Study of the Data Driven Estimation of the $H \to 4\ell$ background with the ATLAS detector

by

KALLIOPI IORDANIDOU
200940

Master Thesis

Section of Nuclear and Particle Physics
Physics Department
School of Sciences
National and Kapodistrian University of Athens

Athens, April 2011

Supervisor: D. Fassouliotis, Assistant Professor
Committe in Charge: Chr. Kourkoumeli (Professor), A. Manousakis (Assistant Professor)

To myself,
To my mother

Contents

Chapter 1

Theory Introduction

1.1 Introduction

In this chapter a brief overview of the Standard Model is given, introducing the Higgs mechanism, the production at hadron colliders and the sensitivity prospects.

1.2 Particles and Interactions

The accepted model for elementary particle physics views quarks and leptons as the basic constituents of ordinary matter. Particles interact via four known basic forces – gravitational,electromagnetic, strong, and weak – that can be characterized on the basis of the following four criteria [1]: the types of particles that experience the force, the relative strength of the force, the range over which the force is effective, and the nature of the particles that mediate the force. The electromagnetic force is carried by the photon, the strong force is mediated with gluons, the $W^{\pm}$ and Z^0 bosons transmit the weak force, and the quantum of the gravitational force is called graviton. A comparison of the (approximate) relative force strengths is given in Table 1.1. Gravity, on a nuclear scale, is the weakest of the four forces and its effect at the particle level can nearly always be ignored [1].

The quarks are fractionally charged spin-$\frac{1}{2}$ strongly interacting particles which are

Type	Relative Strength	Field Particle
Strong	1	gluons
Electromagnetic	10^{-2}	photon
Weak	10^{-6}	$W^{\pm}$ Z^0
Gravitational	10^{-38}	graviton

Table 1.1: *Relative strength of the four forces for two protons inside a nucleus.*

name	symbol	Q	B	S	c	b	t
up	u	$\frac{2}{3}$	$\frac{1}{3}$	0	0	0	0
down	d	$-\frac{1}{3}$	$\frac{1}{3}$	0	0	0	0
strange	s	$-\frac{1}{3}$	$\frac{1}{3}$	-1	0	0	0
charm	c	$\frac{2}{3}$	$\frac{1}{3}$	0	1	0	0
bottom	b	$-\frac{1}{3}$	$\frac{1}{3}$	0	0	-1	0
top	t	$-\frac{1}{3}$	$\frac{1}{3}$	0	0	0	1

Table 1.2: *Quark quantum numbers: charge Q, baryon number B,strangeness S, charm c, bottomness b, and topness t.*

known to form the composites collectively called hadrons:

$$\begin{cases} q\bar{q} \text{ (quark + antiquark) mesons} & \text{integral spin} \rightarrow \text{Bose statistics} \\ qqq \text{ (three quarks) baryons} & \text{half-integral spin} \rightarrow \text{Fermi statistics} \end{cases} .$$

There are six different types of quarks, known as flavors: up (symbol: u), down (d), strange (s), charm (c), bottom (b), and top (t); their properties are given in Table 1.2. (Antiquarks have opposite signs of electric charge, baryon number, strangeness, charm, bottomness, and topness.)

Quarks carry "color" which enables them to interact strongly with one another. Each quark flavor can have three colors usually designated red, green, and blue. The antiquarks are colored antired, antigreen, and antiblue. Baryons are made up of three quarks, one of each color. Mesons consist of a quark-antiquark pair of a particular color and its anticolor. Both baryons and mesons are thus colorless or white. Because the color is different for each quark, it serves to distinguish them and allows the exclusion principle to hold.

One important aspect of on-going research is the attempt to find a unified basis for the different forces. For example, the weak and electromagnetic forces are indeed two different manifestations of a single, more fundamental electroweak interaction. In Figure 1.1 the force merging at high energes is presented.

The electroweak theory has had many notable successes, culminating in the discovery of the predicted $W^{\pm}$ and Z^0 bosons ($m_W = 80.403 \pm 0.029$ GeV and $m_Z = 91.1876 \pm 0.0021$ GeV) [7]. However, the favored electroweak symmetry breaking mechanism requires the existance of a scalar Higgs boson, as yet unseen.

1.3 The Standard Model before Electroweak Symmetry Breaking

The Glashow–Weinberg–Salam electroweak theory which describes the electromagnetic and weak interactions between quarks and leptons, is a Yang–Mills theory based on the

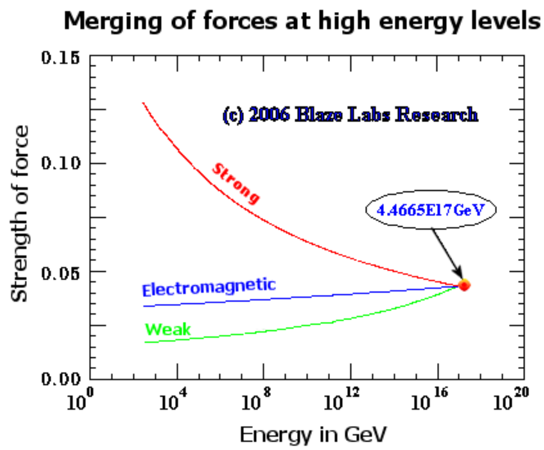

Figure 1.1: *Merging of the forces at high energy limit.*

[]

symmetry group $\mathrm{SU(2)_L} \times \mathrm{U(1)_Y}$ [3]. Combined with the $\mathrm{SU(3)_C}$ based QCD gauge theory which describes the strong interactions, it provides a unified framework to describe the forces (Standard Model) [17]. The model, before introducing the electroweak symmetry breaking mechanism, has two kinds of fields:

• The matter fields for the three generations of left–handed and right–handed chiral quarks and leptons, $f_{L,R} = \frac{1}{2}(1 \mp \gamma_5) f$ [17][7].

• The gauge fields corresponding to the spin–one bosons that mediate the interactions.

The matter fields ψ are minimally coupled to the gauge fields through the covariant derivative D_μ, defined as:

$$D_\mu \psi = \left(\partial_\mu - i g_s T_a G^a_\mu - i g_2 T_a W^a_\mu - i g_1 \frac{Y_q}{2} B_\mu \right) \psi \tag{1.1}$$

where B_μ and $W^{1,2,3}_\mu$ are the fields mentioned previously and corresponds to the generators $\mathrm{Y_q}$ and T^a respectively.

The SM Lagrangian, without mass terms for fermions and gauge bosons is then given by:

$$\begin{aligned} \mathcal{L}_{\mathrm{SM}} &= -\frac{1}{4} G^a_{\mu\nu} G^{\mu\nu}_a - \frac{1}{4} W^a_{\mu\nu} W^{\mu\nu}_a - \frac{1}{4} B_{\mu\nu} B^{\mu\nu} \\ &\quad + \bar{L}_i \, i D_\mu \gamma^\mu \, L_i + \bar{e}_{Ri} \, i D_\mu \gamma^\mu \, e_{R_i} + \bar{Q}_i \, i D_\mu \gamma^\mu \, Q_i + \bar{u}_{Ri} \, i D_\mu \gamma^\mu \, u_{R_i} + \bar{d}_{Ri} \, i D_\mu \gamma^\mu \, d_{R_i} \end{aligned} \tag{1.2}$$

This Lagrangian is invariant under local $\mathrm{SU(3)_C} \times \mathrm{SU(2)_L} \times \mathrm{U(1)_Y}$ gauge transformations for fermion and gauge fields [3]. Since there is experimental evidence for massive bosons (Z,W), mass terms should be added. Thus, this leads to a manifest breakdown of the local $SU(2)_L \times U(1)_Y$ gauge invariance. There is a way of producing gauge bosons and fermion masses without violating the symmetry, this is called the Higgs mechanism.

1.4 Higgs Boson in The Standard Model

The Glashow - Weinberg - Salam (GWS) Electroweak theory initially considers four massless propagators which corresponds to following bosons [2]:

$$W_\mu^{1,2,3}, B_\mu \to W^+, W^-, Z, \gamma \tag{1.3}$$

This transformation is the result of a phenomenon known as "Spotaneous Symmetry Breaking" and in the special case of electroweak force is known as the "Higgs Mechanism" [3].

The GoldStone Theorem

For every spontaneously broken continuous symmetry, the theory contains massless scalar (spin–0) particles called Goldstone bosons. The number of Goldstone bosons is equal to the number of broken generators. For an $O(N)$ continuous symmetry, there are $\frac{1}{2}N(N-1)$ generators; the residual unbroken symmetry $O(N-1)$ has $\frac{1}{2}(N-1)(N-2)$ generators and therefore, there are $N-1$ massless Goldstone bosons. In other words, the breaking of a gauge symmetry comes along with the appearence of a massless boson, usually referred as the Goldstone boson [17].

In the Higgs mechanism the scalar massless scalar field, make disappear the Goldstone boson and produce mass. At that time the Higgs boson and the Higgs field appears. The Higgs boson, produced as previously described, is a vector boson (spin=0), with no charge [7].

1.5 Higgs Production at Hadron Colliders

The main production mechanisms for Higgs particles at hadron colliders make use of the fact that the Higgs boson couples preferentially to the heavy particles, that is the massive W and Z vector bosons, the top quark and, to a lesser extent, the bottom quark. The four main production processes are thus [17]:

- associated production with W/Z: $q\bar{q} \to V + H$
- vector boson fusion: $qq \to V^*V^*qq + H$

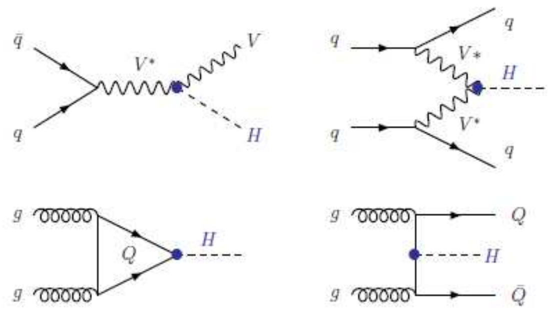

(a)

Figure 1.2: The dominant SM Higgs boson production mechanisms in hadronic collisions.

- gluon-gluon fusion: $gg \to H$
- associated production with heavy quarks: $gg, q\bar{q} \to Q\bar{Q} + H$

There are also several mechanisms for the pair production of the Higgs particles [17]:

$$\text{Higgs pair \ production} : pp \to HH + X \tag{1.4}$$

and the relevant sub–processes are the $gg \to HH$ mechanism, which proceeds through heavy top and bottom quark loops, the associated double production with massive gauge bosons, $q\bar{q} \to HHV$, and the vector boson fusion mechanisms $qq \to V^*V^* \to HHqq$. However, because of the suppression by the additional electroweak couplings, they have much smaller production cross sections than the single Higgs production mechanisms listed above [17].

Also suppressed are processes where the Higgs is produced in association with one or more hard jets in gluon–gluon fusion, the associated Higgs production with gauge boson pairs, the production with a vector boson and two jets. Other production processes exist which have even smaller production cross sections. Finally, Higgs bosons can also be produced in diffractive processes. For the interesting exclusive central diffractive processes, the mechanism is mediated by color singlet exchanges leading to the diffraction of the incoming hadrons and a centrally produced Higgs boson. A mixture of perturbative and non perturbative aspects of QCD is needed to evaluate the cross sections.

1.5.1 Higgs Boson Production in Gluon–Gluon Fusion

Gluon fusion through a heavy-quark loop (see 1.3) is the main production mechanism of the Standard Model Higgs boson at hadron colliders. When combined with the decay

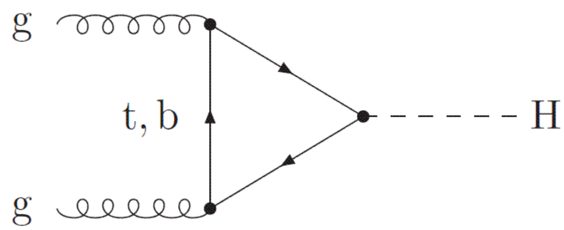

Figure 1.3: *Feynman diagram contributing to $gg \to H$ at lowest order.*

[]

channels $H \to \gamma\gamma$, $H \to WW$, and $H \to ZZ$, this production mechanism is one of the most important for Higgs-boson searches and studies over the entire mass range, $100GeV \leq M_H \leq 1TeV$, to be investigated at the LHC [17].

The dynamics of the gluon–fusion mechanism is controlled by strong interactions. In QCD perturbation theory, the leading order (LO) contribution to the gluon-fusion cross section is proportional to the square of the QCD coupling constant. The main contribution arises from the top quark, due to its large Yukawa coupling to the Higgs boson. The QCD radiative corrections to this process at next–to–leading order (NLO) increase the LO cross section by about $80-100\%$ at the LHC. The next–to–next–to–leading order (NNLO) calculation has been consistently improved by resumming the soft–gluon contributions up to NNLL, this leads to an additional increase of the cross section of about $7-9\%$ ($6-7\%$) at $\sqrt{s} = 7\ (14)TeV$ [17]. The evaluation of electroweak (EW) corrections is dominated by a large uncertainty comes from the fact that it is not obvious how to combine them with the large QCD corrections.

1.5.2 Higgs Boson Production in Vector–Boson Fusion

The production of a Standard Model Higgs boson in association with two hard jets in the forward and backward regions of the detector, frequently quoted as the gvector-boson fusionh (VBF) channel, is a cornerstone in the Higgs-boson search both in the ATLAS experiment [23]. This channel contributes in a significant way to the inclusive Higgs production over the full Higgs mass range. The production of a Higgs boson + 2 jets receives two contributions at hadron colliders. The hard jet pairs have a strong tendency to be forward.backward directed in contrast to other jet-production mechanisms, offering a good background suppression (transverse-momentum and rapidity cuts on jets, jet rapidity gap, central jet veto, etc.).

The measurement of the Higgs-boson couplings in VBF is essential for the measurement of the $H \to WW$ and $H \to ZZ$ couplings. Among the backgrounds that contribute to the final state, events from $Higgs + 2jets$ production via gluon fusion are dominant. Although the final states are similar, the kinematic distributions of jets are very different due to the fact that in the gluon–fusion channel, the Higgs boson is radiated off a heavy quark loop that couples to any parton of the incoming hadrons via gluons [23]. According to a next–to–leading order (NLO) estimation [24], the gluon fusion contribution shows that its residual scale dependence is still of the order of 35%. Since, in the phase–space regions which are accessible at hadron colliders, VBF reactions are dominated by t-channel electroweak gauge–boson exchange, s-channel exchange contributions and kinematically suppressed fermion interference contributions are disregarded [23].

1.6 Higgs Branching Ratios

Figure 1.4(a) presents the total Higgs boson production cross–section at $\sqrt{s} = 7TeV$ and $\sqrt{s} = 14TeV$, whereas Figures 1.4(b) and 1.4(c) present the analytical contribution of each production mode for the different $\sqrt{s}$ respectively [23]. It is obvious that gluon fusion, more usual at NNLO, is dominant but the uncertainty is estimated to be $\sim 15\%$ due to large corrections for gluon initiated processes [25]. Vector–boson fusion comes second at NLO, with an uncertainty of $\sim 5\%$, and then follows associated production with small cross–section to background ratio, but revival is of interest in boosted jets [25].

The branching ratios of each contributing procedure and width are presented in Figures 1.5(a), 1.5(b) and 1.5(c) respectively [23]. From Figure 1.5(c) it can be seen that for the intermediate to high mass range most sensitive channels are the ZZ and WW, whereas for low to intermediate range:

- $\gamma\gamma$: is very clean
- $\tau\tau$: needs distinctive production features to reduce background, ex. VBF [25]
- bb: huge backgrounds from QCD
- $WW \rightarrow 2\ell + MET$: very sentitive and less accurate
- $ZZ \rightarrow 4\ell$: less sensitive but cleanest

Figure 1.5(b) presents the same plot zoomed in the mass region between 90 and 210.

Analytical branching ratios of each procedure for different Higgs masses can be found on Appendix B.

1.7 ATLAS Sensitivity Prospects for Higgs Boson Production at 7/8/9 TeV

The cross-section of the most significant processes for Standard Model Higgs boson production at the LHC and the ratio of the production cross–sections at different centre

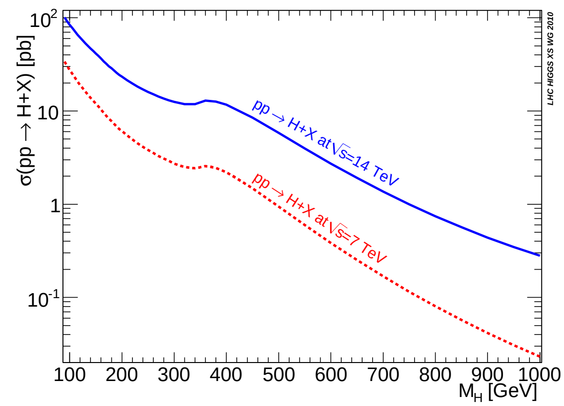

(a)

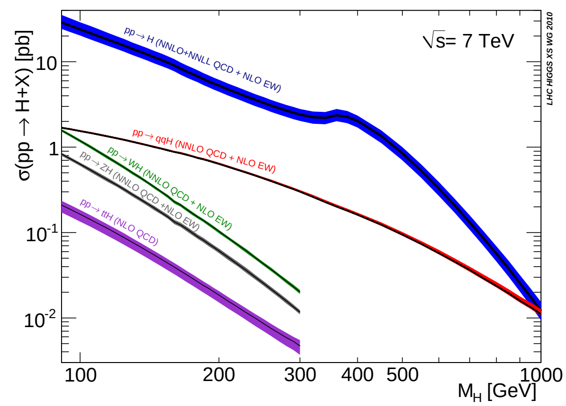

(b)

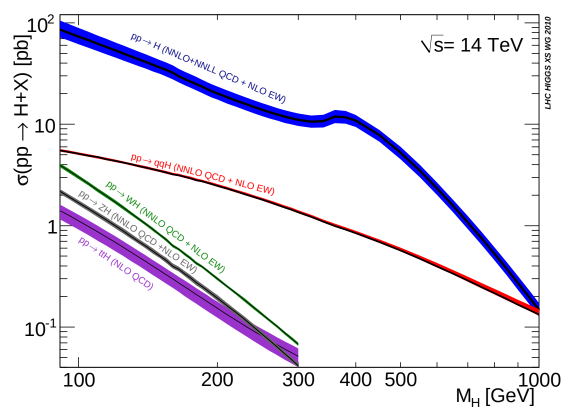

(c)

Figure 1.4: *Standard Model Higgs boson production cross sections.*
[]

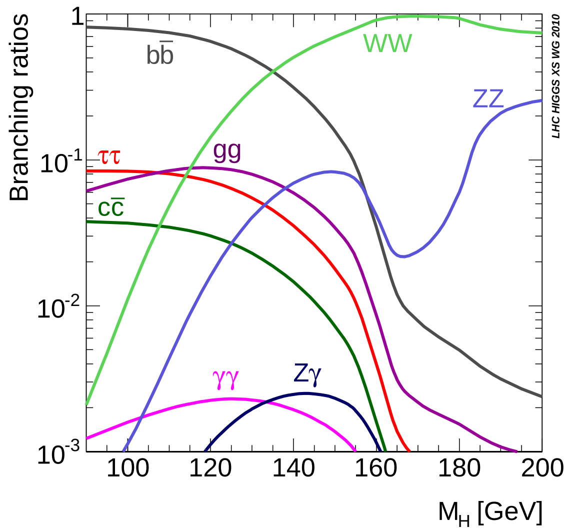

(a)

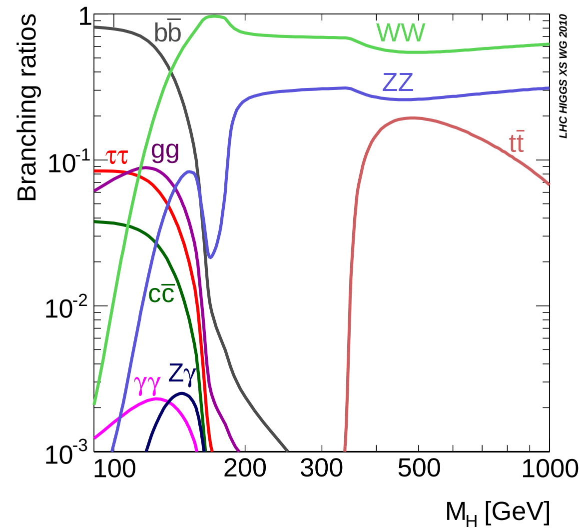

(b)

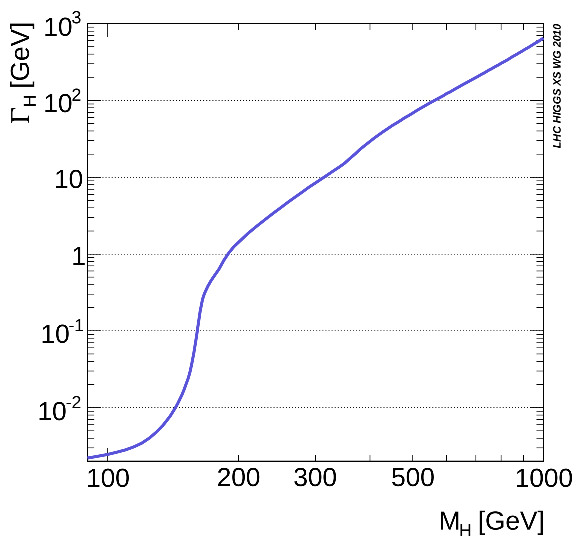

(c)

Figure 1.5: *Standard Model Higgs boson decay branching ratio and width.*
[]

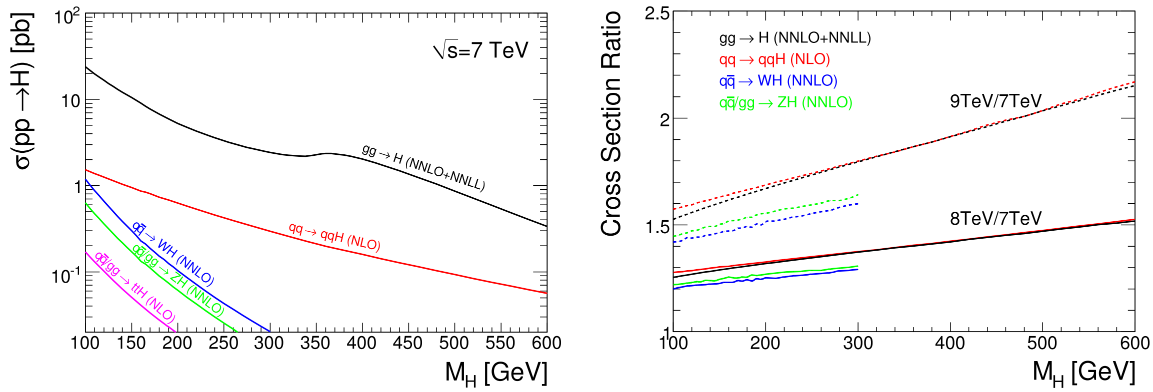

(a) (b)

Figure 1.6: *1.6(a): Cross-section of the most significant processes for Standard Model Higgs boson production at the LHC. 1.6(b): The ratio of the production cross-sections at different centre-of-mass energies.*

[]

of mass energies are presented in Figures 1.6 [23].

Figure 1.7 shows the observed and expected exclusion limits, along with the expected $\pm 1\sigma$ and $+2\sigma$ bands, as a function of Higgs mass for the $H \rightarrow 4\ell$ with an integrated luminosity of 40 pb^{-1} [22]. The green and yellow bands indicate the range in which the limits are expected to lie. The production of a SM-like Higgs boson of $M_H = 200$ GeV with a production cross-section of 18 times the SM value can be excluded at 95% C.L.

The multiple of the cross-section which can be excluded using 1 $fb^{-}1$ of data at 7 TeV, shown in Figure 1.8 [22].

1.8 $Higgs \rightarrow 4\ell$ Discovery Sensitivity

The experimentally cleanest signature for the discovery of the Higgs boson is its "golden" decay to four leptons (electrons and muons): $H \rightarrow ZZ \rightarrow 4\ell$. The excellent energy resolution and linearity of the reconstructed electrons and muons leads to a narrow 4–lepton invariant mass peak on top of a smooth background [8]. The expected signal to background ratio after all experimental cuts depends on the Higgs boson mass itself, since it is a free parameter in the Standard Model. The major component of the background consists of irreducible $ZZ \rightarrow 4\ell$ decays. The most challenging mass region is between $120 - 150 GeV$ where one of the Z bosons is off–shell giving low transverse momentum leptons [8]. In this region backgrounds from $Zb\bar{b} \rightarrow 4\ell$ and $t\bar{t} \rightarrow 4\ell$ are important and require tight lepton isolation cuts to keep their contribution well below the ZZ continuum.

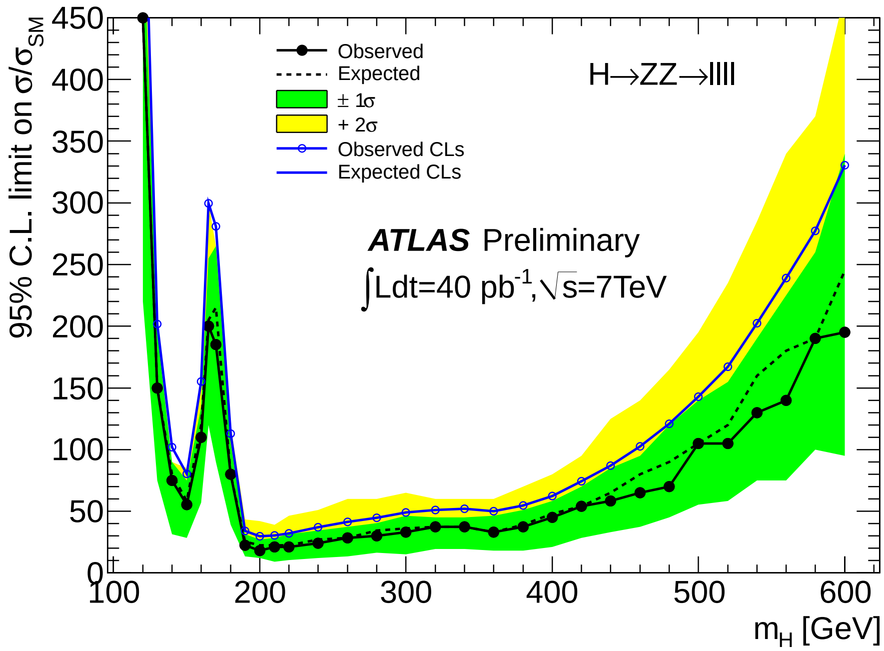

Figure 1.7: *95% C.L. limits on the $H \to ZZ \to 4\ell$ expressed as the ratio to the Standard Model cross-section based on CL_{s+b} in a one-sided frequentist method. The dotted line, green band and yellow band indicate the median expected limit, the $\pm1\sigma$, and the $+2\sigma$ band respectively from background-only pseudo-experiments in which the auxiliary measurements that are used to estimate identification efficiencies etc. are also included in the ensemble. Downward fluctuations below the -1σ band would be considered beyond the sensitivity of the experiment and a power constraint would be invoked, but this does not occur for the observed limit. The median expected and the observed 95% CL_s upper limit, which coincide in this analysis, are also shown.*

[]

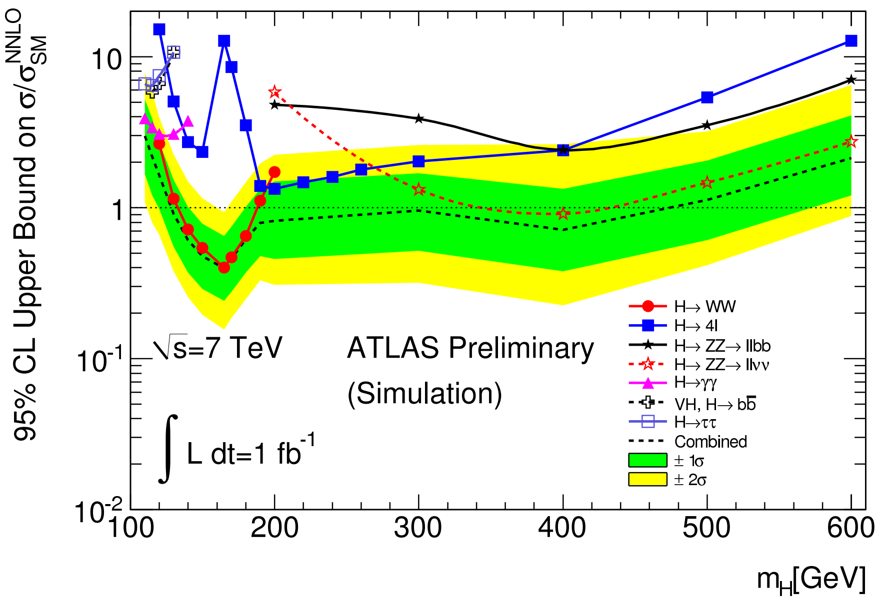

Figure 1.8: *The multiple of the cross-section, using 1 $fb^{-}1$ of data at 7 TeV.*
[]

Bibliography

[1] L. Anchordoqui and Fr. Halzen, "Lessons in Particle Physics", arXiv:0906.1271v1

[2] M. E. Peskin and D. V. Schroeder, "An Introduction to Quantum Field Theory", 1995 (ISBN 0201503972)

[3] C. Burgess and G. Moore, "The Standard Model, A Primer", 2007 (ISBN 0521860369)

[4] H. Georgi, "Weak Interactions and Modern Particle Theory"

[5] M. Srednicki, "Quantum Field Theory"

[6] J. F. Donoghue, E. Golowich and B. R. Holstein, "Dynamics of the Standard Model"

[7] F. Halzen and A. D. Martin, "Quarks and Leptons"

[8] D. H. Perkins, "Introduction to High Energy Physics"

[9] B. R. Martin and G. Shaw, "Particle Physics"

[10] J. F. Gunion, H. E. Haber, G. Kane, S. Dawson, "The Higgs Hunter's Guide"

[11] James Wells, "Lectures on Higgs Boson Physics in the Standard Model and Beyond", arXiv:0909.4541

[12] Riccardo Barbieri , "Ten Lectures on the Electroweak Interactions", arXiv:0706.0684v1

[13] Scott Willenbrock, "Symmetries of the Standard Model", hep-ph/0410370

[14] Sven Heinemeyer, "Higgs and Electroweak Physics", arXiv:0912.0361

[15] S. F. Novaes, "Standard Model: An Introduction", hep-ph/0001283

[16] Antonio Pich, "The Standard Model of Electroweak Interactions", arXiv:0705.4264

[17] Abdelhak Djouadi, "The Anatomy of Electro-Weak Symmetry Breaking. I: The Higgs boson in the Standard Model", hep-ph/0503172

[18] Stefan Pokorski, "Phenomenological guide to physics beyond the Standard Model", hep-ph/0502132

[19] Gautam Bhattacharyya, "A Pedagogical Review of Electroweak Symmetry Breaking Scenarios", arXiv:0910.5095

[20] V.A.Bednyakov, N.D.Giokaris, A.V.Bednyakov, "On Higgs mass generation mechanism in the Standard Model", arXiv:hep-ph/0703280

[21] Atlas Higgs Public Results - TWiki

[22] The ATLAS collaboration, "Search for the Standard Model Higgs boson in the decay channel $H \rightarrow ZZ^{(*)} \rightarrow 4\ell$ with $40pb^{-1}$ of pp collisions at $\sqrt{s} = 7TeV$" ATLAS-COM-CONF-2011-047

[23] S. Dittmaier, C. Mariotti, G. Passarino, and R. Tanaka (eds.), "Handbook of LHC Higgs Cross Sections: 1. Inclusive Observables ", arXiv:1101.0593v2

[24] A. Nikitenko and M. L. Vazquez Acosta, "Monte Carlo study of ggH+jets contribution to Vector Boson Fusion Higgs production at the LHC", arXiv:0705.3585.

[25] S. Giagu, "Results from the ATLAS experiment", Slides for the Mass 2011 Conference in Odense, Denmark. May 9-13, 2011, ATL-PHYS-SLIDE-2011-194

[26] ATLAS Collaboration, "Expected Performance of the ATLAS Experiment (Detector, Trigger and Physics)", arXiv:0901.0512

Chapter 2

LHC Structure, Operation and Experiments

2.1 Introduction

The Large Hadron Collider (LHC) sits in a circular tunnel 27 km in circumference. The tunnel is buried around 50 to 175 m. underground. It straddles the Swiss and French borders on the outskirts of Geneva. The LHC is designed to collide two counter rotating beams of protons or heavy ions. Proton-proton collisions are foreseen at an energy of 7 TeV per beam, the first collisions at an energy of 3.5 TeV per beam took place on 30th March 2010. The advantage of circular accelerators over linear accelerators is that the ring topology allows continuous acceleration, as the particle can transit indefinitely. Another advantage is that a circular accelerator is relatively smaller than a linear accelerator of comparable power. The beams move around the LHC ring inside a continuous vacuum guided by superconducting magnets that are cooled to $1.9K$ by a huge cryogenics system. The cables conduct current without resistance in their superconducting state. The bbeams can be stored at high energy for hours. Some of the foundamental LHC parameters are given in Table 2.1 [2].

Injection of hydrogen gas into a metal cylinder, called *Duoplasmatron, and surrounding it with an electrical field, leads to break down of the gas into its constituent protons and electrons, see Figure 2.2 [2]. This process yields about* 70% *protons and it is the source of the protons. Analytically, the chemical reactions which take place are [2]:*

$$H_2 + e^- \rightarrow H_2 + +2e^- \tag{2.1}$$

$$H_2^+ + e^- \rightarrow H^+ + H + e^- \tag{2.2}$$

LHC parameters	
Circumference	$26659m$
Dipole operating temperature	$1.9K$
Number of arcs ($2450m$ long)	8
Number of lattice cells per arc	23
Number of straight sections ($545m$ long)	8
Main RF System	$400.8MHz$
Number of magnets (dipoles, quadrupoles ... dodecapoles)	9300
Number of dipoles	1232
Number of quadrupoles	858
Number of RF cavities	8/ beam
Nominal energy (protons)	$7TeV$
Momentum at collision	$7TeV/c$
Momentum at injection	$450GeV/c$
Nominal energy (ions)	$2.76TeV/nucleon$
Peak magnetic dipole field	$8.33T$
Current in main dipole	$11800A$
Energy density of the LHC magnets	$500kJ/m$
Main dipole coil inner diameter	$56mm$
Distance between aperture axes ($1.9K$)	$194.00mm$
Distance between aperture axes ($293K$)	$194.52mm$
Main Dipole Length	$14.3m$
Horizontal force at 8.33 T (inner and outer layer)	$1.7MN/m$
Maximum current with NO resistence ($1.9Ke8.33T$)	$17000A$
Maximum current with NO resistence ($1.9Ke0T$)	$50000A$
Number de strands per cable	36
Bending radius	$2803.95m$
Minimum distance between bunches	$\sim 7m$
Bunch spacing	$25ns$
Design Luminosity	$10^{34}cm^{-2} \cdot s^{-1}$
No. of bunches / proton beam	2808
No. of protons / bunch (at start)	$1.15 \cdot 10^{11}$
Circulating current / beam	$0.54A$
Number of turns / second	11245
Stored beam energy	$360MJ$
Stored energy in magnets	$11GJ$
Beam lifetime	$10h$
Average crossing rate	$31.6MHz$
Number of collisions / second	$600millions$
Radiated Power / beam (syncrotron radiation)	$\sim 6KW$
Total crossing angle (collision point)	$300\mu rad$
Emittance ϵ_n	$3.75\mu rad$
β	$0.55m$

Table 2.1: *Some of the LHC designed parameters [2]*

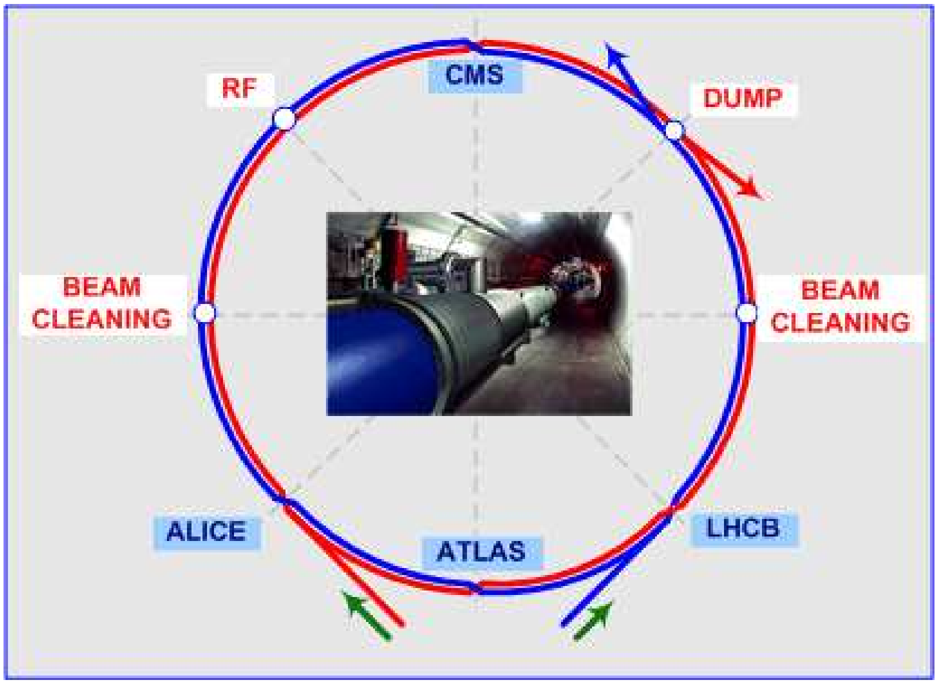

Figure 2.1: *Schematic view of the LHC and the experiments.*

$$H + e^- \rightarrow H^+ + 2e^- \tag{2.3}$$

Protons are accelerated up to $100kV$ *and then sent to a Radio Frequency Quadrupole (QRF), an accelerating component that both speeds up and focuses the proton beam. Four vanes (electrodes) provide a quadrupole RF field that provides a transverse focusing of the beam. Spacing of the vanes bunches and accelerates up to* $750keV$ *the beam. From the quadrupole, the particles are sent to the linear accelerator (LINAC2).The linac tank is a multi-chamber resonant cavity tuned to a specific frequency which creates potential differences in the cavities that accelerate the particle up to* $50MeV$ *[2]. Protons cross the linac and reach the* $157m$ *circumference circular accelerator Proton Synchrotron Booster (PSB) in a few microseconds. Actually, PSB is a circular four rings accelerator.*

The beam line to the PSB from the Linac is $80m$ *long. Twenty quadrupole magnets focus the beam along the line two bending and eight steering magnets direct the beam. The PS Booster accelerates them to* $1.4GeV$ *(factor of 28) in* $530ms$*, then after less than a microsecond they are injected in the* $628m$ *circumference circular accelerator Proton Synchrotron (PS) [2].*

In the PS protons can either be accelerated/manipulated/extracted in $1025ms$ *or wait for* 1.2 *more seconds before being accelerated if they are part of the first PSB batch to the PS. They are accelerated to* $25GeV$ *[2]. The PS is responsible for providing 81*

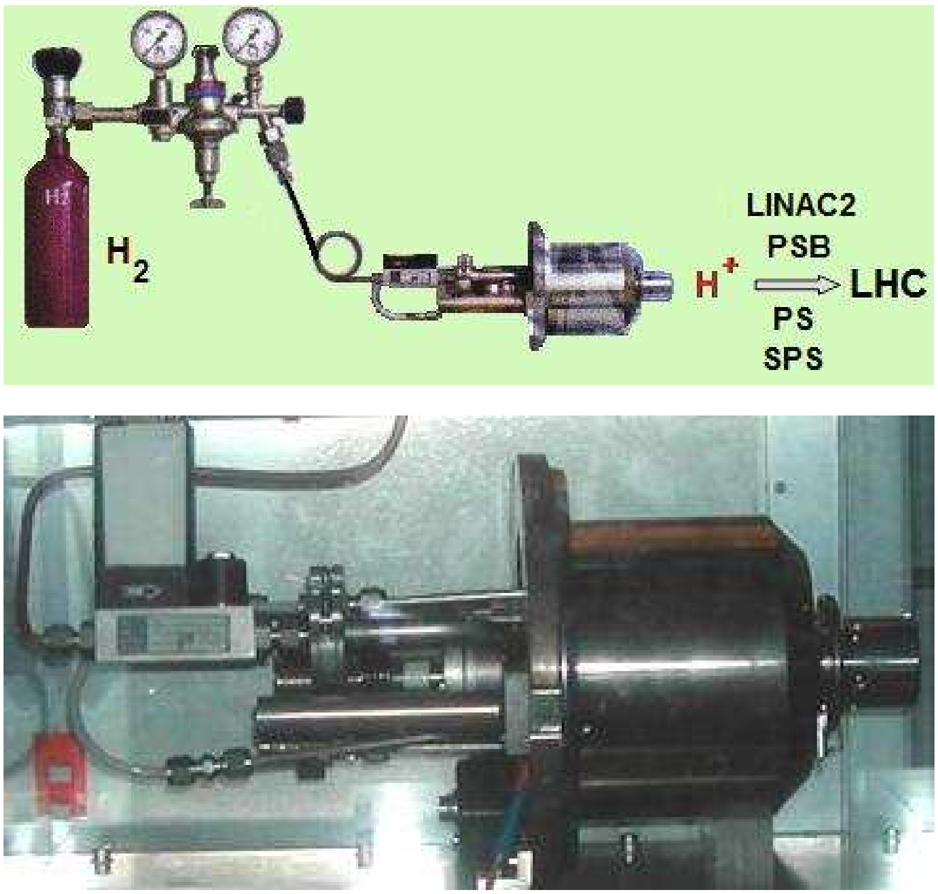

Figure 2.2: *Injection of hydrogen gas into a metal cylinder, surrounded by electric field, creates the proton beam.*

bunch packets with $25ns$ spacing for the LHC.

Triplets of 81 bunches formed in the PS and injected into the $7km$ circumference circular accelerator Super Proton Synchrotron (SPS), taking up $\sim 27\%$ of the SPS beamline. They wait for 10.8, 7.2, 3.6, or 0. seconds whether they are part of the first, second, third, or fourth PS batch to the SPS[2]. The SPS accelerates them to $450GeV$ in 4.3 seconds, and sends it to the LHC [2].

Protons are finally transferred to the LHC (both in a clockwise and counterclockwise direction, the filling time is 420 per LHC ring). The total LHC beam consists of 12 "supercycles" of the 234 bunches from SPS [2]. They have to wait up to 20 minutes on the LHC $450GeV$ injection plateau before the 25 minutes ramp to high energy, and these 45 minutes dominates the transit time.

The beams are stored at high energy for 10 hours, the so called "beam lifetime", and particles make four hundred million revolutions around the machine.

The more is the density of the stored particles the more decreases the beam lifetime. Coulomb scattering of charged particles traveling together causes an exchange of momentum between the transverse and longitudinal directions. Due to relativistic effects, the momentum transferred from the transverse to the longitudinal direction is enhanced by the relativistic factor γ. For stored beam, particles are lost if their longitudinal momentum deviation exceeds the RF bucket or the momentum aperture determined by the lattice. This is called the Touschek effect (after the austrian phyisicist Bruno Touschek) and is generally the limiting factor in beam lifetime.

After $10h$ of beam collisions, the beam itself is exhausted and is dumped. The dipole magnets are then ramped down to $0.54T$ and they stay at flat bottom for some $2040min$. Meanwhile beam injection is repeated before the magnets are ramped up again to $8.3T$ for another cycle of high energy collisions. The machine is designed to withstand some 20000 such cycles in 20 years lifetime [2].

2.2 Proton Collisions

In the LHC, proton bunches are accelerated (over a period of 25 minutes) to their peak $7TeV$ energy, and finally circulated for 10 hours while collisions occur at the four intersection points.

Between each consecutive bunch there will be $7.5m$. So, with a circumference of $27km$ there should be [2]:

$$26659/7.5 \sim 3550\, bunches \tag{2.4}$$

To get a correct sequence of bunches injected into the ring and to be able to insert new bunches when non-useful ones are extracted it is necessary to allow enough space for that. The effective number of bunches per beam is 2808. Each bunch has $1.15 \cdot 10^{11}$ protons ($1cm^3$ STP of hydrogen has $\sim 10^{19}$ protons). Each bunch gets squeezed down

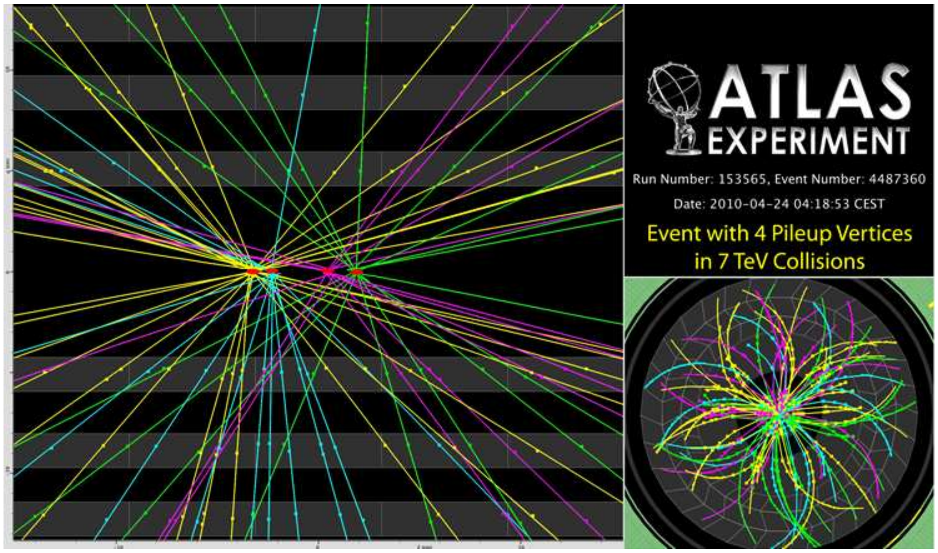

Figure 2.3: *Event with four Pileup Vertices recorded at the ATLAS detector on April 24th 2010 [2].*

(using magnetics lenses) to $16 \times 16\mu m$ *section at an interaction point, where collisions take place [1]. The "volume occupied" for each proton in the inteaction point is:*

$$(74800 \times 16 \times 16)/(1.15 \cdot 10^{11}) \sim 10^{-4} \mu m^3 \tag{2.5}$$

That is much bigger than an atom, so a collision is still rare. The probability of one particular proton in a bunch coming from the left hitting a particular proton in a bunch coming from the right depends roughly on the proton size (d^2 *with* $d \sim 1fm$*) and the cross-sectional size of the bunch (*σ^2*, with* $\sigma = 16\mu m$*) in the interaction point [2].*

$$Probability = \frac{d^2_{proton}}{\sigma^2} = 4 \cdot 10^{-21} \tag{2.6}$$

But with $1.15 \cdot 10^{11}$ *protons/bunch a good number of interactions will be possible every crossing. Now, the number of interactions will be:*

$$Probability \times N^2 (N = number\, of protons/bunch) =\sim 50\, interactions\, every\, crossing \tag{2.7}$$

But just a fraction of these interactions ($\sim 50\%$*) are inelastic scatterings that give rise to particles at sufficient high angles with respect to the beam axis. Therefore, there are about 20 "effective" collisions every crossing. With 11245 crosses per second we get:*

$$11245 \times 2808 = 31.6\, millions\, crosses(''average\, crossing\, rate'') \tag{2.8}$$

$$(31.6 \cdot 10^6 crosses/s) \times (20 collisions/cross) = 600\, millions\, collision/s \qquad (2.9)$$

If we consider 3550 bunches: $11245 \times 3550 = 40 millions\ crosses = \sim 40 MHz$.

2.3 The LHC Experiments

The two large experiments, ATLAS and CMS, are based on general-purpose detectors. They are designed to investigate the largest range of physics possible. Having two independently designed detectors is vital for cross-confirmation of any new discoveries made.

Two medium-size experiments, ALICE and LHCb, have specialised detectors for analysing the LHC collisions in relation to specific phenomena.

Two experiments, TOTEM and LHCf, are much smaller in size. They are designed to focus on "forward particles" (protons or heavy ions). These are particles that just brush past each other as the beams collide, rather than meeting head-on

2.3.1 ATLAS

ATLAS is designed to investigate a wide range of physics, including the search for the Higgs boson, extra dimensions, and particles that could make up dark matter. It records sets of measurements on the particles created in collisions - their paths, energies, and their identities [7]. This is accomplished through six different detecting subsystems that identify particles and measure their momentum and energy. Another vital element of ATLAS is the huge magnet system that bends the paths of charged particles for momentum measurement [8].

2.3.2 CMS

The Compact Muon Solenoid (CMS) experiment uses a general-purpose detector to investigate a wide range of physics, including the search for the Higgs boson, extra dimensions, and particles that could make up dark matter. Although it has the same scientific goals as the ATLAS experiment, it uses different technical solutions and design of its detector magnet system to achieve these [4]. The CMS detector is built around a huge solenoid magnet. This takes the form of a cylindrical coil of superconducting cable that generates a magnetic field of 4 teslas, about 100 000 times that of the Earth. The magnetic field is confined by a steel "yoke" that forms the bulk of the detector's weight of 12500 tonnes.

2.3.3 ALICE

The Large Ion Collider Experiment (ALICE) collides lead ions to recreate the conditions just after the Big Bang under laboratory conditions. The data obtained will allow to study a state of matter known as quark - gluon plasma, which is believed to have existed soon after the Big Bang. Collisions in the LHC will generate temperatures more than 100000 times hotter than the heart of the Sun. The ALICE collaboration plans to study the quark-gluon plasma as it expands and cools, observing how it progressively gives rise to the particles that constitute the matter of our Universe today [5].

2.3.4 LHCb

The Large Hadron Collider beauty experiment (LHCb) specialises in investigating the slight differences between matter and antimatter by studying the "beauty" quark. It uses a series of sub-detectors to detect mainly forward particles. The first sub-detector is mounted close to the collision point, while the next ones stand one behind the other, over a length of 20 m [2]. An abundance of different types of quark will be created by the LHC before they decay quickly into other forms. To catch the b-quarks, LHCb has developed sophisticated movable tracking detectors close to the path of the beams circling in the LHC.

2.3.5 TOTEM

the TOTal Elastic and diffractive cross section Measurement experiment (TOTEM) studies forward particles to focus on physics that is not accessible to the general-purpose experiments. Among a range of studies, it will measure, in effect, the size of the proton and also monitor accurately the LHC's luminosity. To do this TOTEM must be able to detect particles produced very close to the LHC beams [6]. It will include detectors housed in specially designed vacuum chambers called "Roman pots", which are connected to the beam pipes in the LHC. Eight Roman pots are placed in pairs at four locations near the collision point of the CMS experiment. Although the two experiments are scientifically independent, TOTEM complements the results obtained by the CMS detector and by the other LHC experiments overall.

2.3.6 LHCf

the Large Hadron Collider forward (LHCf) experiment uses forward particles created inside the LHC as a source to simulate cosmic rays in laboratory conditions [7]. Studying how collisions inside the LHC cause similar cascades of particles to those of cosmic rays, it will help to interpret and calibrate large-scale cosmic-ray experiments that can cover thousands of kilometres.

Bibliography

[1] Lyndon Evans, "The Large Hadron Collider: a Marvel of Technology ", CERN and EPFL Press (2009)

[2] Taking a closer look at ATLAS

[3] The LHC Experiments

[4] CMS Physics Technical Design Report, Volume I: Detector Performance and Software, CERN-LHCC-2006-001 ; CMS-TDR-008-1, 2006

[5] ALICE : Technical proposal for a Large Ion collider Experiment at the CERN LHC, CERN-LHCC-95-71 ; LHCC-P-3,1995

[6] The TOTEM Collaboration et al 2008 JINST 3 S08007

[7] The LHCf Collaboration et al 2008 JINST 3 S08006

[8] ATLAS collaboration, ATLAS Detector and Physics Performance Technical Design Report Vol I, CERN-LHCC-99-14, 1999

[9] ATLAS collaboration, ATLAS Detector and Physics Performance Technical Design Report Vol II, CERN-LHCC-99-15, 1999

[10] ATLAS collaboration, Inner Detector Technical Design Report Vol I, CERN-LHCC-97-16, 1997

[11] ATLAS collaboration, Inner Detector Technical Design Report Vol II, CERN-LHCC-97-17, 1997

[12] ATLAS collaboration, Liquid Argon Technical Design Report, CERN-LHCC-96-41, 1996

[13] ATLAS collaboration, Tile Calorimeter Technical Design Report, CERN-LHCC-96-12, 1996

[14] A. Artamonov et al., "The ATLAS Forward Calorimeter JINST 3", 2008

[15] J.Barriere et al, ”The alignment system of the ATLAS barrel muon spectrometer”, ATL-MUON-PUB-2008-007, 2008

[16] C. Amelung et al, ”The Optical Alignment System of the ATLAS Muon Spectrometer Endcaps”, ATL-MUON-PUB-2008-003, 2008

[17] C. Grupen and B. Shwartz, ”Particle Detectors”, 2nd Edition, Cambridge 2008

Chapter 3

Atlas Detector Description

3.1 Introduction

ATLAS (A Toroidal LHC Apparatus) is one of two General Purpose Detectors at the CERN Large Hadron Collider (LHC). The LHC will collide 7 TeV protons together with a center of mass energy of 14 TeV and a design luminosity of $10^{-34} cm^{-2} s^{-1}$ *[7]. The bunch crossing time will be 25ns and at full luminosity there will be approximately 22 proton-proton collisions per bunch crossing. The detector is a cylinder with a total length of 42 m and a radius of 11 m and weighs approximately 7000 tones. To investigate the foundamental processes of nature at the Large Hadron Collider (LHC), detectors of unprecedented size and complexity were designed.*

The major ATLAS components are:

- *The Muon Spectrometer*
- *The Inner Detector*
- *The Calorimeters*
- *Solenoidal and Toroidal Magnets*
- *Data acquisition and Computing*

3.2 The Coordinate System

The origin of the ATLAS coordinate system is defined as the nominal interaction point in the center of the detector [7]. The z-axis runs parallel to the beam line in counter-clockwise direction. The half of the detector that corresponds to positive values of z is referred to as side A and the other half as side C. The x-axis points to the center of the LHC ring and the y-axis points upwards to the surface, resulting in a righthanded

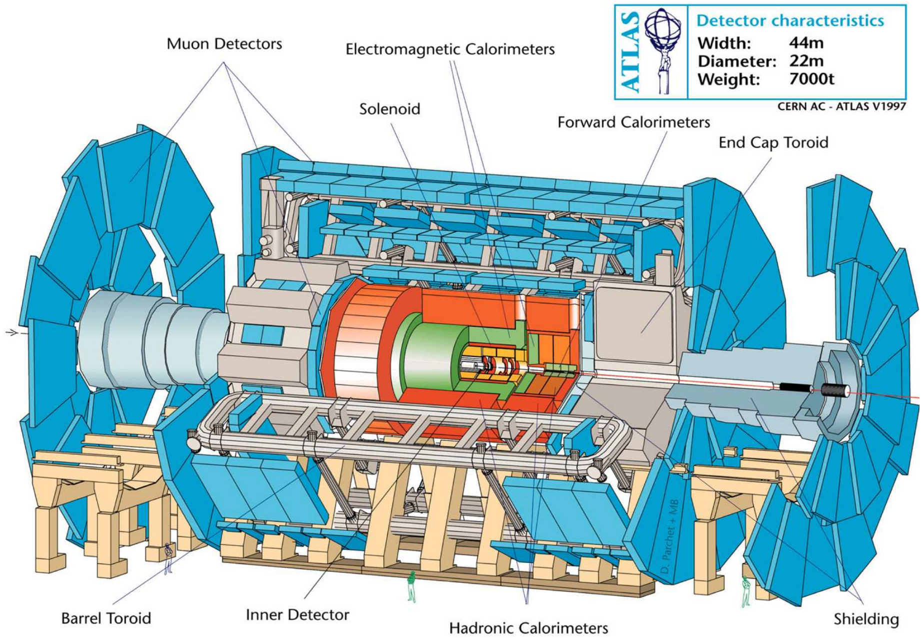

Figure 3.1: *The Atlas Detector.*
[]

orientation. The xy-plane is referred to as the transverse plane. The ATLAS detector has a global cylindrical structure, where each subdetector consists of concentric layers around the beam axis, the barrel component, and two endcaps formed by disks perpendicular to the z-axis on each side of the interaction point. A coordinate system closely related to cylindrical coordinates is convenient. The radial distance is given by $R = \sqrt{x^2 + y^2}$*. The azimuthal angle* $\phi \in [-\pi, \pi]$ *is the angle with the positive x-axis and increases in clockwise direction when looking down the positive z-axis. The polar angle* $\theta \in [0, \pi]$ *is defined as the angle with the positive z-axis, albeit generally replaced by the pseudorapidity* η*, which is given by*

$$\eta = -ln(tan[\frac{\theta}{2}]) \tag{3.1}$$

The preference for this quantity is motivated by the particle flux being roughly constant as a function of η*. A direction* (eta, ϕ) *is assigned to reconstructed final state objects and the opening angle between two of them is denoted* ΔR*:*

$$\Delta R = \sqrt{(\Delta\eta)^2 + (\Delta\phi)^2} \tag{3.2}$$

3.3 Requirements

The performance requirements for the design of the ATLAS detector are based on the processes that may be observed at this new energy scale, such as the production of the Higgs boson, SUSY particles or or any kind of Beyond the SM physics. The extensive variety of objects to be detected, the broad energy range of particles to be measured, the high radiation conditions and the high collision rate impose strict requirements on the detectorfs precision, speed, performance, radiation hardness, efficiency and acceptance. The performance requirements in terms of resolution as well as the acceptance of each subdetector are summarized in Table 3.3 [8]. An additional challenge is the instantaneous selection of collisions to be stored, which is taken care of by the trigger system.

Subdetector	Required Resolution	$\|\eta\|$ coverage
Inner Detector	$\sigma(P_T)/P_T = 0.05\% P_T \oplus 1\%$	< 2.5
Electromagnetic Calorimeter	$\Sigma(E)/E = 10\%/\sqrt{E(GeV)} \oplus 0.7\%$	< 3.2
Hadronic Calorimeter	$\Sigma(E)/E = 50\%/\sqrt{E(GeV)} \oplus 3\%$	< 3.2
	$\Sigma(E)/E = 100\%/\sqrt{E(GeV)} \oplus 10\%$	$(3.1, 4.9)$
Muon Spectrometer	$\sigma(P_T)/P_T = 0.05\% \, at \, P_T = 1TeV$	< 2.7

Table 3.1: *Performance requirements for the subdetectors of the ATLAS detector*

3.4 The Inner Detector

3.4.1 Introduction

The Inner Detector is able to measure the tracks of the hundreds of charged particles that are produced in the proton-proton collisions in the middle of the detector every 25ns. It consists of concentric layers of tracking detectors, with the highest precision detectors closest to the collision point. The colliding beams produce intense levels of radiation, making radiation hardness a top priority for the detector and readout electronics. At the same time, the amount of material in the Inner Detector must be minimized to avoid disturbing the trajectories of the particles.

3.4.2 Pixel and Silcon Strip Detectors

High precision and high efficiency semiconductor detector elements are needed near the collision point in order to distinguish individual particle tracks from the hundreds produced in each collision [7]. The closest detector layers contain over 80 million tiny rectangular pixels, which are capable of resolving particle positions to better than 14

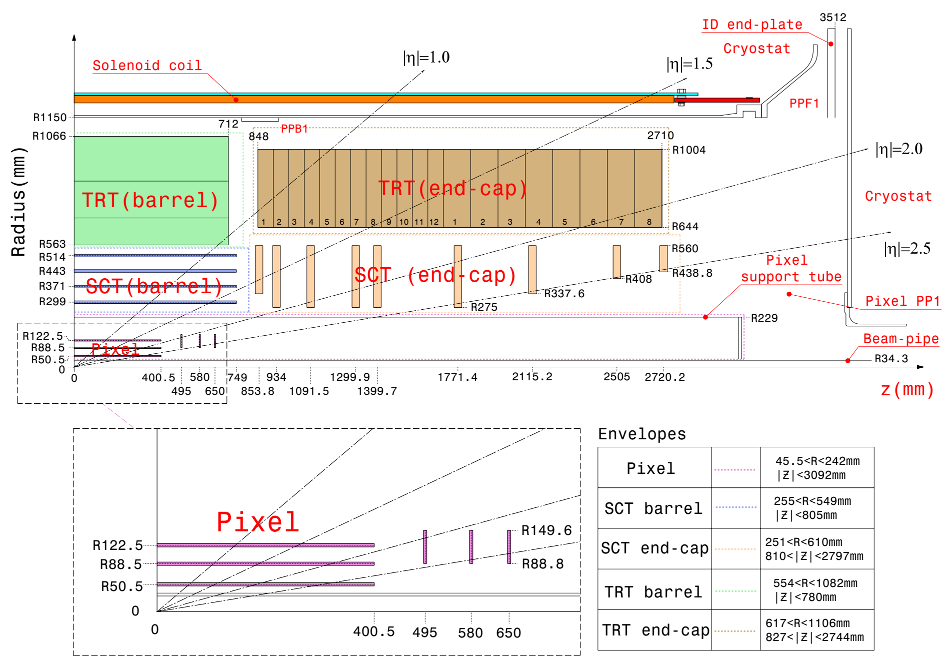

Figure 3.2: *Plan view of a quarter-section of the ATLAS inner detector showing each of the major elements with its active dimensions.*

[]

μm [9]. The pixel detectors use advanced silcon technology which provides excellent radiation hardness.

Outside the pixel detector is the Semiconductor Tracker, where the precise (20 μm) tracking of charged particle continues using layers of silicon microstrip sensors. The silicon covers an area of 60 m^2 *and has over 6 million readout strips connected to custom radiation-hard ASICs. The dissipated power in the detector, up to* $30kW$*, is removed by a cooling system, keeping the silcon temperature at -7°C [10].*

3.4.3 Transition Radiation Tracker

Further from the collision point is the Transition Radiation Tracker which contains hundreds of thousands of gas-filled "straws" held at high voltage, each with a wire down its axis. Charged particles passing through the straw ionize the gas, producing electrical pulses. The timing of the pulse allows the distance between the particle track and the wire to be measured with a precision of $0.17mm$ *[7]. Special materials between the straw tubes cause electrons passing through them to produce X–rays, a feature which helps ATLAS to distinguish electrons from other particles.*

When charged particles pass through, the gas inside the tubes is ionized and a voltage difference between the tube and the anode wire in its center causes the free electrons to drift towards the wire. The drift time is converted into the distance of the track to the wire.

Transition radiation is emitted when highly relativistic charged particles pass the transition between two materials with different dielectric constants. The intensity of the transition radiation photons is proportional to the Lorentz factor of the traversing particle, which is much higher for electrons than for pions, at equivalent energies, due to their mass difference. The gas mixture inside the straw tubes contains xenon, which absorbs the radiation photons and thus produces a signal with a high amplitude when an electron passes through.

The readout electronics of the tubes apply two distinct thresholds: a lower one that detects the ionization clusters and a higher one that is optimized for transition radiation from electrons and allows for rejection of tracks from $\pi^{\pm}$ *background.*

3.4.4 Central Solenoid

The central solenoid is located outside of the Inner Detector. The 5 tonne coil contains $9km$ *of superconducting wire cooled by liquid helium, and an electric current of* $8000A$ *produces a* $2T$ *magnetic field. The powerful magnetic field causes the charged particles to bend. The curvature of these tracks provide important information for determining the momentum and electric charge of each particle.*

3.5 The Calorimeters

3.5.1 Introduction

After having traversed the inner detector, particles enter the calorimeter system, which is situated outside the solenoidal magnet that surrounds the inner detector. It extends from approximately $1.4m$ to $4.2m$ from the interaction point in the transverse plane [8]. Firstly encountered is the electromagnetic calorimeter, which is optimized for the identification and energy determination of photons and electrons. The hadronic calorimeter is dedicated to the reconstruction of hadronic showers from quarks, gluons and hadronically decaying taus. Altogether, the calorimeter system covers the full azimuth and the pseudorapidity range $|\eta| < 4.9$. Muons generally deposit a small fraction of their energy in the calorimeters and continue to be detected by the muon spectrometer. The transverse component of the undetected energy can be estimated by means of the expected energy balance in the transverse plane. The performance of the calorimeters is of direct influence on this quantity, the missing transverse energy. Both the electromagnetic and the hadronic calorimeter consist of sampling detectors, i.e. layers of passive, dense material alternated with layers of active material. The passive material causes incident particles to initiate a shower or cascade of secondary particles, which are detected in the active material. In sufficient successive layers, the primary particle will have transferred all its initial energy. Electromagnetic showers are the result of Bremsstrahlung and e^+e^- pair production and the characteristic interaction distance is the radiation length X_0, the mean distance over which an electron loses all but 1/e of its energy, of the material. Hadronic showers are the result of nuclear interactions and develop over larger distances. The required depth of the material for complete containment of the shower is larger and is expressed in terms of the nuclear interaction length λ of the passive material.

3.5.2 The Electromagnetic Calorimeter

The electromagnetic calorimeter consists of a barrel that covers $|\eta| < 1.475$ and two endcap wheels at $1.375 < |\eta| < 3.200$ [7]. The passive material employed in the electromagnetic calorimeter are lead plates folded into an accordion shape, as illustrated in Figure 3.3. The space between the plates contains a honeycomb structure that is filled with liquid argon. Charged particles produced in showers induce free charge by ionizing the liquid argon, which is collected on the readout electrodes. The barrel component shares its cryostat vessel with the solenoid magnet in order to minimize the amount of inactive material. Between the barrel and each endcap wheel, around $|\eta| = 1.4$, some space is available for cables and services for the inner detector. The thickness of the electromagnetic calorimeter varies from $22X_0$ to $33X_0$. The modules of which the electromagnetic calorimeter is composed are divided into three longitudinal layers.

The front layer is finely segmented in η, which facilitates γ/π^0 separation. The middle layer is thickest and receives the larger part of the energy deposited by electromagnetic showers. The third layer has a coarse granularity and is mainly used to recover the tails of highly energetic electromagnetic showers and to discriminate between hadronic and electromagnetic showers based on the larger energy deposit by the former.

The absorber plates of the Electromagnetic Calorimeter have a unique accordion geometry that provides uniform response over the entire angle of coverage. To read out the more than 100000 channels in the calorimeter, a radiation tolerant readout system was designed that consumes less than $1/10W$ per channel.

3.5.3 The Hadronic Calorimeter

The Hadronic calorimeter surrounds the electromagnetic calorimeter and constitutes a scintillator tile calorimeter at $|\eta| < 1.7$ and two endcap wheels at $1.5 < |\eta| < 3.2$. The tile calorimeter in turn is divided into a central barrel at $|\eta| < 1$ and two extended barrels at $0.8 < |\eta| < 1.7$. The gap in between contains cables, services and power supplies for the inner detector as well as for the electromagnetic calorimeter [7].

The Hadronic calorimeter measures the energies of particles not stopped by the Electromagnetic Calorimeter. In the barrel, the absorber layers are steel. Particle showers are sampled by the tiles of scintillatting plastic which emit light when charged particles pass through them. The light pulses are carried by optical fibres to photomultiplier tubes behind the calorimeter and converted to electronic signals.

3.5.4 Endcap and Forward Calorimeters

In the high radiation level region close to the proton beams, argon calorimeters with copper and tungsten absorbers are used for hadronic energy measurements. These radiation hard detectors extend the acceptance of the ATLAS calorimeter to nearly the full solid angle around the collision point. In order to estimate the missing transverse energy, as large hermetic calorimeter coverage as possible is pursued. The coverage in the very forward region, $3.1 < |\eta| < 4.9$, is provided by three wheels on either side: one electromagnetic component and two hadronic components. With inner radii of approximately $8cm$, they are situated close to the beam and the expected radiation level is high. Closest to the interaction point is the electromagnetic component in which copper acts as the passive material. The two hadronic components employ tungsten and the active material in all three of them is liquid argon. On each side, the forward calorimeter wheels share the liquid argon cryostat with the electromagnetic and hadronic endcaps.

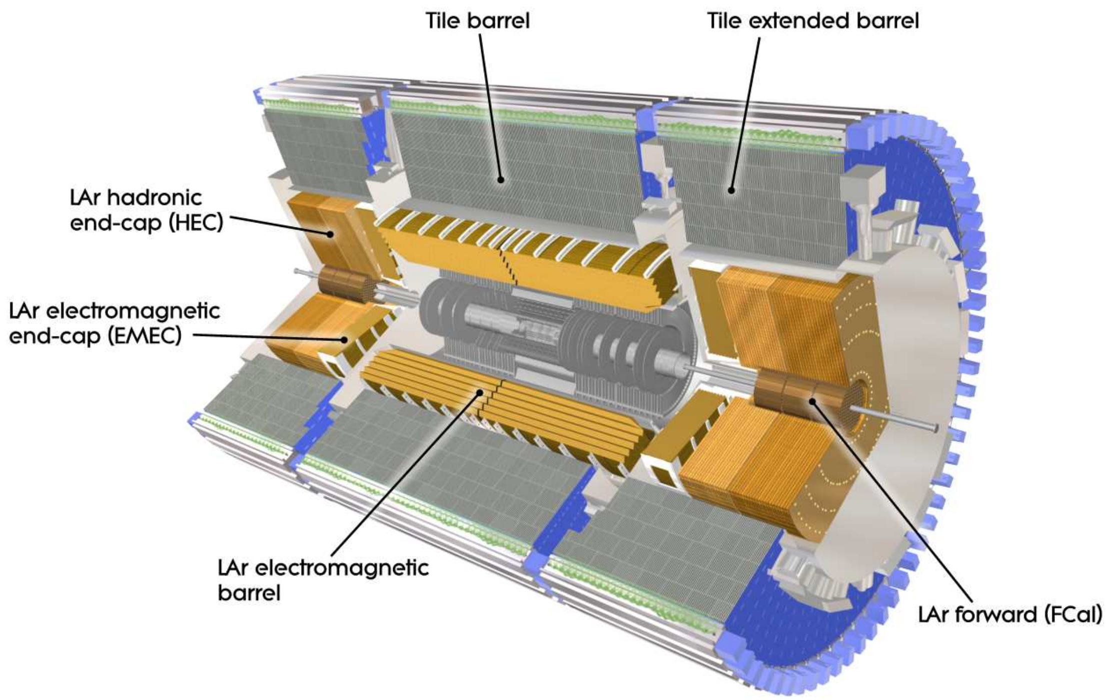

(a)

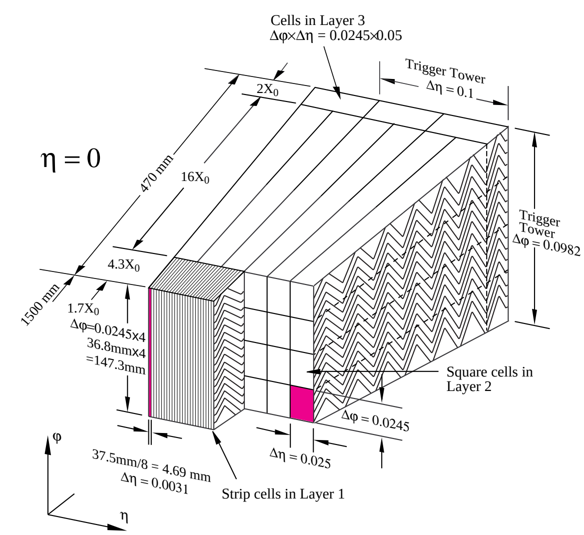

(b)

Figure 3.3: *3.3(a) The ATLAS Calorimeters. 3.3(b) Schematic view of a module in the electromagnetic calorimeter, showing the typical accordion shape and the granularity of the different layers.*

[]

3.6 The Muon Spectrometer

The muon spectrometer is the largest and outermost subdetector of ATLAS. With inner and outer radii of approximately $4.5m$ *and* $11m$ *respectively and stretching out from about* $7m$ *to* $23m$ *from the interaction point on each side in the longitudinal direction, it occupies a volume of around* $16000m^3$ *[7]. It was designed to trigger on muons with high momenta, which play a role as a distinguishing feature in several interesting physics channels, as well as to reconstruct the tracks of muons that pass through with high precision. The components providing the first functionality are the Resistive Plate Chambers (RPC) and the Thin Gap Chambers (TGC), while the latter is achieved by the Monitored Drift Tube (MDT) chambers and the Cathode Strip Chambers (CSC) [1]. A representation of the muon spectrometer is shown in Figure 3.4, indicating the four different types of components. The arrangement is such that a particle originating from the interaction point will traverse three layers of muon stations as it is bended by the magnetic field. The muon spectrometer is designed to measure the electrical charges and momenta of muons. Muons are able to pass through calorimeter without being absorbed. The trajectories of muons are bent by a second set of powerful magnets (after the solenoid magnet), allowing the charges and momenta to be calculated.*

From studies based on 2010 data [16] a systematic uncertainty of $\pm 7\%$ *is assigned to muon reconstruction. This uncertainty is dominated by the dependence of the efficiency on the transverse momenta and the uncertainty on the remaining* π/K *contamination in the data sample where the efficiency is measured. The trigger uncertainty, derived by changing the tolerance on the matching between tracks and trigger signals and comparing measurements obtained in different trigger data streams, found to be* $\pm 2\%$ *[16]. This number is a weighted average of the RPC and TGC trigger efficiency uncertainties, taking into account that there are two muons that can fire the trigger. As far as the energy scale and resolution is concerned, the uncertainty obtained by applying a smearing of MC muon momentum resolution and scale using parameters in agreement with the data (energy scale uncertainty of* 2% *and a resolution uncertainty of* 5% *in the barrel and* 8.5% *in the end–cap [16]). The total systematic systematic uncertainty estimated to be of* $\pm 7\%$ *[16].*

3.6.1 Monitored Drift Tubes (MDT)

MDTs consist of arrays of gas - filled 3cm tubes with anode wires along their axes at high voltage. By measuring the time for electrons produced by ionization to drift to the wires, muon positions can be determined to 80 μm *[1]. In the Barrel, the MDTs are installed as three cylindrical shells. In the End Cap, they form three wheels normal to the axis of ATLAS.*

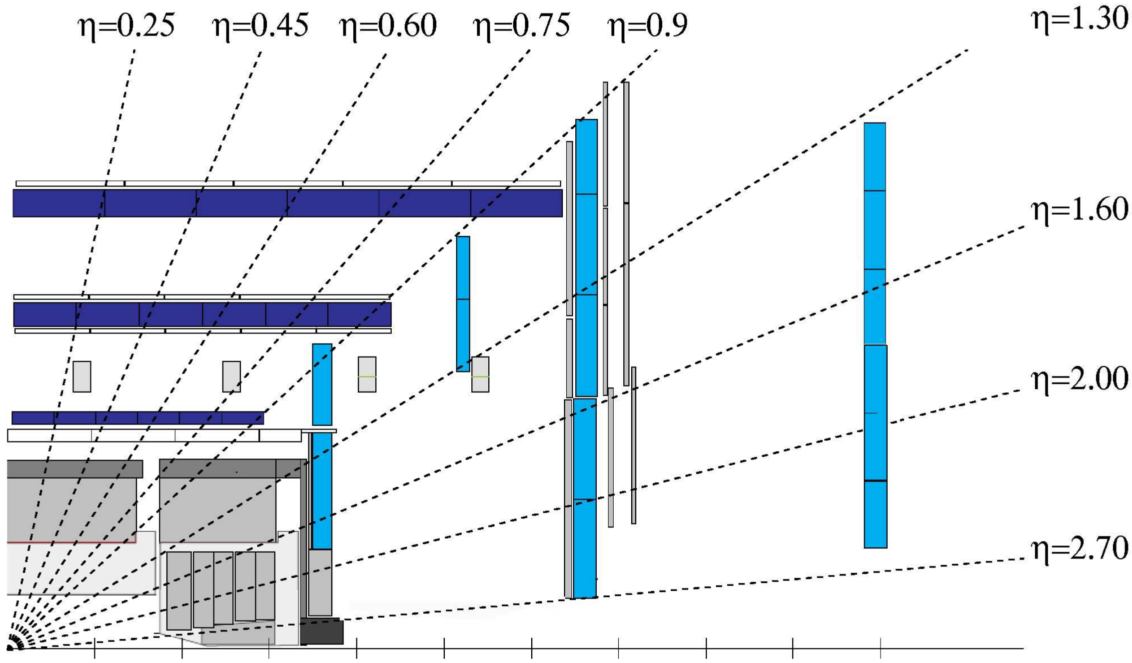

(a)

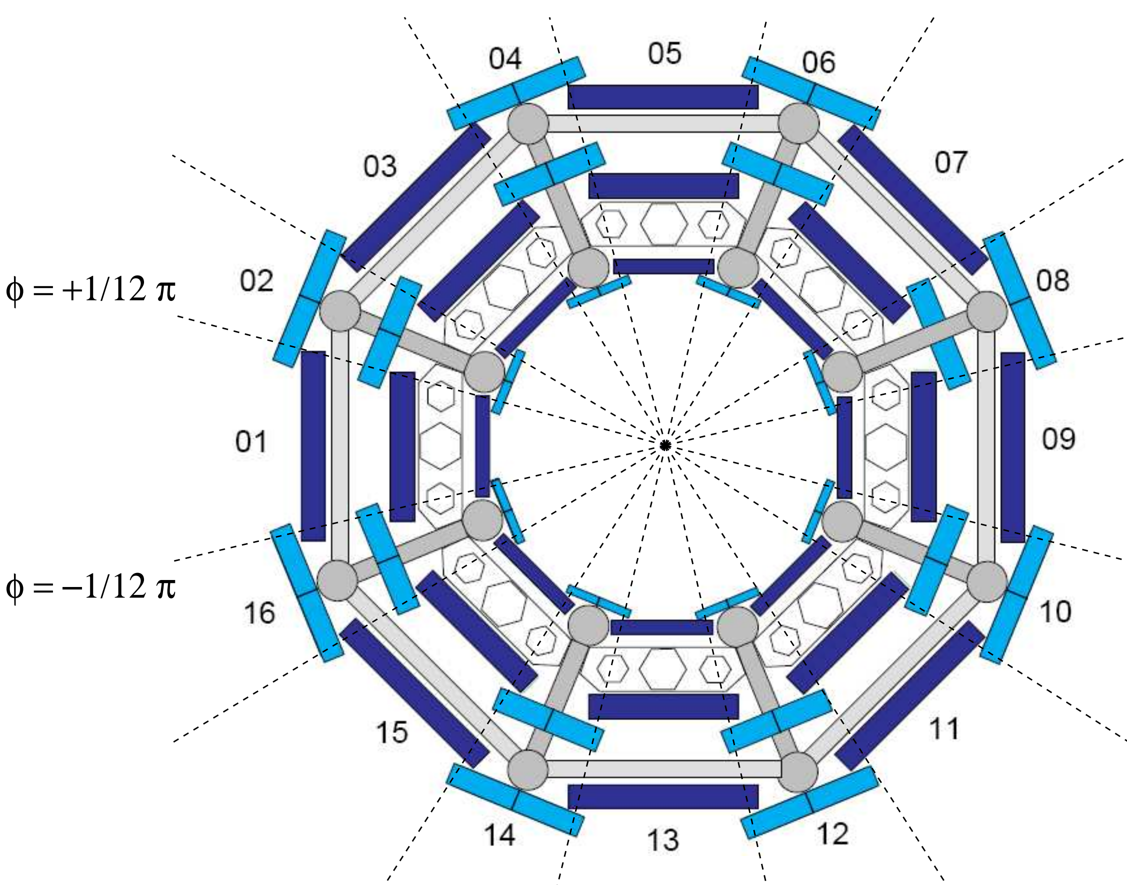

(b)

Figure 3.4: *A schematic view of the η (3.4(a)) and ϕ (3.4(b)) binning of the Muons Spectrometer.*

[]

3.6.2 Cathode Strip Chambers(CSC)

In those parts of the inner layer where the radiation is highest, CSCs are used to measure the muon trajectories. They are thin arrays of closely spaced parallel anode wires located between narrow metal cathode strips. Ionized gas from muons traversing the chamber produce electrical signals on the strips, allowing position measurements at the 60mm level [1].

3.6.3 Thin Gap Chambers(TGC)

The End Cap contains four layers of chambers with closely spaced wires, placed in a thin gap between resistive plates. The ionization signals from the different stations are used to identify the presence of energetic muons every $25ns$*, at each bunch crossing of the beams of LHC [1]. TGCs also furnish coordinates in the non–bending direction.*

3.6.4 Resistive Plate Chambers(RPC)

In the Barrel the trigger is generated by chambers with a narrow gap where ionization by the muon is amplified in a strong electric field to generate signals on external strips. The position of the crossing track is measured with a time resolution of few ns. Three RPC stations are installed together with MDT chambers of the barrel. RPCs also provide second coordinate measurement [7].

3.7 The Magnet System

The ATLAS magnet system generates a magnetic field configuration such that the trajectories of charged particles are bended when traversing the tracking devices, the inner detector and the muon spectrometer. It consists of two superconducting magnet systems, a toroidal system and a central solenoid, that add up to a diameter of $22m$ *and a length of* $26m$ *[1]. The toroidal magnet system provides a magnetic field inside the volume of the muon spectrometer, while the solenoidal magnet generates a homogeneous field parallel to the beam axis inside the inner detector. The curvature of the trajectory followed by a charged particle when passing through the field is used to determine its momentum. A schematic view of the magnetic field is depicted in Figure 3.5.*

3.7.1 Barrel and End–Cap Toroids

In order to produce a powerful field to bend the paths of the muons, the ATLAS detector uses an exceptionally large system of air–core toroids arranged outside the calorimeter volumes. The large volume magnetic field has a wide angular coverage and strengths of up to $4.7T$ *[7].*

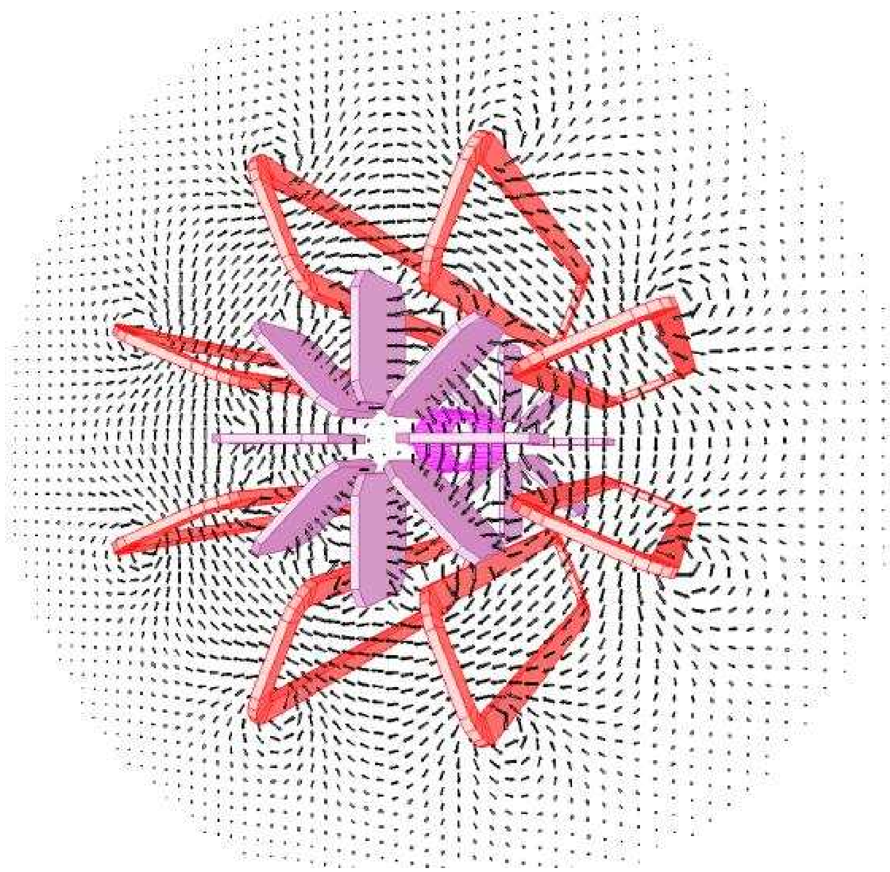

Figure 3.5: *The ATLAS magnetic Field.*
[]

The toroid system contains over $100km$ *of superconducting wire, and has a design current of* $20500A$ *[8].*

3.7.2 The Central Solenoid

The solenoidal magnet system is aligned with the beam axis and produces an axial field throughout the volume of the inner detector. At the $7.730kA$ *nominal operational current, the strength of the field varies from* $2T$ *at the interaction point to* $0.9T$ *[7]. With an axial length of* $5.8m$ *and a diameter of about* $2.5m$*, it is embedded inside the electromagnetic calorimeter. In contemplation of a minimal amount of material in front of the calorimeters, the solenoid shares its cryostat with the electromagnetic calorimeter.*

3.7.3 The Toroidal Magnet System

The toroidal magnet system is built up of a barrel toroid and two endcap toroids. The barrel toroid consists of eight superconducting rectangular coils, each encased in a cryostat. The total assembly weighs 830 *tons and adds up to* $25.3m$ *axial length and inner and outer diameters of* $9.4m$ *and* $20.1m$ *respectively [7]. Cooling down to the nominal operational temperature of* $4.6K$ *takes* 5 *weeks. The field strength provided by the barrel toroid at the nominal operational current of* $20.5kA$ *varies from* $0.15T$ *to* $2.5T$ *[7]. The endcap toroid systems consist of eight coils each, which are located interleaved with the barrel toroid coils on either side, thus generating a magnetic field in the endcap regions of the muon spectrometer. With an inner and outer diameter of* $1.65m$ *and* $10.7m$ *and an axial length of* $5.0m$ *each endcap toroid weighs* 239 *tons. Powered in series with the barrel toroid, the endcap toroids generate a field strength that varies from* $0.2T$ *to* $0.35T$ *at nominal operational current [7].*

3.8 Data Acquisition and Computing

ATLAS is designed to observe up to nearly one billion proton–proton collisions per second, with a combined data volume of more than 60 *million megabytes per second [1]. However, only a few of these events will contain interesting characteristics that might lead to new discoveries.*

To reduce the flow of data to managale levels, ATLAS uses a specialized multi–level computing system, the Trigger system, which selects events with distinguishing characteristics that make them interesting for physics analyses [2].

3.8.1 The trigger system

Trigger is a system that uses simple criteria to rapidly decide which events in a particle detector to keep when only a small fraction of the total can be recorded. Trigger systems are necessary due to real–world limitations in data storage capacity and rates. Since experiments are typically searching for "interesting" events that occur at a relatively low rate, trigger systems are used to identify the events that should be recorded for later analysis. The ratio of the trigger rate to the event rate is referred to as the selectivity of the trigger. For example, the Large Hadron Collider has an event rate of $1GHz$*, and the Higgs boson is expected to be produced there at a rate of at least* $0.01Hz$ *[1].*

Triggers usually make heavy use of a parallelized design, exploiting the symmetry of the detector: the same operation may be performed at the same time on different parts of the detector. Yet on a global scale they are essentially serial devices: in fact, they are usually divided in "levels". The idea is that each level selects the data that becomes an input for the following, which has more time available and more information to take a better decision.

Custom hardware processors make an initial decision to keep an event in a few μs *using coarsely segmented data from a subset of the detectors, while holding all the high–resolution data in pipelined memories. Commodity processors make subsequent decisions using more detailed information from all of the detectors in more sophisticated algorithms that eventually approach the final reconstruction.*

Each detector has its own trigger design and features. The ATLAS trigger system carries out the selection process in three stages, the first level (L1) is hardware-based and uses a coarse detector information, while the next two levels are based on the software algorithms and high-granularity detector information for a stricter selection of interesting events.

The Level–1 trigger is a massively parallel system of specialized electronics that process a coarse subset of the data from every 25ns beam crossing interval. A decision to keep the data from an event is made less than two microseconds after the event occurred, and the event is then retrieved from pipelined storage buffers. Of 40 *million bunch crossings per second, less than* 100000 *pass Level–1 [1].*

The Level–2 trigger is a large array of custom processors that analyse in greater detail specific regions of interest defined by the Level-1 system for each event [1]. In the mean time, the full event data is collected into buffers. Fewer than 1000 *events per second pass Level–2, and have their data passed on the Level–3.*

In the Level–3 trigger, usually referred as "Event Filter" (EF), a detailed analysis on the full event data is applied. Less than 100 *events per second are left after the Level–3 analysis, and these are passed on to a data storage system for offline analysis.*

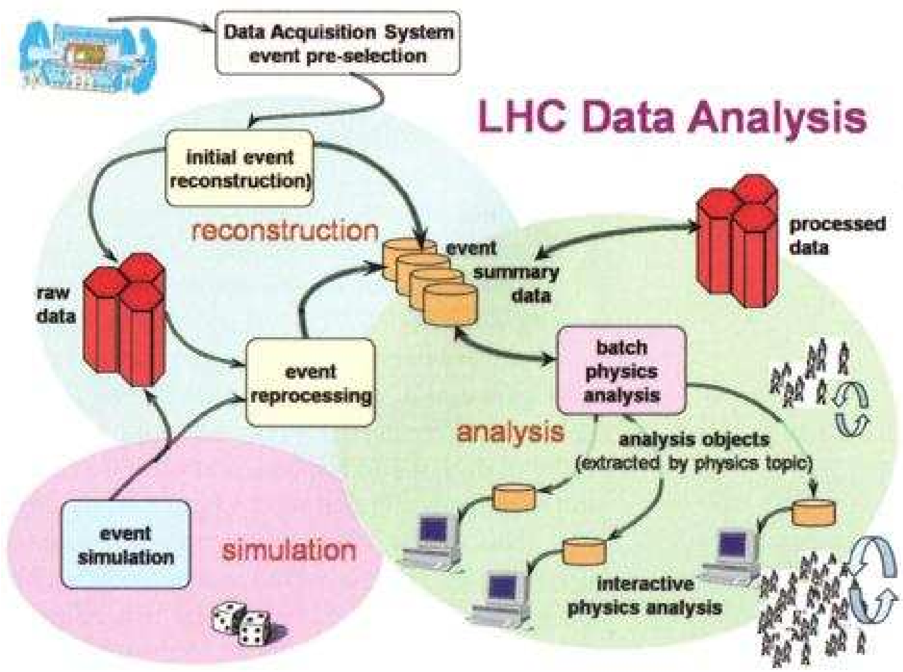

Figure 3.6: *A high-level view of the data flow and the principal processing stages involved in this process.*

Bibliography

[1] ATLAS Collaboration, ” The ATLAS Experiment at the CERN Large Hadron Collider”, PUBLISHED: August 14, 2008, Institute of Physics Publishing and SISSA

[2] ATLAS Collaboration, ” Technical Challenges of ATLAS”

[3] N. Berger, T. Bold, T. Eifert, G. Fischer, S. George, J. Haller, A. Hoecker, J. Masik, M. zur Nedden, V. Perez Reale, C. Risler, C. Schiavi, J. Stelzer, X. Wu, ”The High-Level-Trigger Steering of the ATLAS experiment”, ATL-COM-DAQ-2007-020

[4] Lyndon Evans, ”The Large Hadron Collider: a Marvel of Technology ”, CERN and EPFL Press (2009)

[5] Taking a closer look at ATLAS

[6] Manouk Rijpstra, ”The Top and Beyond, Missing Energy and Little Higgs in ATLAS”, CERN-Theses 2011-005

[7] ATLAS collaboration, ”ATLAS Detector and Physics Performance Technical Design Report Vol I”, CERN-LHCC-99-14, 1999

[8] ATLAS collaboration, ”ATLAS Detector and Physics Performance Technical Design Report Vol II”, CERN-LHCC-99-15, 1999

[9] ATLAS collaboration, ”Inner Detector Technical Design Report Vol I”, CERN-LHCC-97-16, 1997

[10] ATLAS collaboration, ”Inner Detector Technical Design Report Vol II”, CERN-LHCC-97-17, 1997

[11] ATLAS collaboration, ”Liquid Argon Technical Design Report”, CERN-LHCC-96-41, 1996

[12] ATLAS collaboration, ”Tile Calorimeter Technical Design Report”, CERN-LHCC-96-12, 1996

[13] A. Artamonov et al., ”The ATLAS Forward Calorimeter JINST 3”, 2008

[14] J.Barriere et al, "The alignment system of the ATLAS barrel muon spectrometer", ATL-MUON-PUB-2008-007, 2008

[15] C. Amelung et al, "The Optical Alignment System of the ATLAS Muon Spectrometer Endcaps", ATL-MUON-PUB-2008-003, 2008

[16] ATLAS Collaboration, "Measurement of the $Z \to \ell\ell$ production cross section in proton–proton collisions at $\sqrt{s} = 7TeV$ with the ATLAS detector", ATL-COM-PHYS-2010-546

Chapter 4

Data Driven Estimation of $ZQQ \rightarrow Z\mu\mu$ Background

4.1 Introduction

The decay channel $H \rightarrow ZZ^{(*)} \rightarrow 4\ell$, where $\ell = e, \mu$, is one of the experimentally cleanest signatures for the search of the Standard Model Higgs boson. The main backgrounds to the $H \rightarrow ZZ^* \rightarrow 4\ell$ search at LHC is the irreducible $ZZ^*/\gamma^* \rightarrow 4\ell$, while the reducible backgrounds are mainly $Z + QQ$ (Q=b or c), $t\bar{t}$, and $Z + light\, jets$ with one or more "fake" leptons in the final state.

For the high mass region, $M_H > 180GeV$, the two on-shell Z bosons from the Higgs decay allow for a selection which strongly suppresses the reducible backgrounds leaving only the irreducible $ZZ \rightarrow 4\ell$ component. At low Higgs masses, where one of the decay bosons is off-shell, contributions from $Z + jets$ and $t\bar{t}$ can be significant and tighter cuts are therefore applied to reduce these backgrounds to a level safely below the ZZ^* continuum.

This analysis presents a search for $Z + \mu^+\mu^-$ events using the first $43pb^{-1}$ of pp collisions at the LHC at $\sqrt{s} = 7TeV$ with the ATLAS detector. Events with a dilepton pair consistent with a Z decay, both $Z \rightarrow \mu^+\mu^-$ and $Z \rightarrow e^+e^-$ decays, are studied. With this search, which is using the same selection criteria with $H \rightarrow 4\ell$ analysis, the $Z+$ heavy quark background is measured in a control region and it is compared with the corresponding Monte Carlo expectation. Further more, because of the low statistics of these early data, the $Z + \mu$ final state is also studied, allowing for more quantitative comparison of the different muon components in data and MC.

Finally, the efficiency of the additional muon selection criteria is investigated using a tag and probe like method on muons originating from Z decays.

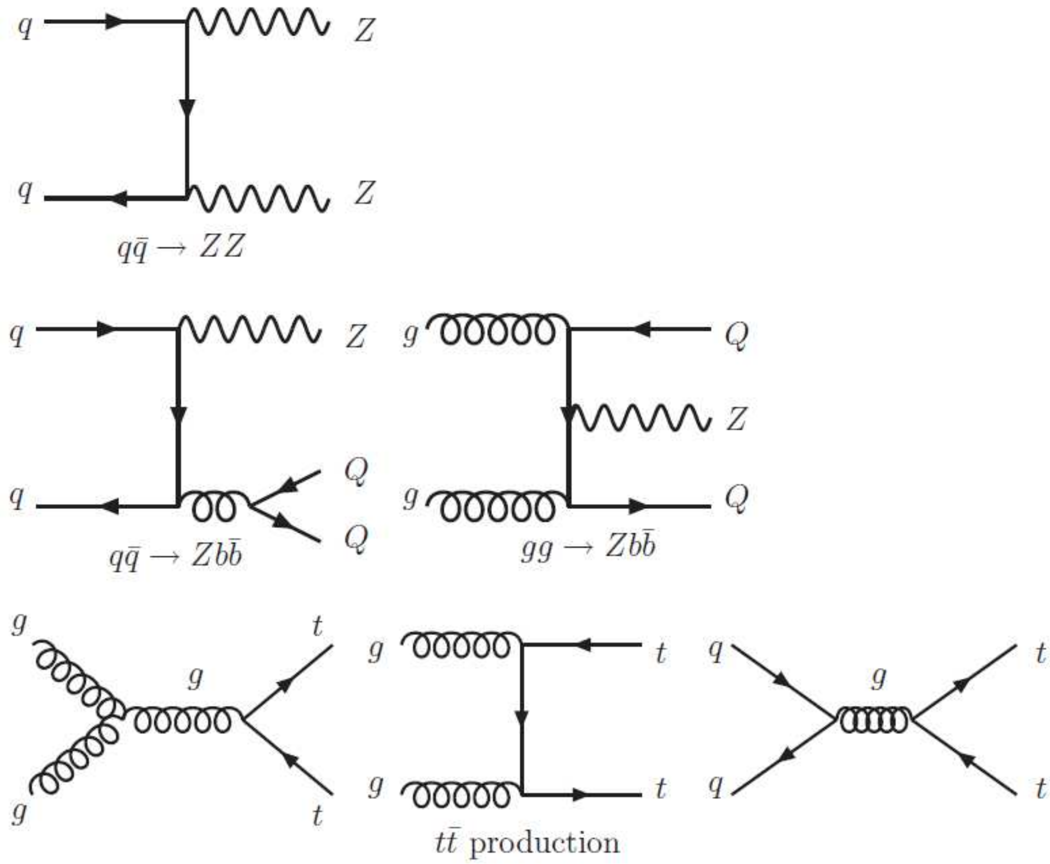

Figure 4.1: *Feynman diagrams of the ZZ, Zbb and $t\bar{t}$ production at the LHC.*
[]

4.2 MC Samples

The MC samples used for this analaysis, described detailed in Appendix A, include $Z \rightarrow \mu^+\mu^-$ and $Z \rightarrow e^+e^-$ samples generated by "Pythia 6.4" [1]. Though, cross checks were made using "Sherpa"[2], "MC@NLO"[3] and "ALPGEN" [4] generators. The results obtained from the previous are compatible with each other. "Pythia" generators also used for ZZ, bb, cc, $Z \rightarrow \tau\tau$ and Higgs with different masses processes. For the $t\bar{t}$ background the "MC@NLO" generator is used. Next–to– next–to leading order cross–section used for the simulation scaling to the data luminosity. The feynman diagrams of the production mechanisms of the backgrouns are illustrated in Figure 4.1 and the corresponding cross sections are presented on Table 4.1. The pile up setup is bunch train with double trains of 225ns separation, within trains are 8 filled bunches with 150ns bunch separation [11]. As a result, the MC samples are reweighted to reproduce the vertex multiplicity observed in the data, see Table 4.2.

Sample	Cross Section
$H \rightarrow ZZ \rightarrow 4\ell(M_H = 120GeV)$	1.37 fb
$Z \rightarrow \ell\ell$ (PYTHIA)	0.989 nb
$Z \rightarrow \ell\ell bb + 0\, parton$ (ALPGEN)	7.95 pb
$Z \rightarrow \ell\ell bb + 1\, parton$ (ALPGEN)	3.01 pb
$Z \rightarrow \ell\ell bb + 2\, parton$ (ALPGEN)	0.986 pb
$Z \rightarrow \ell\ell bb + 3\, parton$ (ALPGEN)	0.472 pb
ZZ (PYTHIA)	1.02pb
$t\bar{t}$	164.6 pb

Table 4.1: *Cross sections of the MC used for the analysis [5]. NNLO used except from the $t\bar{t}$ which is leading order logarithm approach.*

N_{vtx}	Reweight
1	1.90
2	1.21
3	0.86
4	0.66
5	0.58
6	0.47
7	0.54
$\geq$8	0.32

Table 4.2: Pile-up reweight as a function of the number of primary vertices, N_{Vtx}. All events with 8 or more vertices are grouped in the last category, owing to lack of statistics.

4.3 Lepton Definition

This section contains a brief introduction to the muon and electron identification and reconstruction algorithms.

4.3.1 Muon Reconstruction And Identification

There are four basic algorithms for the muon reconstruction available:

- *Stand - alone: this reconstruction is based on the muon spectrometer information, independently of the inner detector. It is initiated locally in a muon chamber by a search for straight line track segments in the bending plane. A minimum of two track segments in different muon stations are combined to form a muon track candidate using three - dimensional tracking in the magnetic field. The track parameters are obtained from the muon spectrometer track fit and are extrapolated to the interaction point taking into account both multiple scattering and energy loss in the calorimeters.*

- *Combined muons: this reconstruction associates a previously defined Stand–Alone muon spectrometer track to an inner-detector track, by performing a χ^2-test, defined by the difference between the respective track parameters weighted by their combined covariance matrices. The parameters are evaluated at the point of closest approach to the beam axis. The track parameters are derived from a statistical combination of the two tracks or the refit of the ID and MS hits associated with the track.*

- *Tagged muons: this reconstruction algorithm propagates all inner detector tracks with sufficient momentum out to the first station of the muon spectrometer and searches for nearby track segments in the muon chambers. If a segment is sufficiently close to the predicted track position, then the inner detector track is tagged as corresponding to a muon.*

- *Calo Muons: Muons traverse the Inner Detector and the calorimeters in the ATLAS experiment before reaching the Muon Spectrometer. The material thickness traversed by the muons is over 100 radiation lengths (X_0), as presented in Figure 4.2 [17]. By passing through this material, muons undergo electromagnetic interactions which result in a partial loss of their energy. As over 80% of this material is in the instrumented areas of the calorimeters, the energy loss can be measured. Calorimeter tagging algorithms identify inner detector tracks using the distinctive energy deposition pattern associated to minimum ionising particles and by those procedures calo muons are identified. Muon identification in the calorimeters can be used to recover low momentum ($P_T = 2 - 5GeV/c$) muons, which produce marginal activity in the muon spectrometer.*

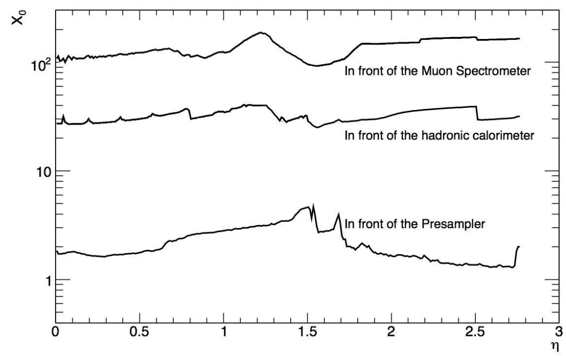

Figure 4.2: *Material distribution before the Muon Spectrometer in ATLAS as a function of h. The material is expressed in radiation lengths (X_0) [8].*

[]

The combined and segment - tagged muons are used for this study. Efficiency checks using data from dimuon decays of the J/ ψ mesons and Z bosons, proved that using combined and segment-tagged muons leads to an agreement between data and MC efficiencies of better than 1 % and as a result no efficiency correction is needed [11].

Inner Detector (ID) Track Requirements for Muon Identification

A series of cuts are applied to muon candidates in order to ensure the quality of the reconstructed muons and as a result of the selection. These cuts are presented in Table 4.3 and the efficiency of this selection is 96% [16].

Requirements	
$\|\eta\|$	≤ 2.5
Hits	$N_{B-Layer\,Hits} > 0$ when B - Layer Hit expected $N_{Pixel\,Hits} + N_{Crossed\,Dead\,Pixel\,Sensors} > 1$ $N_{SCT\,Hits} + N_{Crossed\,Dead\,SCT\,Sensors} \geq 6$ $N_{Pixel\,Holes} + N_{SCT\,Holes} < 2$
TRT extension	${n_{TRT}}^{hits}$ = the number of TRT hits on the muon track ${n_{TRT}}^{outliers}$ = the number of TRT outliers on the muon track n = ${n_{TRT}}^{hits} + {n_{TRT}}^{outliers}$
if $\|\eta\|$ <1.9	$n > 5$ and ${n_{TRT}}^{outliers} > 0.9n$
if $\|\eta\|$ ≥1.9 and $n > 5$	${n_{TRT}}^{outliers} > 0.9n$

Table 4.3: *ID track Requirements for muon identification*

.

4.3.2 Electron Reconstruction and Identification

Electrons consist of electromagnetic clusters to which inner detector tracks are matched in a broad window between the cluster position and the extrapolated track. The baseline electron identification relies on cuts using variables that provide good separation between isolated electrons and jets. These variables include calorimeter, tracker and combined calorimeter/tracker information. They can be applied independently and three reference sets of cuts have been defined with increasing background rejection power: loose, medium *and* tight. *In more details [9]:*

- Loose: *A set of cuts performs a simple electron identification based only on limited information from the calorimeters. Cuts are applied on the hadronic leakage and on shower-shape variables, derived from only the middle layer of the EM calorimeter. This set of cuts provides excellent identification efficiency, but low background rejection.*

- Medium: *By adding cuts on the strips in the first layer of the EM calorimeter and on the tracking variables, an effective rejection of $\pi^0 \to \gamma\gamma$ decays is achieved. Since the energy-deposit pattern from π^0's is often found to have two maxima due to $\pi^0 \to \gamma\gamma$ decay, showers are studied in a window $\Delta\eta \times \Delta\phi = 0.125 \times 0.2$ around the cell with the highest E_T to look for a second maximum. If more than two maxima are found the second highest maximum is considered. The tracking variables include the number of hits in the pixels, the number of silicon hits and the tranverse impact parameter. The medium cuts increase the jet rejection by a factor of 3-4 with respect to the loose cuts, while reducing the identification efficiency by 10%.*

- Tight: *Additional cuts are applied on the number of vertexing-layer hits (to reject electrons from conversions), on the number of hits in the TRT, on the ratio of high-threshold hits to the number of hits in the TRT (to reject the dominant background from charged hadrons), on the difference between the cluster and the extrapolated track positions in η and ϕ , and on the ratio of cluster energy to track momentum. Two different final selections are available within this tight category: they are named tight (isol) and tight (TRT) and are optimised differently for isolated and non-isolated electrons. In the case of tight (isol) cuts, an additional energy isolation cut is applied to the cluster, using all cell energies within a cone of $\Delta R < 0.2$ around the electron candidate. This set of cuts provides the highest isolated electron identification and the highest rejection against jets. The tight (TRT) cuts do not include the additional explicit energy isolation cut, but instead apply tighter cuts on the TRT information to further remove the background from charged hadrons.*

Since the very early data taking periods, Data and MC comparisons on electrons from W and Z decays, have revealed some discrepancies in the shower shape distributions [9]. In order to maintain the robustness of the electron identification criteria the cut values used on the shower shapes are placed on the tail of the relevant distributions from data, thus maitaining high identification efficiency and reducing systematics [9]. This is called the "Robust" selection. An electron candidate may be found with the standard (cluster based) and softe (track based) algorithm, which is referred as "author" variable. For this study, candidates found by at least the standard algorithm and fulfilling robust medium selection are used [9].

Dead Calorimeter Regions - OTx Maps

Signals from the Liquid Argon Calorimeter are amplified, shaped and digitized on the front-end boards located on the detector. The digital data are then transferred through over 1700 optical links to the back-end electronic system located about 120 meter away for further processing. In each optical link, optical transmitter (OTx) converts the signals from electrical into optical form and sends them out through optical fiber. In each optical link the data of 128 channels are transmitted, if one optical link fails that leads to data loss of these channels. The front end borders are organised by calorimeter layers and therefore always correspond to the same layer. During the 2010 data taking period there were OTx failures in all 4 layers (presampler, first, second and third). Since electromagnetic cluster building is based on the second layer, electrons falling into a dead OTx region in the second layer are therefore unrecoverable [5]. Losses in the presampler and first layer are in principle recoverable but special energy corrections are needed. These corrections are available only for the presampler at present. In this analysis, the affected regions are excluded by applying an acceptance map on the data and MC (where only a fraction of dead regions are simulated). This results in an acceptance loss of 9% per electron. The back layer has very little impact on efficiency and energy measurements and it is therefore included without corrections. All dead and weak optical links were replaced in the 2010-2011 winter shut down, while the failure pattern is understood and appropriate measures have been taken. All affected regions of the calorimeter are thus expected to be recovered for the 2011 run.

Electron Requirements

Electron candidates should pass the selection presented in Table 4.4, in order to be considered as quality candidates. The efficiency of this selection is estimated to be 90% [9].

Electron Requirements	
Candidates	Excluded those from dead calorimetric Regions
author	1 or 3
$\|\eta\|$	≤ 2.47 (including crack region)
isEM	true
Reconstruction	Robust Medium

Table 4.4: *Electron Requirements*

.

4.4 Muon Additional Selection Criteria

The final state of $Z + \mu\mu$ accepts significant contribution from $Z + jets$ and $t\bar{t}$ backgrounds. In order to reduce them below a safety level additional lepton selection, to those previously described, is required. Isolation and impact parameter criteria are used for further background rejection [8].

4.4.1 Lepton Isolation

$Z + jets$ and $t\bar{t}$ are the most important reducible backgrounds of our study. The heavy quark decays are expected to originate from secondary vertices and appear in a jet environment, since b and c quarks live long enough to decay at some distance from the interaction point. Additional contaminating sources are the light quark jets (pion or kaon decays and punch-through hadrons) and $t\bar{t}$ decays. Muons coming from the latter interactions are in general consistent with originating from secondary verteces. Muons that originate from light quark jets populate in general the low P_T spectrum and are characterized by relatively large difference between the transverse momenta measured in the inner detector and the muon spectrometer. In addition, such muons are not isolated. As opposed to these, the prompt muons from W or Z boson decays have on average just the opposite properties except that they originate from the interaction point. The muons in $t\bar{t}$ decays originate either from W or from b–quark decays, sharing the corresponding characteristics.

Muon isolation requirement can be separated into two types: calorimeter-based and track-based. The calorimeter isolation is determined by defining a cone around the muon trajectory with a minimum and maximum radius, so the cells, where the muon deposits its energy, can be excluded. The size of the inner radius must be optimised to collect most of the energy deposited by the muon and as little as possible from other particles. The energy deposited between the inner and outer radius is then the isolation energy. Track-based isolation is a very useful variable, as it has been shown to provide a better signal background discrimination [8], and can be used either together with or as *an alternative to calorimeter based isolation since the two are statistically independent as the information is provided by different parts of the detector.*

Isolation variables

The E_T measured in the electromagnetic calorimeter within a cone around the lepton (ΣE_T) can be used as a standalone parameter. This variable is often referred to as the isolation energy. It can be based on energy measurements or the sum of P_T from all tracks within the given cone. The relative isolation energy, where the isolation energy is divided by the total combined lepton P_T, is also a usefull parameter since it allows for a cut yielding even better isolation. The value in the cone is assumed to be energy of the lepton subtracted the value of other particles in the cone, this value can be negative for muons. For this reason, the number of tracks around the reconstructed lepton is used as an isolation variable for the muon and respectively the relative track isolation, is defined as the ratio of the sum of the transverse momenta of the Inner Detector tracks in a cone of radius $\Delta R = \sqrt{\Delta\eta^2 + \Delta\phi^2} < 0.3$ around the lepton over the lepton P_T. In order to minimize secondary, out of interest, ineractions (pile - up effect) vertex proximity criteria and a P_T threshold of $1GeV$ are applied.

The imposal of calorimetric and track isolation on muons reduces drastically the reducible backgrounds, including the "fake" muons of the $Z + jets$ background. As an example the distributions of the isolation variables used in this analysis for muons originating from Higgs decays as well as muons originating from jets are shown in Figure 4.3. The isolation distributions of the a $H \rightarrow 4\ell\,(M = 120GeV)$ and a dijet sample are presented. It can be observed that the signal peaks at 0 whereas the backgrounds extends to higher values.

4.4.2 Impact Parameter Criteria

Due to the apreciable life time of the b–hadrons, some of the leptons from the $Zb\bar{b}$ and $t\bar{t}$ processes are expected to originate from displaced vertices, which can be used to further reject the reducible backgrounds. The impact parameter significance, defined as the impact parameter of the lepton normalised to its measurement error, is required not to exceed a predefined value. In Figure 4.4 where the distributions of a $H \rightarrow 4\ell\,(M = 120GeV)$ and a dijet sample are presented, it shows how this requirement rejects the background [8].

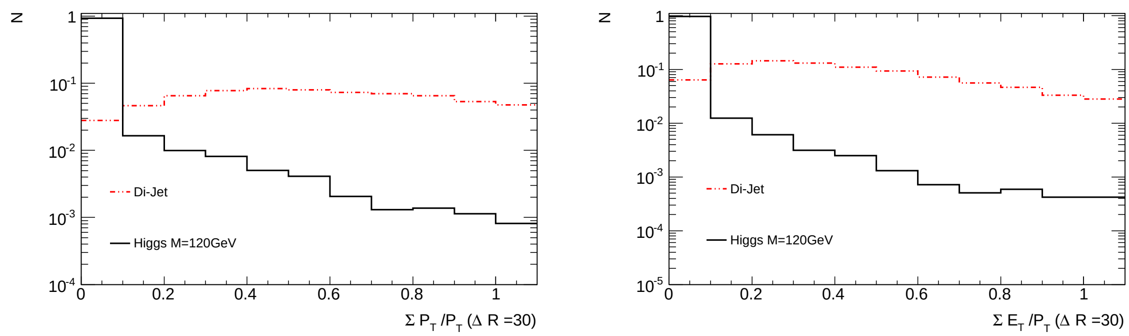

(a) (b)

Figure 4.3: *4.3(a) Track - based and 4.3(b) calorimetric isolation distributions in cone* $\Delta R = 0.3$ *for muons originating from Higgs decays and jets. The isolations cuts at low values of the relative isolation variable suppress the background.*

[]

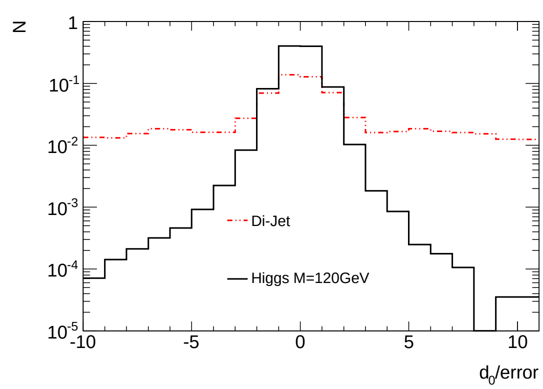

Figure 4.4: d_0 *significance distribution of muons from Higgs decays and muons from jets. The application of this cut leads to background rejection.*

[]

4.5 Event Preselection

4.5.1 Data Quality - GRL

This study uses data collected at a center of mass energy of $\sqrt{s} = 7TeV$ in proton–proton collisions by the ATLAS experiment from March 30 until October 31, 2010 (data–taking periods A to I2). The data analysed passes the "Good Runs List" (GRL) selection, for which the LHC declared stable beams and the ATLAS detector was at nominal high voltage. In addition, the GRL selection required the solenoid and toroid elds to be both on and at nomimal conditions for good muon and electron momentum measurements. The sub-detectors were also recording good data quality so that the electron and muon identfication and reconstruction algorithms were oparating as expected. The corresponding total integrated luminosity after the data quality selection applied in this analysis is $43.32pb^{-1}$ for the muons channel and $38.85pb^{-1}$ for the $2e2\mu$ channel, as determined by the standard ATLAS tool for luminosity calculation [18].

4.5.2 Trigger

The trigger requirements change as a function of increasing instantanous luminosity. Events for the present analysis are selected by the triggers of Table 4.5, which correspond to the lowest unprescaled triggers [12].

Run Numbers (R)	Muons Stream Trigger	Egamma Stream Trigger
$R < 160899$	L1_MU10	L1_EM14
$160899 \leq R < 165703$	EF_mu10_MG	L1_EM14
$165703 \leq R < 167607$	EF_mu13_MG	EF_e15_medium
$R \geq 167607$	EF_mu13_MG_tight	EF_e15_medium

Table 4.5: *Triggers used for the different data taking periods for the muons and electrons channels analysis*

Level 1 (L1) muon trigger searches for patterns of hits in three trigger stations within $|\eta| < 2.4$. The algorithm requires the hits in the different trigger stations to coincide with a road which tracks the path of a muon from the interaction point through the detector. The width of the road is related to the P_T threshold to be applied, which is set to 10 GeV (L1_MU10 trigger selection) or 14 GeV(L1_EM14).

The High Level Trigger (HLT) is a software based trigger, running on farms built from commodity computing and network technology. It is subdivided into LVL2 and the Event Filter (EF). The EF can take around 1s and should further reduce the rate to $\sim$ 200 Hz. Both levels have access to the full granularity of all the detector data and follow the principle of further refining the signatures identified at LVL1, see Figure 4.5. The EF_mu10_MG match reconstructed muon to EF muon object with $dR < 0.3$ and

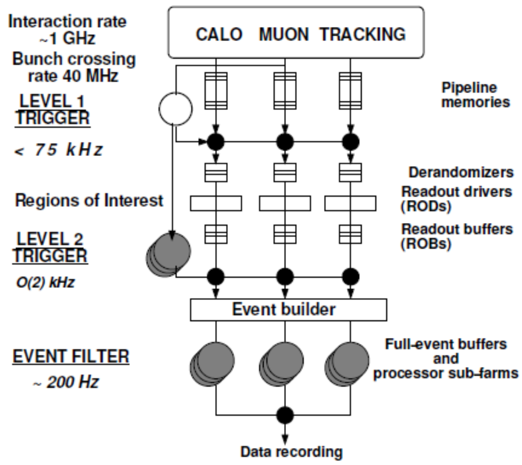

Figure 4.5: *Sketch of the ATLAS T/DAQ system. The places where the HLT and thus the HLT Steering is deployed (LVL2/EF) are marked in grey.*

[]

a P_T threshold of 10GeV, whereas EF_mu13 triggers have a threshold set to 13GeV. EF_e15_medium corresponds to medium electrons with P_T above 15 GeV.

4.5.3 Leading Dilepton Selection

The event candidates are formed by selecting two opposite sign, same flavour di–leptons in an event. The leading di–lepton, Z_1, is defined as the one with invariant mass $M_{\ell_1\ell_2}$ closest to the nominal Z boson mass. Out of all possible remaining lepton pairs, the second di–lepton, Z_2, is chosen to have the invariant mass closest to the nominal Z mass.

An initial selection requires the trigger criteria described in 4.5.2, a primary vertex with at least three tracks associated to it and at least two same flavor leptons. The rest of the selection is different for the $Z \rightarrow e^+e^- + \mu\mu$ and $Z \rightarrow \mu^+\mu^- + \mu\mu$ channels and is described in details in the following subsections. Note that each lepton candidate should be in well seperated from the other leptons of the event ($DR \geq 0.1$).

$Z_{12} \rightarrow \mu^+\mu^-$

For the leading case of $Z \rightarrow \mu^+\mu^-$, the ID track requirements for muon identification, see Table 4.3 are applied to each muon of the dimuon pair. This selection requires $|\eta| \leq 2.5$, the number of Pixel hits and crossed dead Pixel sensors to be greater than one, similar requirement is applied to the SCT hits and the SCT dead sensors, a Pixel b–layer hit on the muon except the extrapolated muon track passed an uninstrumented

<table>
<tr><th></th><th>$Z \rightarrow ee$</th><th>$Z \rightarrow \mu\mu$</th></tr>
<tr><td>Primary vertex</td><td>$\mathrm{N_{vtx}} \geq 1$ with $\mathrm{N_{trks}} \geq 3$</td><td>$\mathrm{N_{vtx}} \geq 1$ with $\mathrm{N_{trks}} \geq 3$
$|Z_{vtx}| < 150$ mm</td></tr>
<tr><td>Trigger</td><td colspan="2">Based on the increasing instantanous luminosity</td></tr>
<tr><td rowspan="3">Z_{12}</td><td colspan="2">$P_T > 20GeV$</td></tr>
<tr><td>robust Medium
$|\eta| \leq 2.47$
author=1 or 3</td><td>Combined or Segment Tagged
$|\eta| \leq 2.5$
B-layer Hit when expected
successful TRT extension
Pixel and SCT hits
Impact Parameter Criteria</td></tr>
<tr><td colspan="2">Track Iso $(30)/P_T \leq 0.2$
Calo Iso $(30)/P_T \leq 0.3$
opposite charge
$|M_{12} - M_Z| \leq 15GeV$</td></tr>
<tr><td>Additional Muons</td><td colspan="2">$P_T > 3GeV$
Combined or Segment Tagged
$|\eta| \leq 2.5$
B-layer hit when expected, successful TRT extension
Pixel and SCT hits</td></tr>
</table>

Table 4.6: *Summary of the event selection criteria*

.

or dead area of the b–layer, SCT holes and Pixel holes to be less than two and a successful TRT extension where expected. In addition to the ID qualiity requirements a selection similar to The Higgs selection is applied. This requires a P_T threshold of $20GeV$, combined or segment tagged muons, a relative track isolation in cone 30 less than 0.20 and relative calorimetric isolation at cone $\Delta R = 30$ less than 0.30, impact parameter criteria, opposite sign charges for the dimuon pair and mass close to the Z mass within a range of $15GeV$, see Table 4.7. The selection is such that it suppreses the $t\bar{t}$ background without affecting the signal. Note that the calorimetric isolation affects less than 1% the signal and for that reason is not applied in the rest of the analysis.

Applying the above selection for the $l_1 l_2$, the mass distribution before the mass cut is presented in Figure 4.6, the Z peak is apparent with negligible background.

$Z_{12} \rightarrow e^+e^-$

A similar procedure is perfomed for the case where Z_{12} decays to electrons. The electrons selection requires the electron quality requiremenrs discussed in section 4.4 and

$H \rightarrow 4\ell$ Selection Criteria	
P_T	$> 20GeV$
Track Iso $(30)/P_T$	≤ 0.2
Calo Iso $(30)/P_T$	≤ 0.3
Reconstruction	Combined / Segment Tagged
$Z_0(PV)$	$\leq 10mm$
$d_0(PV)$	$\leq 1mm$
Charge	opposite
Mass $\ell_1\ell_2$	$\lvert M_{12}\rvert \leq 15GeV$

Table 4.7: Higgs ($H \rightarrow 4\ell$) Selection Criteria for muons of the primary dilepton
.

the Higgs selection. The former reccomendation, is presented in Table 4.4, and accepts robust medium electrons with authors 1 or 3, within $|\eta| < 2.47$ (including the crack region) and fullfilling the isEM selection. All candidates from dead calorimetric regions are excluded using OTx maps.

From the Higgs Selection, see Table 4.7, the P_T requirement, the relative track based and calorimetric isolation, the charge and mass cuts are applied to the dielectron pair. A detailed study of the perfomance of the higgs cuts is presented in the following subsection.

The mass M_{12} distribution before the mass cut $|M_{12}| \leq 15GeV$ is presented in Figure 4.6 for Data and MC.

4.5.4 Additional muon selection

The remaining muons of the event, which are required to be in a well seperated from the ℓ_1, ℓ_2 and from each other, are required to pass the ID track requirements, presented in Table 4.3, and a series of other cuts. In details, the latter include:

- $P_T > 3GeV$
- *Combined or Segment Tagged*
- $Z_0(PV) \leq 10mm$
- $d_0(PV) \leq 1mm$
- *Opposite Sign (in case of dimuon)*

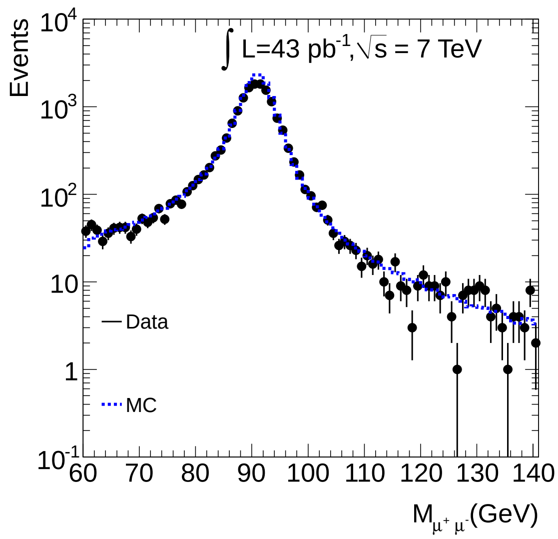

Figure 4.6: *Mass distribution of the leading dimuon pair ($\ell_1\ell_2$), the Z peak is apparent*
[]

Note that in the case where two additional muons are found, no explicit mass cut is applied to M_{34}, however the ΔR cut between leptons sets a threshold. This is done in order gain statistics and estimate the background in the control region.

Since only a few 4ℓ final state events were found in 2010 ATLAS data when the selection as described above was applied, the 3ℓ final state was studied as well in order to have statistics to study the proposed method. The main reason is a cross check of the MC expectations in the control region, since the available statistics does not allow an accurate measurement of the background contribution in the signal region.

4.6 Data Driven Estimation of $ZQQ \rightarrow Z\mu\mu$ Background

The muons sources accompanying the Z are from heavy flavor (Q) or from π/K decays. In this section, muons candidates originating from heavy flavor (Q) or from light jets (q) are treated seperately. Special emphasis is given to lepton candidates originating from Q, since $ZQQ \rightarrow 4\ell$ is the most important irreducible background to the $H \rightarrow 4\ell$.

The selection of the lepton candidates is described in Table 4.6 and in previous section 4.5.4. For the additional muons the P_T threshold applied is $3GeV$ in order to gain statistics, but cross–checks are made with 5 and $7GeV$ thresholds.

Muons from π/K decays were subtracted using a weighting procedure, which assigns to each charged track, selected by the same selection as the additional muons, a *probability to be reconstructed as a muon. The propability that a pion is reconstructed as a muon has been studied using reconstructed $K_s^0 \to \pi^+\pi^-$ decays and the total probability estimated to be 0.1% [13]. From that study, a 20% systematic uncertainty is assigned.*

The estimated rates of muons from heavy flavor decays per Z decay with the weighting procedure applied on MC are presented in Table 4.8, for both decay channels $Z \to \mu^+\mu^-$ and $Z \to e^+e^-$, along with the corresponding truth rates. The estimated and truth values (from MC) are in very good agreement and as a result the method can be applied on Data.

P_T cut (GeV)	$Z(Q \to \mu)/Z$ decay (%)		$Z(QQ \to \mu^+\mu^-)/Z$ decay (%)	
	Estimated	True	Estimated	True
3	0.538	0.535 ± 0.004	0.0114	0.0110 ± 0.0006
5	0.269	0.273 ± 0.003	0.0036	0.0033 ± 0.0004
7	0.163	0.163 ± 0.003	0.0013	0.0013 ± 0.0003

Table 4.8: *Estimated and true events of $Q \to \mu$ and $QQ \to \mu^+\mu^-$, expressed in percentage of Z for MC, for different P_T thersholds of the additional muons*

Apart from the fake muons, the $Z + \mu\mu$ final state receive contributions from ZZ and $t\bar{t}$. In contrast, in the 3ℓ final state these contributions are estimated from MC to be negligible (< 2% and P_T independent). The detailed amount of their contribution to the 3ℓ and 4ℓ final states as well as the $Z + jets$ contribution estimated from MC and given in Table 4.9.

Sample	$Z + \mu(pb)$	$Z + \mu^+\mu^-(pb)$
$3GeV$		
$Z + jets$	6.17	0.130
$t\bar{t}$	0.097	0.026
ZZ	0.003	0.005
$7GeV$		
Sample	$Z + \mu$ (pb)	$Z + \mu^+\mu^-(pb)$
$Z + jets$	1.44	0.012
$t\bar{t}$	0.017	0.001
ZZ	0.012	0.005

Table 4.9: *Estimated cross sections of the contribution to the final state of the $Z + jets$, ZZ and $t\bar{t}$ background, for different P_T thresholds applied.*

For the 4ℓ final state, the ZZ background contribution is estimated to be 30%

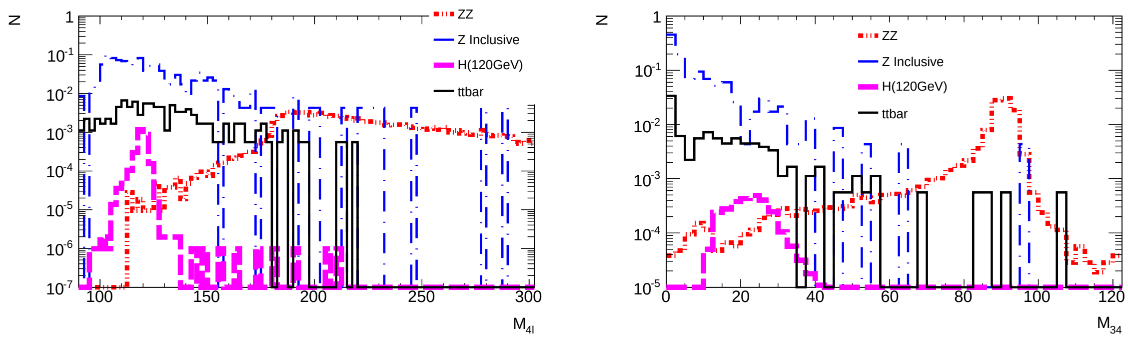

(a) (b)

Figure 4.7: *Mass distributions of the quadraplets of the* 4ℓ *final state 4.7(a) and the non-leading dimuon pair 4.7(b) for* $t\bar{t}$, ZZ, Z *Inclusive processes and Higgs (120GeV) as signal for the luminosity of our Data* ($40\ \mathrm{pb}^{-1}$).

[]

for a P_T *threshold of* $7GeV$ *applied to the additional muons. The* $t\bar{t}$ *background contributes more for low* P_T *thresholds. Figure 4.7 presents the mass distributions of the quadraplets of the* 4ℓ *final state for* $t\bar{t}$, ZZ, Z *Inclusive processes and Higgs (120GeV) for the signal, as well as the mass of the non-leading dilepton* (M_{34})*. The mass of the Higgs sample (120GeV) was choosen because of the lowest* M_{34} *mass that it gives. From the* M_{34} *plot it is apparent that if an upper cut, between* 60 *and* $70\,GeV$*, is set the* ZZ *contribution could almost be eliminated.*

4.7 Results of data to MC comparison

The selection, described previously for the leading dilepton 4.6 and the additional muons 4.5.4, is applied on both data and MC in this section. The properties of the additional muons are compared with the corresponding from the MC. The procedure to estimate the contribution of fake muons is applied on the data, while, due to low statistics, the ZZ *and* $t\bar{t}$ *contributions are taken from MC.*

When a Z *candidate is found, the tracks are rewighted using the same probability map as that of the MC and the* π/K *contamination is estimated. Figure 4.8 shows the additional muon multiplicity in proportion of the* Z *decays, before and after the subtraction of the* π/K *contamination. In Table 4.10 the exact numbers of additional muons are reported, for both data and MC and for different* P_T *thresholds.*

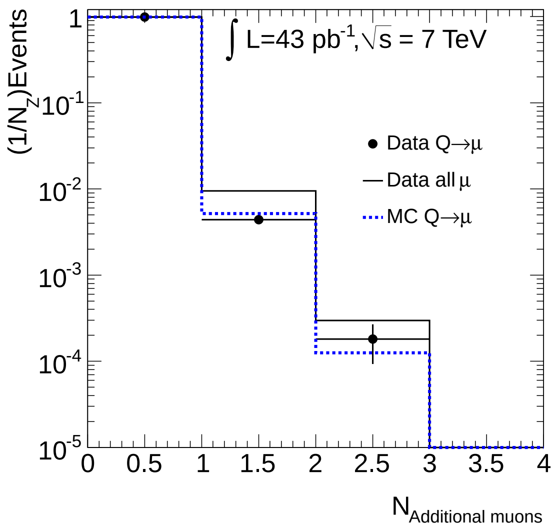

Figure 4.8: *Additional muon normalized multiplicity with a P_T threshold of $3GeV$, before and after the subtraction of the π/K contamination. The MC expectations is also presented for heavy flavor.*

[]

4.7.1 $Z + \mu$

For the 3ℓ final state the agreement between data and simulation is investigated. Figure 4.8 presents the normalized per number of Z events found, while Figure 4.9 presents the normalised P_T spectrum for both data and MC.

When the isolation and impact parameter criteria are imposed on the additional muons the efficiency recorded in data is $(27 \pm 3)\%$, which is in agreement with the 25% efficiency measured from the MC. The distribution of these properties, before this additional selection, are presented in Figure 4.10. For the case of the calorimetric isolation, the first bin shows discrepancies between data and MC. The pile–up is not the cause, since the MC describes the pile–up conditions of our data. The rest of the distribution though, as well as the other distributions are in agreement.

Additional Tracks Selection

Same selection criteria as for the additional muons are applied to tracks, excluding those tracks which are associated to the Z boson leptons. The purpose is to be used for the measurement of $P(\pi/K \rightarrow \mu)$ rates. In this way, each event in the $Z+tracks$ final state can be assigned with a probability to contribute to the $Z + \mu$ or $Z + \mu^+\mu^-$ final state, yielding the predicted contaminating contribution $N_{Z+(q\rightarrow\mu)}$. The number of observed $Z + \mu(\mu)$ events after the subtraction of the contaminating $N_{Z+(q\rightarrow\mu)}$ contribution can

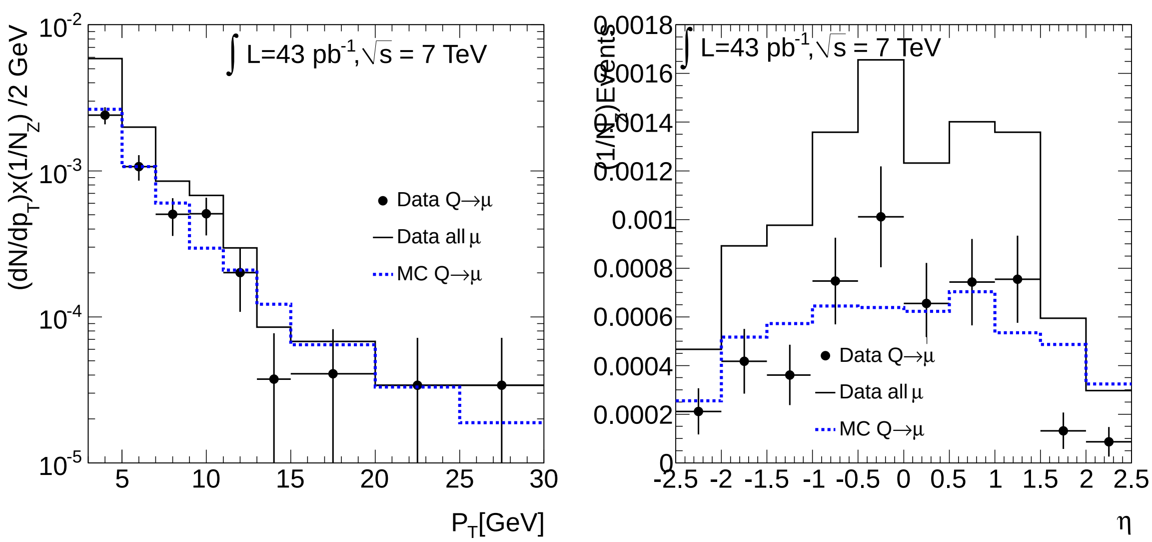

(a) (b)

Figure 4.9: *4.9(a) Additional muon normalized P_T spectrum and 4.9(b) η distribution with $P_T > 3GeV$ threshold, before and after the subtraction of the π/K contamination. The MC expectations is also presented for heavy flavor.*

[]

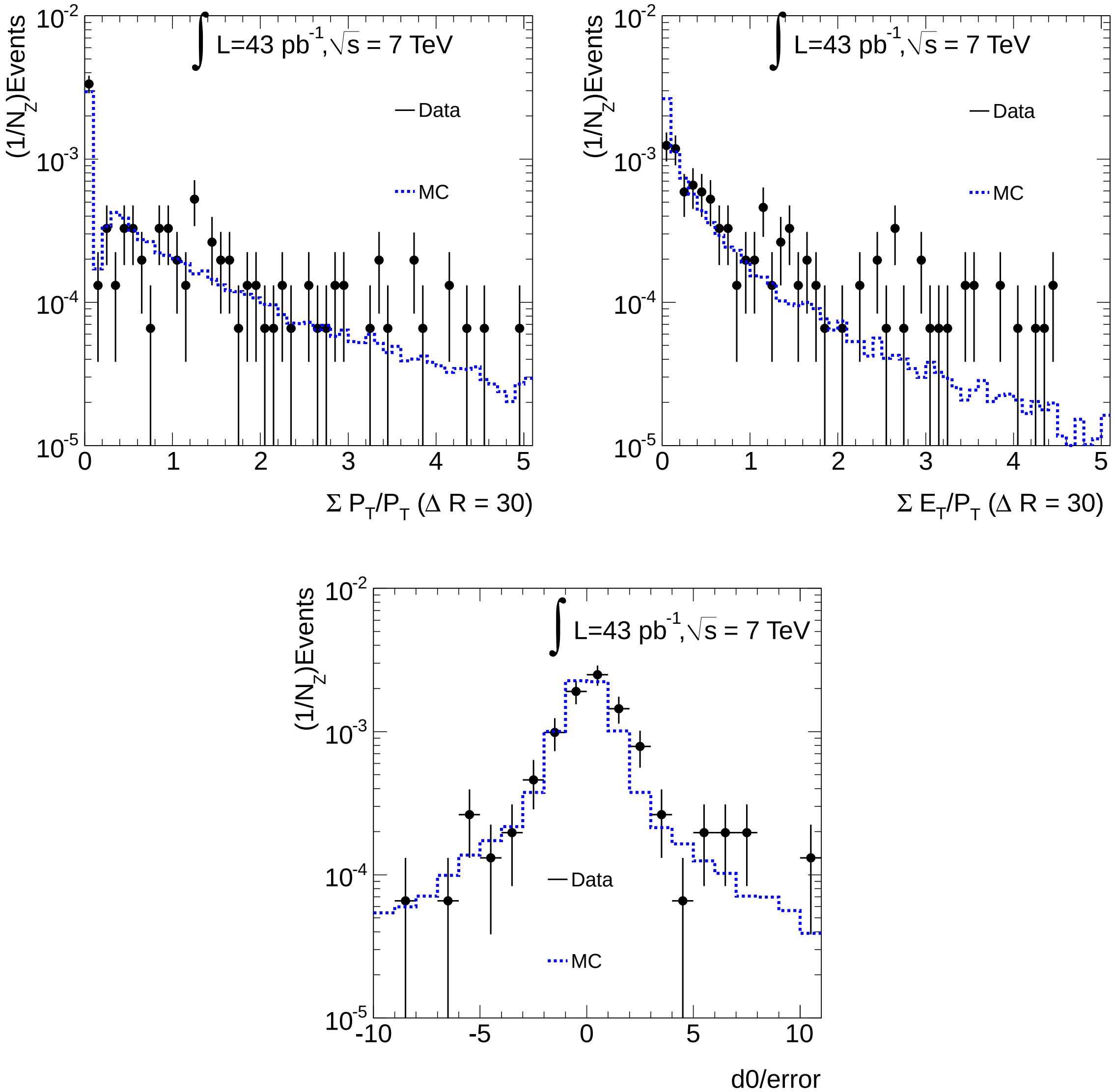

Figure 4.10: *Track based and calorimetric isolation and d_0 significance of extra muons normalized to P_T.*

[]

			Final State 3ℓ	
		Events	$Z+\mu/Z \times 10^{-2}$	$Z+(Q\rightarrow\mu)/Z \times 10^{-2}$
$p_T > 3$ GeV	Data	241	(1.02 ± 0.07)	0.51 ± 0.08
	MC		0.99	0.54 ± 0.05
$p_T > 5$ GeV	Data	103	(0.43 ± 0.04)	0.27 ± 0.05
	MC		0.42	0.27 ± 0.02
$p_T > 7$ GeV	Data	51	(0.22 ± 0.03)	0.15 ± 0.03
	MC		0.23	0.16 ± 0.01
			Final State 4ℓ	
		Events	$Z+\mu\mu/Z \times 10^{-3}$	$Z+(QQ\rightarrow\mu\mu)/Z \times 10^{-3}$
$p_T > 3$ GeV	Data	7	(0.30 ± 0.11)	0.20 ± 0.11
	MC		0.232	0.114 ± 0.012
$p_T > 5$ GeV	Data	1	(0.04 ± 0.04)	0.03 ± 0.03
	MC		0.060	0.036 ± 0.005
$p_T > 7$ GeV	Data	1	(0.04 ± 0.04)	0.03 ± 0.04
	MC		0.027	0.013 ± 0.002

Table 4.10: Number of events $Z+\mu$ and $Z+\mu^+\mu^-$ in data and rates of events per Z decay of all additional muon events as well as the ones estimated to originate from heavy quark decays in data and MC.

then be compared with the Monte Carlo predictions for each of the $Z+\mu$ or $Z+\mu^+\mu^-$ processes, as presented in previous section. The properties of the tracks are presented in Figures 4.11. The track multiplicity 4.11(a) seems to be harder in data for higher P_T values than expected from MC. Pile-up simulated samples were used for further investigation, however no evidence was found that the pile-up is the cause. P_T and η distributions shapes though agree for data and MC.

4.7.2 $Z+\mu^+\mu^-$

The statistics of 4ℓ final states found is extremely limited, as presented in Table 4.10. With a $3GeV$ cut seven cases with second dilepton are found, from which in only four the additional dimuon is opposite sign. The mass distribution of the quadraplets with opposite sign dileptons is presented in Figure 4.12 and it is in agreement with the MC expectations.

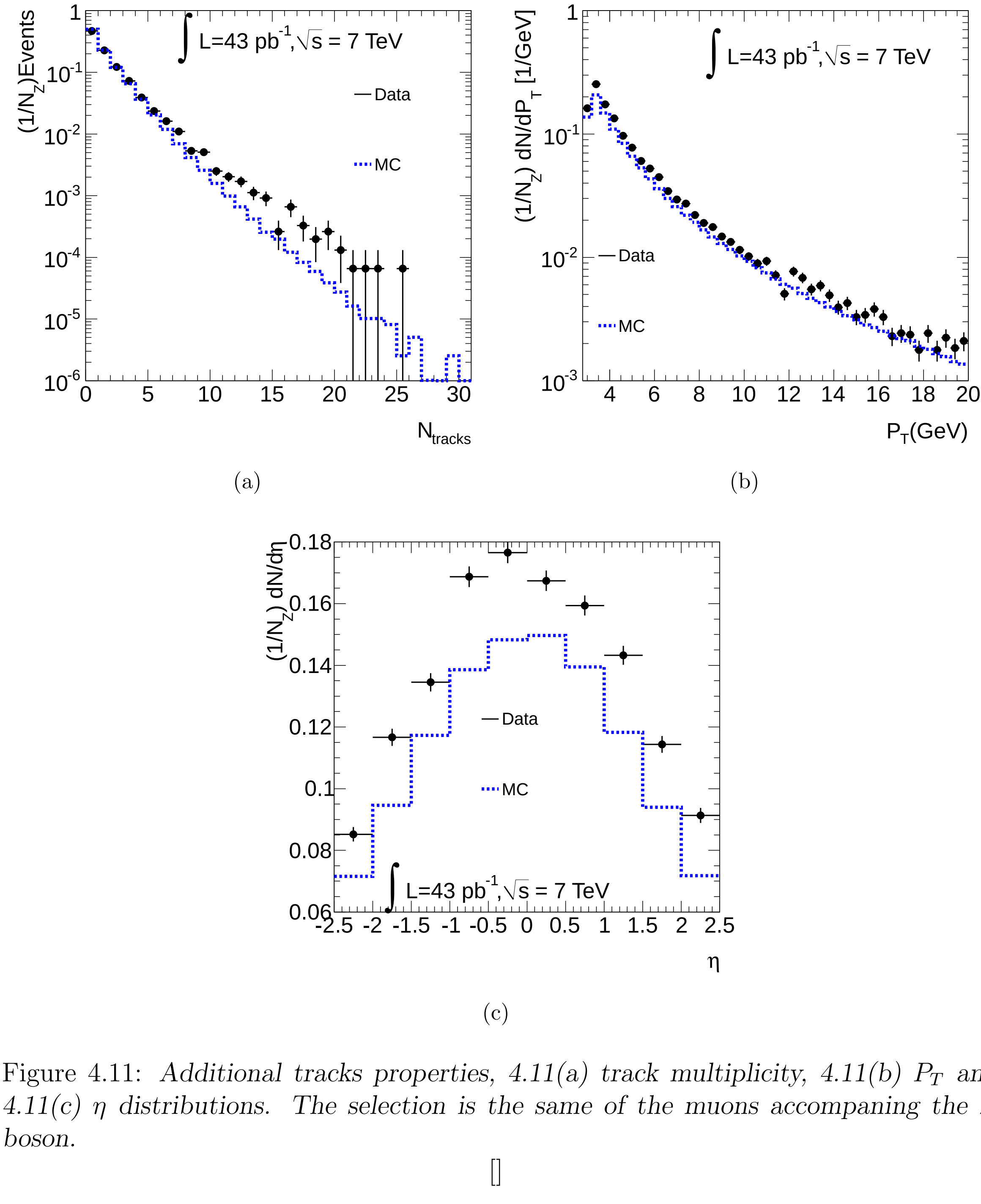

Figure 4.11: *Additional tracks properties, 4.11(a) track multiplicity, 4.11(b) P_T and 4.11(c) η distributions. The selection is the same of the muons accompaning the Z boson.*

[]

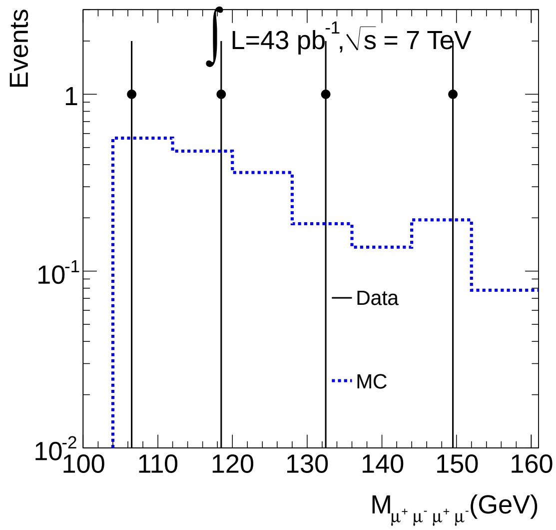

Figure 4.12: *Mass distribution of four lepton events, where the non-leading dimuon is opposite sign and the* P_T *cut is* $3GeV$.

[]

4.8 Data Driven Efficiency Estimation of the Isolation and Impact Parameter Requirements (by using Z–decays)

Apart from the data driven estimation of the ZQQ *background, the data driven signal efficiency of the additional muon selection is of interest. This section presents a data based study of the lepton selection criteria, these criteria are the impact parameter significance, calorimetric and track based isolation. For the signal, the efficiency is evaluated for* Z *decay events for different* P_T *bins since low* P_T *muons can be isolated. A method similar to the "tag and probe", is used to measure the efficency of this selection. Events with at least one dimuon pair, are required to have at least one muon passing all the cuts of Table 4.3, this is defined as the tag muon. The additional selection is applied to an opposite sign muon (probe) simultaneously or individually each cut. In order to avoid biases in the estimation, the procedure is applied separately in positive and negative charged tag muons. After the selection, the surviving number of candidates is estimated with a fit on the dimuon invariant mass. A convolution of a Breit-Wigner with a Crystal-Ball function is used for the signal and an exponential is used for the background. Examples of the fitting are shown in Figure 4.13. Two cases are presented, the upper row corresponds to the most difficult case* $(10 < P_T^{probe} < 20GeV)$ *where significant background exists, especially in the case where no additional* *criteria are imposed to the probe muon, and the lower row corresponds to the case* $40 < P_T^{probe} < 50GeV$*, where the background is negligible.*

The results of the application of the procedure for all the P_T *intervals and selections are shown in Figure 4.14. The uncertainty is estimated by the quadratic difference of the fit result uncertainties on the number of signal events. The uncertainty assigned by this method is in general higher than the difference in the estimates produced by different signal and background fitting functions and is therefore assumed to be the systematic uncertainty of the procedure. At high* P_T *values, where the QCD background is negligible, it reaches asymptotically the expected binomial estimate. The ratio between Data and MC efficiencies, is shown in Figure 4.15.*

The efficiency of the additional selection criteria is shown to be in very good agreement between Data and MC for all P_T *intervals and no scale factor is needed to be applied to the MC expectation. The overall efficiencies in data and MC, as well as their ratio, are summarized in Table 4.11. The errors are due to systematic effects stemming from the fit procedure on the data samples.*

Selection	Efficiency (Data)	Efficiency (MC)	Ratio
$d_0/\sigma_{d_0} < 3.5$	0.995	0.996	1.000 ± 0.001
Calo Iso/$P_T < 0.3$	0.995	0.995	1.000 ± 0.001
Track Iso/$P_T < 0.2$	0.989	0.992	0.997 ± 0.002
All cuts	0.982	0.985	0.997 ± 0.002

Table 4.11: *Efficiency in Data and MC for each selection requirement and their combination.*

.

4.9 Conclusions

A search for event with 3ℓ *and* 4ℓ *final states has been perfomed using the* $43pb^{-}1$ *of* pp *collisions at* $\sqrt{s} = 7TeV$ *of the ATLAS Experiment. The event studied demonstrated good agreement of the simulation with the observation. The effect of the muon isolation and the impact parameter criterias were studied and proved to be no discrepancy between data and simulation. The extraction of the* $Z + (Q \rightarrow \mu)$ *control samples with muons originating from the heavy quark decays allowed a quantitative comparison, since* $Z + (QQ \rightarrow \mu^+\mu^-)$ *is limited by the large statistical uncertainties. No evidence supports any disagreement between data and MC.*

This analysis was perfomed for contributing to the $H \rightarrow 4\ell$ *(approved) conference note, "Search for the Standard Model Higgs boson in the decay channel* $H \rightarrow ZZ^{(*)} \rightarrow 4\ell$ *with* $40pb^{-}1$ *of* pp *collisions at* $\sqrt{s} = 7TeV$*", ATLAS-COM-CONF-2011-047.*

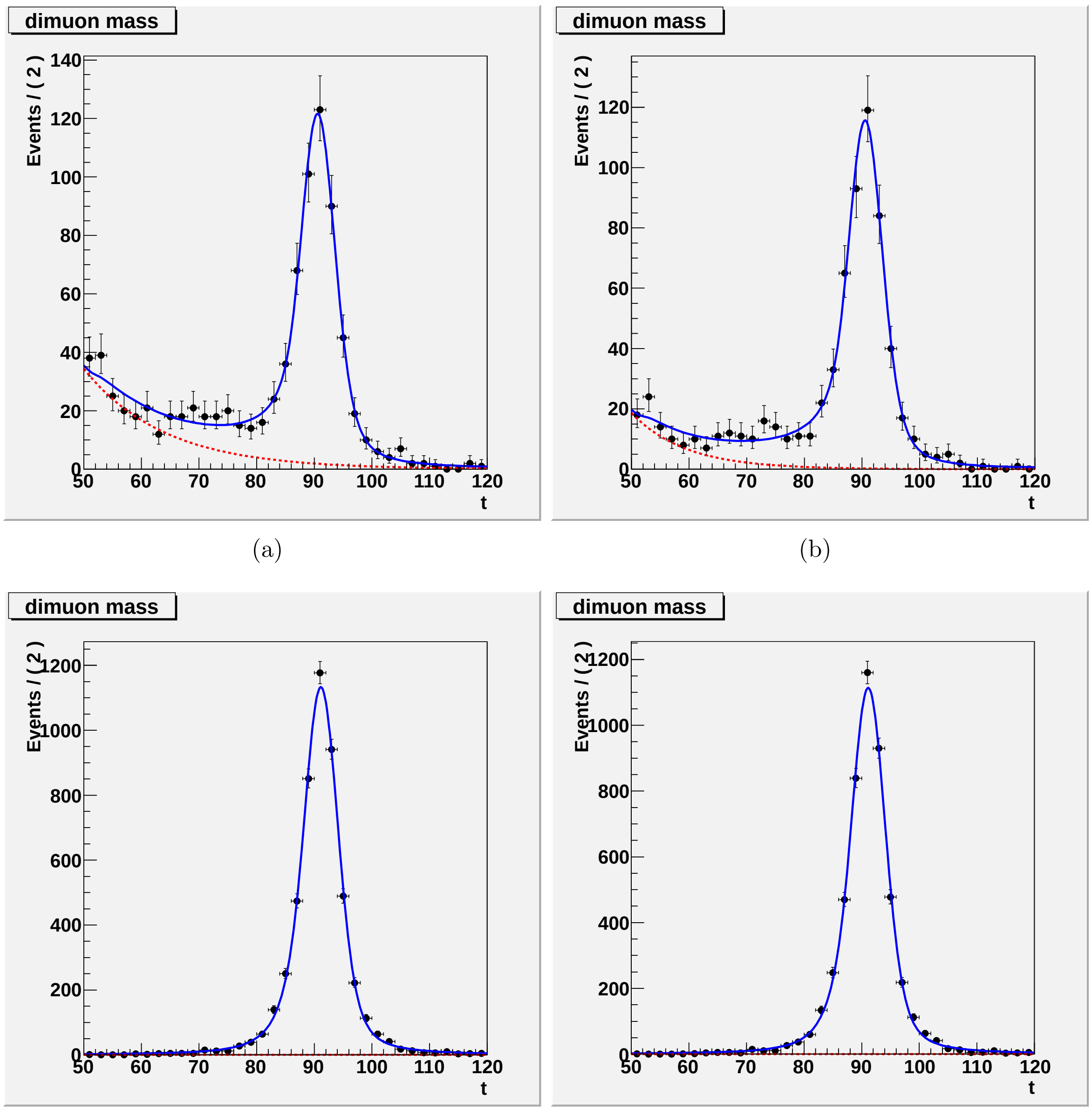

(a) (b)

(c) (d)

Figure 4.13: *4.13(a): Dimuon mass distributions for* $10 < P_T^{probe} < 20$ *GeV in data without additional requirements on probe muons. 4.13(b): all the requirements imposed. 4.13(c) and 4.13(d): Are the corresponding distributions for probe muons with* $40 < P_T^{probe} < 50$ *GeV. The vertical axis corresponds to the number of events whereas the horizontal to masses (GeV)*

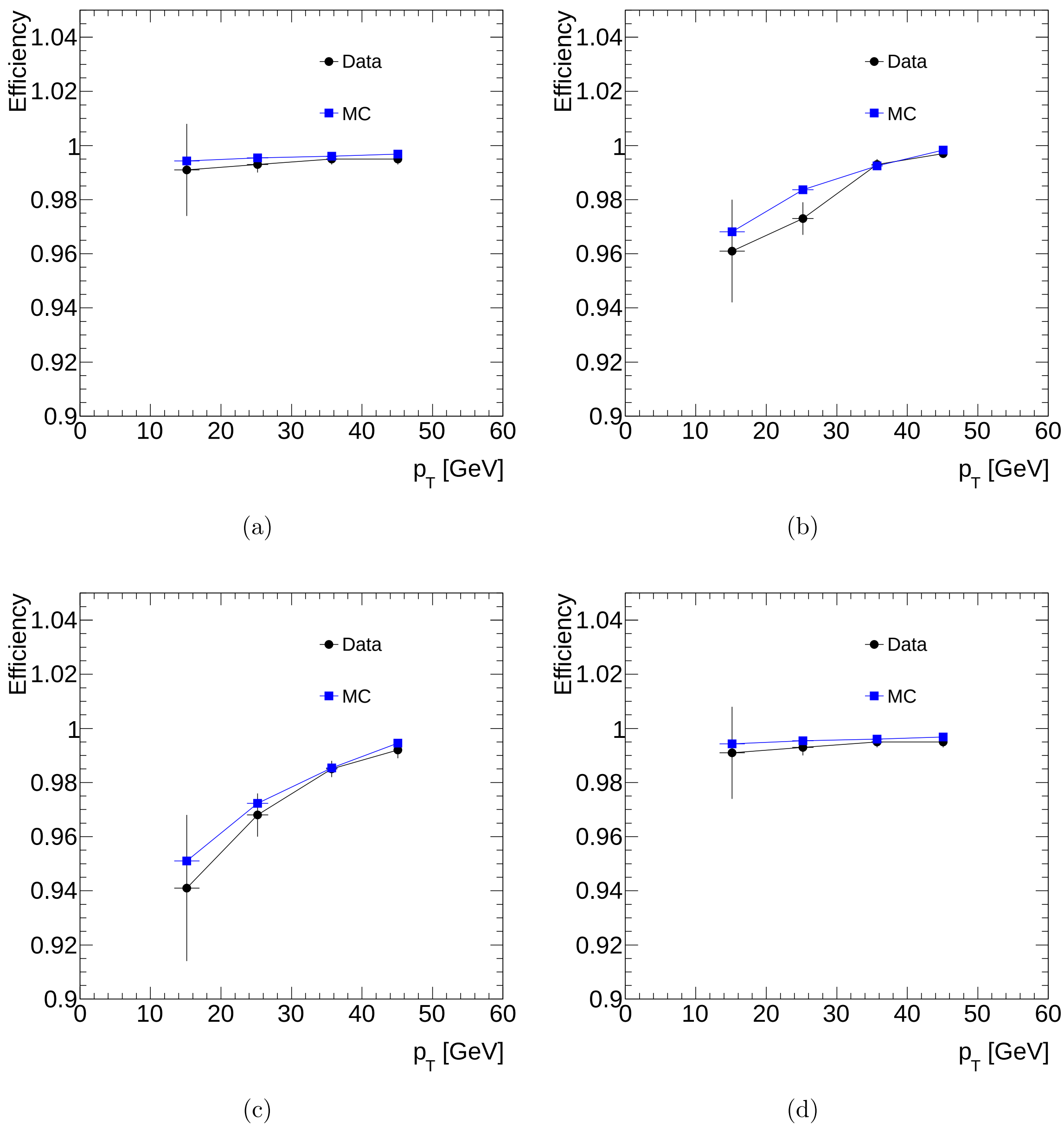

Figure 4.14: Probe muon efficiencies as function of the transverse momentum for both data and simulation, imposing calorimeter isolation (a), track isolation (b), impact parameter significance (c) and both isolation criteria simultaneously (d).

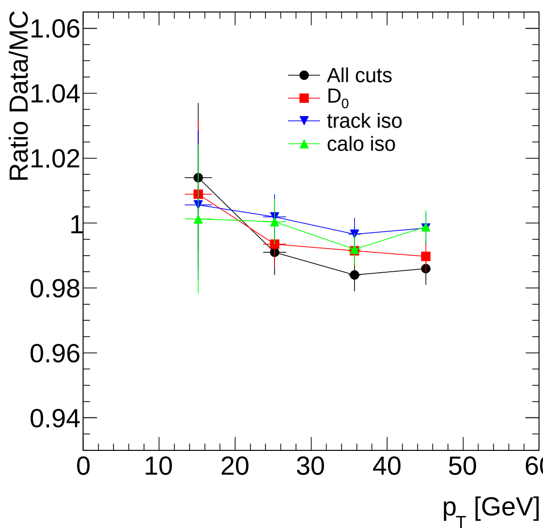

Figure 4.15: *The ratio between Data and MC for the efficiency of the additional selection criteria on muons as a function of* P_T

.

Bibliography

[1] *T. Sjostrand, S. Mrenna and P. Z. Skands, "PYTHIA 6.4 Physics and Manual", JHEP 0605 (2006) 026, AriXiv: hep-ph/0603175*

[2] *T. Gleisberg, S. Hoeche, F. Krauss, M. Schoenherr, S. Schumann, F. Siegert, J. Winter, "Event Generation with SHERPA 1.1", arXiv:hep-ph/0811.4622*

[3] *S. Frixione and B. R. Webber, "The MC@NLO Event Generator", arXiv:hep-ph/0207182*

[4] *M. L. Mangano, M. Moretti, F. Piccinini, R. Pittau, and A. D. Polosa, "ALPGEN, a Generator for Hard Multiparton Processes in Hadronic Collisions", JHEP 07 (2003) 001,arXiv:hep-ph/0206293*

[5] *ATLAS Collaboration, "Search for the Standard Model Higgs boson in the decay channel* $H \rightarrow ZZ^{(*)} \rightarrow 4\ell$ *with* $40pb^{-}1$ *of pp collisions at* $\sqrt{s} = 7TeV$*", ATLAS-COM-CONF-2011-047*

[6] *N. Berger, T. Bold, T. Eifert, G. Fischer, S. George, J. Haller, A. Hoecker, J. Masik, M. zur Nedden, V. Perez Reale, C. Risler, C. Schiavi, J. Stelzer, X. Wu, "The High-Level-Trigger Steering of the ATLAS experiment", ATL-COM-DAQ-2007-020*

[7] *ATLAS Collaboration, "Muons in the ATLAS Calorimeters: Energy Loss Corrections and Muon Tagging", CSC note*

[8] *ATLAS Collaboration, 'Expected Performance of the ATLAS Experiment : Detector, Trigger and Physics",Geneva : CERN, 2009, arXiv:0901.0512*

[9] *ATLAS Collaboration, 'Expected Electron Performance in the ATLAS experiment', ATL-PHYS-PUB-2011-006*

[10] *E. Jensen, "Dilepton final states with ATLAS at* $\sqrt{s} = 7TeV$*", CERN - Master Thesis - 2011-004*

[11] *ATLAS Collaboration, "Muon reconstruction efficiency in reprocessed 2010 LHC proton-proton collision data recorded with the ATLAS detector", ATLAS-COM-CONF-2011-003*

[12] Andrew Hamilton on behalf of the ATLAS Collaboration, 'The ATLAS Trigger System Commissioning and Performance', arXiv:1010.0017

[13] ATLAS Collaboration, "Muon Reconstruction Performance", ATLAS-CONF-2010-064

[14] Stefano Rosati for the ATLAS collaboration, "Standard Model Higgs Boson Searches at ATLAS", 2008 J. Phys.: Conf. Ser. 110 042022

[15] Aharrouche M. ,Anastopoulos C. ,Dao V., Derue F., Dudziak F., Fedin O., Fournier D., Froidevaux D., Hartert J., Iconomidou-Fayard L., Kerschen K., Koenig S., Koffas T., Maleev V., Paganis E., Pasztor G., Poveda J., Robichaud-Veronneau A., Schaffer A., Sarangi T., Sedykh E., Solovyev V., Tackmann K., Theveneaux-Pelzer T., Urquijo P., Wielers M., Wu, S L, "Expected electron performance in the ATLAS experiment", CERN,ATL-PHYS-INT-2010-126, Nov 2010

[16] ATLAS Collaboration, 'Muon Reconstruction Efficiency in Reprocessed 2010 LHC proton-proton Collision Data Recorded with the ATLAS Detector', ATLAS-CONF-2011-063

[17] Gustavo Ordonez Sanz, "Muon Identification in the ATLAS Calorimeters", Thesis Radboud Universiteit Nijmegen, 2009

[18] ATLAS tool for luminosity calculation

Appendices

Appendix A

MC Samples list

The MC samples used for the present analysis are:

```
mc10_7TeV.109065.PythiaH140zz4l - e540_s765_s767 - r1302
mc10_7TeV.109291.Pythiazz4l - e530_s765_s767 - r1302,r1430
mc10_7TeV.107660.AlpgenJimmyZmumuNp0_pt20 - e529_s765_s767 - r1302,r1430
mc10_7TeV.107661.AlpgenJimmyZmumuNp1_pt20 - e529_s765_s767 - r1302,r1430
mc10_7TeV.107662.AlpgenJimmyZmumuNp2_pt20 - e529_s765_s767 - r1302,r1430
mc10_7TeV.107663.AlpgenJimmyZmumuNp3_pt20 - e529_s765_s767 - r1302,r1430
mc10_7TeV.107664.AlpgenJimmyZmumuNp4_pt20 - e529_s765_s767 - r1302,r1430
mc10_7TeV.107665.AlpgenJimmyZmumuNp5_pt20 - e529_s765_s767 - r1302,r1430
mc10_7TeV.106088.McAtNloZmumu_no_filter - e521_s765_s767 - r1302
mc10_7TeV.104994.Sherpa010103Z4jetstomumu - e550_s765_s767 - r1302
mc10_7TeV.109345.T1_McAtNlo_Jimmy_2LeptonsMll60GeV - e583_s765_s767 - r1302
mc10_7TeV.106047.PythiaZmumu_no_filter - e468_s765_s767 - r1302,r1430
mc10_7TeV.106046.PythiaZee_no_filter - e468_s765_s767 - r1302,r1430
mc10_7TeV.109385.AlpgenJimmyZmumubbNp0_3Leptons- e579_s765_s767 - r1302,r1430
mc10_7TeV.109386.AlpgenJimmyZmumubbNp1_3Leptons- e579_s765_s767 - r1302,r1430
mc10_7TeV.109387.AlpgenJimmyZmumubbNp2_3Leptons- e579_s765_s767 - r1302,r1430
mc10_7TeV.109388.AlpgenJimmyZmumubbNp3_3Leptons- e579_s765_s767 - r1302,r1430
```

Appendix B

Analytical Tables of the Standart Model Higgs Branching Ratios

Table B.1: SM Higgs branching ratios in fermionic final states in the low- and intermediate-mass range.

M_H [GeV]	$H \to bb$	$H \to \tau\tau$	$H \to \mu\mu$	$H \to g\bar{g}$	$H \to c\bar{c}$	$H \to t\bar{t}$
90	$8.12 \cdot 10^{-1}$	$8.41 \cdot 10^{-2}$	$2.92 \cdot 10^{-4}$	$6.20 \cdot 10^{-4}$	$3.78 \cdot 10^{-2}$	0.00
95	$8.04 \cdot 10^{-1}$	$8.41 \cdot 10^{-2}$	$2.92 \cdot 10^{-4}$	$6.13 \cdot 10^{-4}$	$3.73 \cdot 10^{-2}$	0.00
100	$7.91 \cdot 10^{-1}$	$8.36 \cdot 10^{-2}$	$2.90 \cdot 10^{-4}$	$6.03 \cdot 10^{-4}$	$3.68 \cdot 10^{-2}$	0.00
105	$7.73 \cdot 10^{-1}$	$8.25 \cdot 10^{-2}$	$2.86 \cdot 10^{-4}$	$5.89 \cdot 10^{-4}$	$3.59 \cdot 10^{-2}$	0.00
110	$7.45 \cdot 10^{-1}$	$8.03 \cdot 10^{-2}$	$2.79 \cdot 10^{-4}$	$5.68 \cdot 10^{-4}$	$3.46 \cdot 10^{-2}$	0.00
115	$7.05 \cdot 10^{-1}$	$7.65 \cdot 10^{-2}$	$2.66 \cdot 10^{-4}$	$5.37 \cdot 10^{-4}$	$3.27 \cdot 10^{-2}$	0.00
120	$6.49 \cdot 10^{-1}$	$7.11 \cdot 10^{-2}$	$2.47 \cdot 10^{-4}$	$4.94 \cdot 10^{-4}$	$3.01 \cdot 10^{-2}$	0.00
125	$5.78 \cdot 10^{-1}$	$6.37 \cdot 10^{-2}$	$2.21 \cdot 10^{-4}$	$4.40 \cdot 10^{-4}$	$2.68 \cdot 10^{-2}$	0.00
130	$4.94 \cdot 10^{-1}$	$5.49 \cdot 10^{-2}$	$1.91 \cdot 10^{-4}$	$3.76 \cdot 10^{-4}$	$2.29 \cdot 10^{-2}$	0.00
135	$4.04 \cdot 10^{-1}$	$4.52 \cdot 10^{-2}$	$1.57 \cdot 10^{-4}$	$3.07 \cdot 10^{-4}$	$1.87 \cdot 10^{-2}$	0.00
140	$3.14 \cdot 10^{-1}$	$3.54 \cdot 10^{-2}$	$1.23 \cdot 10^{-4}$	$2.39 \cdot 10^{-4}$	$1.46 \cdot 10^{-2}$	0.00
145	$2.31 \cdot 10^{-1}$	$2.62 \cdot 10^{-2}$	$9.09 \cdot 10^{-5}$	$1.76 \cdot 10^{-4}$	$1.07 \cdot 10^{-2}$	0.00
150	$1.57 \cdot 10^{-1}$	$1.79 \cdot 10^{-2}$	$6.20 \cdot 10^{-5}$	$1.19 \cdot 10^{-4}$	$7.25 \cdot 10^{-3}$	0.00
155	$9.18 \cdot 10^{-2}$	$1.06 \cdot 10^{-2}$	$3.66 \cdot 10^{-5}$	$6.98 \cdot 10^{-5}$	$4.25 \cdot 10^{-3}$	0.00
160	$3.44 \cdot 10^{-2}$	$3.97 \cdot 10^{-3}$	$1.38 \cdot 10^{-5}$	$2.61 \cdot 10^{-5}$	$1.59 \cdot 10^{-3}$	0.00
165	$1.19 \cdot 10^{-2}$	$1.38 \cdot 10^{-3}$	$4.78 \cdot 10^{-6}$	$9.02 \cdot 10^{-6}$	$5.49 \cdot 10^{-4}$	0.00
170	$7.87 \cdot 10^{-3}$	$9.20 \cdot 10^{-4}$	$3.19 \cdot 10^{-6}$	$5.99 \cdot 10^{-6}$	$3.64 \cdot 10^{-4}$	0.00
175	$6.12 \cdot 10^{-3}$	$7.19 \cdot 10^{-4}$	$2.49 \cdot 10^{-6}$	$4.65 \cdot 10^{-6}$	$2.83 \cdot 10^{-4}$	0.00
180	$4.97 \cdot 10^{-3}$	$5.87 \cdot 10^{-4}$	$2.04 \cdot 10^{-6}$	$3.78 \cdot 10^{-6}$	$2.30 \cdot 10^{-4}$	0.00
185	$3.85 \cdot 10^{-3}$	$4.57 \cdot 10^{-4}$	$1.59 \cdot 10^{-6}$	$2.93 \cdot 10^{-6}$	$1.78 \cdot 10^{-4}$	0.00
190	$3.15 \cdot 10^{-3}$	$3.76 \cdot 10^{-4}$	$1.30 \cdot 10^{-6}$	$2.39 \cdot 10^{-6}$	$1.46 \cdot 10^{-4}$	0.00
195	$2.70 \cdot 10^{-3}$	$3.24 \cdot 10^{-4}$	$1.13 \cdot 10^{-6}$	$2.06 \cdot 10^{-6}$	$1.25 \cdot 10^{-4}$	0.00
200	$2.38 \cdot 10^{-3}$	$2.87 \cdot 10^{-4}$	$9.96 \cdot 10^{-7}$	$1.81 \cdot 10^{-6}$	$1.10 \cdot 10^{-4}$	0.00
210	$1.92 \cdot 10^{-3}$	$2.34 \cdot 10^{-4}$	$8.11 \cdot 10^{-7}$	$1.46 \cdot 10^{-6}$	$8.89 \cdot 10^{-5}$	0.00
220	$1.60 \cdot 10^{-3}$	$1.96 \cdot 10^{-4}$	$6.81 \cdot 10^{-7}$	$1.22 \cdot 10^{-6}$	$7.40 \cdot 10^{-5}$	0.00
230	$1.36 \cdot 10^{-3}$	$1.68 \cdot 10^{-4}$	$5.82 \cdot 10^{-7}$	$1.03 \cdot 10^{-6}$	$6.27 \cdot 10^{-5}$	0.00
240	$1.17 \cdot 10^{-3}$	$1.45 \cdot 10^{-4}$	$5.04 \cdot 10^{-7}$	$8.86 \cdot 10^{-7}$	$5.39 \cdot 10^{-5}$	0.00
250	$1.01 \cdot 10^{-3}$	$1.27 \cdot 10^{-4}$	$4.42 \cdot 10^{-7}$	$7.70 \cdot 10^{-7}$	$4.68 \cdot 10^{-5}$	0.00
260	$8.89 \cdot 10^{-4}$	$1.12 \cdot 10^{-4}$	$3.90 \cdot 10^{-7}$	$6.75 \cdot 10^{-7}$	$4.11 \cdot 10^{-5}$	$5.14 \cdot 10^{-8}$
270	$7.86 \cdot 10^{-4}$	$1.00 \cdot 10^{-4}$	$3.47 \cdot 10^{-7}$	$5.97 \cdot 10^{-7}$	$3.63 \cdot 10^{-5}$	$2.29 \cdot 10^{-6}$
280	$7.00 \cdot 10^{-4}$	$8.98 \cdot 10^{-5}$	$3.11 \cdot 10^{-7}$	$5.31 \cdot 10^{-7}$	$3.23 \cdot 10^{-5}$	$1.09 \cdot 10^{-5}$
290	$6.27 \cdot 10^{-4}$	$8.09 \cdot 10^{-5}$	$2.80 \cdot 10^{-7}$	$4.76 \cdot 10^{-7}$	$2.90 \cdot 10^{-5}$	$3.06 \cdot 10^{-5}$
300	$5.65 \cdot 10^{-4}$	$7.33 \cdot 10^{-5}$	$2.54 \cdot 10^{-7}$	$4.29 \cdot 10^{-7}$	$2.61 \cdot 10^{-5}$	$6.87 \cdot 10^{-5}$
310	$5.12 \cdot 10^{-4}$	$6.68 \cdot 10^{-5}$	$2.32 \cdot 10^{-7}$	$3.89 \cdot 10^{-7}$	$2.36 \cdot 10^{-5}$	$1.38 \cdot 10^{-4}$
320	$4.66 \cdot 10^{-4}$	$6.12 \cdot 10^{-5}$	$2.12 \cdot 10^{-7}$	$3.54 \cdot 10^{-7}$	$2.15 \cdot 10^{-5}$	$2.66 \cdot 10^{-4}$
330	$4.26 \cdot 10^{-4}$	$5.63 \cdot 10^{-5}$	$1.95 \cdot 10^{-7}$	$3.24 \cdot 10^{-7}$	$1.97 \cdot 10^{-5}$	$5.21 \cdot 10^{-4}$
340	$3.92 \cdot 10^{-4}$	$5.20 \cdot 10^{-5}$	$1.80 \cdot 10^{-7}$	$2.98 \cdot 10^{-7}$	$1.81 \cdot 10^{-5}$	$1.20 \cdot 10^{-3}$
350	$3.57 \cdot 10^{-4}$	$4.76 \cdot 10^{-5}$	$1.65 \cdot 10^{-7}$	$2.71 \cdot 10^{-7}$	$1.65 \cdot 10^{-5}$	$1.56 \cdot 10^{-2}$
360	$3.16 \cdot 10^{-4}$	$4.23 \cdot 10^{-5}$	$1.47 \cdot 10^{-7}$	$2.40 \cdot 10^{-7}$	$1.46 \cdot 10^{-5}$	$5.15 \cdot 10^{-2}$
370	$2.81 \cdot 10^{-4}$	$3.78 \cdot 10^{-5}$	$1.31 \cdot 10^{-7}$	$2.13 \cdot 10^{-7}$	$1.29 \cdot 10^{-5}$	$8.37 \cdot 10^{-2}$
380	$2.52 \cdot 10^{-4}$	$3.40 \cdot 10^{-5}$	$1.18 \cdot 10^{-7}$	$1.91 \cdot 10^{-7}$	$1.16 \cdot 10^{-5}$	$1.10 \cdot 10^{-1}$
390	$2.28 \cdot 10^{-4}$	$3.10 \cdot 10^{-5}$	$1.07 \cdot 10^{-7}$	$1.73 \cdot 10^{-7}$	$1.05 \cdot 10^{-5}$	$1.32 \cdot 10^{-1}$
400	$2.08 \cdot 10^{-4}$	$2.84 \cdot 10^{-5}$	$9.83 \cdot 10^{-8}$	$1.58 \cdot 10^{-7}$	$9.59 \cdot 10^{-6}$	$1.48 \cdot 10^{-1}$
410	$1.91 \cdot 10^{-4}$	$2.61 \cdot 10^{-5}$	$9.06 \cdot 10^{-8}$	$1.45 \cdot 10^{-7}$	$8.80 \cdot 10^{-6}$	$1.62 \cdot 10^{-1}$
420	$1.76 \cdot 10^{-4}$	$2.43 \cdot 10^{-5}$	$8.41 \cdot 10^{-8}$	$1.34 \cdot 10^{-7}$	$8.13 \cdot 10^{-6}$	$1.72 \cdot 10^{-1}$
430	$1.64 \cdot 10^{-4}$	$2.26 \cdot 10^{-5}$	$7.84 \cdot 10^{-8}$	$1.24 \cdot 10^{-7}$	$7.55 \cdot 10^{-6}$	$1.79 \cdot 10^{-1}$
440	$1.53 \cdot 10^{-4}$	$2.12 \cdot 10^{-5}$	$7.34 \cdot 10^{-8}$	$1.16 \cdot 10^{-7}$	$7.05 \cdot 10^{-6}$	$1.85 \cdot 10^{-1}$
450	$1.43 \cdot 10^{-4}$	$1.99 \cdot 10^{-5}$	$6.90 \cdot 10^{-8}$	$1.09 \cdot 10^{-7}$	$6.60 \cdot 10^{-6}$	$1.89 \cdot 10^{-1}$
460	$1.35 \cdot 10^{-4}$	$1.88 \cdot 10^{-5}$	$6.51 \cdot 10^{-8}$	$1.02 \cdot 10^{-7}$	$6.21 \cdot 10^{-6}$	$1.91 \cdot 10^{-1}$
470	$1.27 \cdot 10^{-4}$	$1.78 \cdot 10^{-5}$	$6.16 \cdot 10^{-8}$	$9.63 \cdot 10^{-8}$	$5.85 \cdot 10^{-6}$	$1.93 \cdot 10^{-1}$
480	$1.20 \cdot 10^{-4}$	$1.69 \cdot 10^{-5}$	$5.85 \cdot 10^{-8}$	$9.10 \cdot 10^{-8}$	$5.53 \cdot 10^{-6}$	$1.94 \cdot 10^{-1}$
490	$1.14 \cdot 10^{-4}$	$1.60 \cdot 10^{-5}$	$5.56 \cdot 10^{-8}$	$8.63 \cdot 10^{-8}$	$5.24 \cdot 10^{-6}$	$1.94 \cdot 10^{-1}$

Table B.2: SM Higgs branching ratios in fermionic final states in the high-mass range.

M_H [GeV]	$H \to bb$	$H \to \tau\tau$	$H \to \mu\mu$	$H \to g\bar{g}$	$H \to c\bar{c}$	$H \to t\bar{t}$
500	$1.08 \cdot 10^{-4}$	$1.53 \cdot 10^{-5}$	$5.30 \cdot 10^{-8}$	$8.19 \cdot 10^{-8}$	$4.98 \cdot 10^{-6}$	$1.93 \cdot 10^{-1}$
510	$1.03 \cdot 10^{-4}$	$1.46 \cdot 10^{-5}$	$5.06 \cdot 10^{-8}$	$7.80 \cdot 10^{-8}$	$4.74 \cdot 10^{-6}$	$1.92 \cdot 10^{-1}$
520	$9.80 \cdot 10^{-5}$	$1.40 \cdot 10^{-5}$	$4.84 \cdot 10^{-8}$	$7.44 \cdot 10^{-8}$	$4.52 \cdot 10^{-6}$	$1.90 \cdot 10^{-1}$
530	$9.36 \cdot 10^{-5}$	$1.34 \cdot 10^{-5}$	$4.64 \cdot 10^{-8}$	$7.10 \cdot 10^{-8}$	$4.31 \cdot 10^{-6}$	$1.88 \cdot 10^{-1}$
540	$8.95 \cdot 10^{-5}$	$1.28 \cdot 10^{-5}$	$4.45 \cdot 10^{-8}$	$6.79 \cdot 10^{-8}$	$4.12 \cdot 10^{-6}$	$1.86 \cdot 10^{-1}$
550	$8.57 \cdot 10^{-5}$	$1.23 \cdot 10^{-5}$	$4.27 \cdot 10^{-8}$	$6.50 \cdot 10^{-8}$	$3.95 \cdot 10^{-6}$	$1.84 \cdot 10^{-1}$
560	$8.21 \cdot 10^{-5}$	$1.18 \cdot 10^{-5}$	$4.10 \cdot 10^{-8}$	$6.23 \cdot 10^{-8}$	$3.79 \cdot 10^{-6}$	$1.81 \cdot 10^{-1}$
570	$7.88 \cdot 10^{-5}$	$1.14 \cdot 10^{-5}$	$3.95 \cdot 10^{-8}$	$5.98 \cdot 10^{-8}$	$3.63 \cdot 10^{-6}$	$1.78 \cdot 10^{-1}$
580	$7.57 \cdot 10^{-5}$	$1.10 \cdot 10^{-5}$	$3.80 \cdot 10^{-8}$	$5.74 \cdot 10^{-8}$	$3.49 \cdot 10^{-6}$	$1.75 \cdot 10^{-1}$
590	$7.28 \cdot 10^{-5}$	$1.06 \cdot 10^{-5}$	$3.67 \cdot 10^{-8}$	$5.52 \cdot 10^{-8}$	$3.35 \cdot 10^{-6}$	$1.72 \cdot 10^{-1}$
600	$7.00 \cdot 10^{-5}$	$1.02 \cdot 10^{-5}$	$3.54 \cdot 10^{-8}$	$5.31 \cdot 10^{-8}$	$3.23 \cdot 10^{-6}$	$1.69 \cdot 10^{-1}$
610	$6.74 \cdot 10^{-5}$	$9.86 \cdot 10^{-6}$	$3.42 \cdot 10^{-8}$	$5.12 \cdot 10^{-8}$	$3.11 \cdot 10^{-6}$	$1.66 \cdot 10^{-1}$
620	$6.50 \cdot 10^{-5}$	$9.53 \cdot 10^{-6}$	$3.30 \cdot 10^{-8}$	$4.93 \cdot 10^{-8}$	$2.99 \cdot 10^{-6}$	$1.63 \cdot 10^{-1}$
630	$6.27 \cdot 10^{-5}$	$9.21 \cdot 10^{-6}$	$3.19 \cdot 10^{-8}$	$4.76 \cdot 10^{-8}$	$2.89 \cdot 10^{-6}$	$1.60 \cdot 10^{-1}$
640	$6.05 \cdot 10^{-5}$	$8.91 \cdot 10^{-6}$	$3.09 \cdot 10^{-8}$	$4.59 \cdot 10^{-8}$	$2.79 \cdot 10^{-6}$	$1.57 \cdot 10^{-1}$
650	$5.84 \cdot 10^{-5}$	$8.63 \cdot 10^{-6}$	$2.99 \cdot 10^{-8}$	$4.43 \cdot 10^{-8}$	$2.69 \cdot 10^{-6}$	$1.54 \cdot 10^{-1}$
660	$5.64 \cdot 10^{-5}$	$8.35 \cdot 10^{-6}$	$2.89 \cdot 10^{-8}$	$4.28 \cdot 10^{-8}$	$2.60 \cdot 10^{-6}$	$1.50 \cdot 10^{-1}$
670	$5.45 \cdot 10^{-5}$	$8.09 \cdot 10^{-6}$	$2.80 \cdot 10^{-8}$	$4.14 \cdot 10^{-8}$	$2.51 \cdot 10^{-6}$	$1.47 \cdot 10^{-1}$
680	$5.27 \cdot 10^{-5}$	$7.84 \cdot 10^{-6}$	$2.72 \cdot 10^{-8}$	$4.00 \cdot 10^{-8}$	$2.43 \cdot 10^{-6}$	$1.44 \cdot 10^{-1}$
690	$5.10 \cdot 10^{-5}$	$7.60 \cdot 10^{-6}$	$2.64 \cdot 10^{-8}$	$3.87 \cdot 10^{-8}$	$2.35 \cdot 10^{-6}$	$1.41 \cdot 10^{-1}$
700	$4.94 \cdot 10^{-5}$	$7.37 \cdot 10^{-6}$	$2.56 \cdot 10^{-8}$	$3.74 \cdot 10^{-8}$	$2.27 \cdot 10^{-6}$	$1.38 \cdot 10^{-1}$
710	$4.78 \cdot 10^{-5}$	$7.16 \cdot 10^{-6}$	$2.48 \cdot 10^{-8}$	$3.62 \cdot 10^{-8}$	$2.20 \cdot 10^{-6}$	$1.35 \cdot 10^{-1}$
720	$4.63 \cdot 10^{-5}$	$6.94 \cdot 10^{-6}$	$2.41 \cdot 10^{-8}$	$3.51 \cdot 10^{-8}$	$2.13 \cdot 10^{-6}$	$1.32 \cdot 10^{-1}$
730	$4.48 \cdot 10^{-5}$	$6.74 \cdot 10^{-6}$	$2.34 \cdot 10^{-8}$	$3.40 \cdot 10^{-8}$	$2.07 \cdot 10^{-6}$	$1.29 \cdot 10^{-1}$
740	$4.34 \cdot 10^{-5}$	$6.55 \cdot 10^{-6}$	$2.27 \cdot 10^{-8}$	$3.30 \cdot 10^{-8}$	$2.00 \cdot 10^{-6}$	$1.26 \cdot 10^{-1}$
750	$4.21 \cdot 10^{-5}$	$6.36 \cdot 10^{-6}$	$2.20 \cdot 10^{-8}$	$3.19 \cdot 10^{-8}$	$1.94 \cdot 10^{-6}$	$1.23 \cdot 10^{-1}$
760	$4.08 \cdot 10^{-5}$	$6.18 \cdot 10^{-6}$	$2.14 \cdot 10^{-8}$	$3.10 \cdot 10^{-8}$	$1.88 \cdot 10^{-6}$	$1.21 \cdot 10^{-1}$
770	$3.96 \cdot 10^{-5}$	$6.00 \cdot 10^{-6}$	$2.08 \cdot 10^{-8}$	$3.00 \cdot 10^{-8}$	$1.82 \cdot 10^{-6}$	$1.18 \cdot 10^{-1}$
780	$3.84 \cdot 10^{-5}$	$5.83 \cdot 10^{-6}$	$2.02 \cdot 10^{-8}$	$2.91 \cdot 10^{-8}$	$1.77 \cdot 10^{-6}$	$1.15 \cdot 10^{-1}$
790	$3.73 \cdot 10^{-5}$	$5.67 \cdot 10^{-6}$	$1.97 \cdot 10^{-8}$	$2.83 \cdot 10^{-8}$	$1.72 \cdot 10^{-6}$	$1.13 \cdot 10^{-1}$
800	$3.62 \cdot 10^{-5}$	$5.52 \cdot 10^{-6}$	$1.91 \cdot 10^{-8}$	$2.74 \cdot 10^{-8}$	$1.67 \cdot 10^{-6}$	$1.10 \cdot 10^{-1}$
810	$3.51 \cdot 10^{-5}$	$5.36 \cdot 10^{-6}$	$1.86 \cdot 10^{-8}$	$2.66 \cdot 10^{-8}$	$1.62 \cdot 10^{-6}$	$1.07 \cdot 10^{-1}$
820	$3.41 \cdot 10^{-5}$	$5.22 \cdot 10^{-6}$	$1.81 \cdot 10^{-8}$	$2.58 \cdot 10^{-8}$	$1.57 \cdot 10^{-6}$	$1.05 \cdot 10^{-1}$
830	$3.31 \cdot 10^{-5}$	$5.07 \cdot 10^{-6}$	$1.76 \cdot 10^{-8}$	$2.51 \cdot 10^{-8}$	$1.52 \cdot 10^{-6}$	$1.02 \cdot 10^{-1}$
840	$3.21 \cdot 10^{-5}$	$4.93 \cdot 10^{-6}$	$1.71 \cdot 10^{-8}$	$2.44 \cdot 10^{-8}$	$1.48 \cdot 10^{-6}$	$1.00 \cdot 10^{-1}$
850	$3.12 \cdot 10^{-5}$	$4.80 \cdot 10^{-6}$	$1.66 \cdot 10^{-8}$	$2.37 \cdot 10^{-8}$	$1.44 \cdot 10^{-6}$	$9.77 \cdot 10^{-2}$
860	$3.03 \cdot 10^{-5}$	$4.67 \cdot 10^{-6}$	$1.62 \cdot 10^{-8}$	$2.30 \cdot 10^{-8}$	$1.40 \cdot 10^{-6}$	$9.54 \cdot 10^{-2}$
870	$2.94 \cdot 10^{-5}$	$4.55 \cdot 10^{-6}$	$1.58 \cdot 10^{-8}$	$2.23 \cdot 10^{-8}$	$1.36 \cdot 10^{-6}$	$9.31 \cdot 10^{-2}$
880	$2.86 \cdot 10^{-5}$	$4.42 \cdot 10^{-6}$	$1.53 \cdot 10^{-8}$	$2.17 \cdot 10^{-8}$	$1.32 \cdot 10^{-6}$	$9.09 \cdot 10^{-2}$
890	$2.78 \cdot 10^{-5}$	$4.31 \cdot 10^{-6}$	$1.49 \cdot 10^{-8}$	$2.11 \cdot 10^{-8}$	$1.28 \cdot 10^{-6}$	$8.87 \cdot 10^{-2}$
900	$2.70 \cdot 10^{-5}$	$4.19 \cdot 10^{-6}$	$1.45 \cdot 10^{-8}$	$2.05 \cdot 10^{-8}$	$1.24 \cdot 10^{-6}$	$8.66 \cdot 10^{-2}$
910	$2.62 \cdot 10^{-5}$	$4.08 \cdot 10^{-6}$	$1.41 \cdot 10^{-8}$	$1.99 \cdot 10^{-8}$	$1.21 \cdot 10^{-6}$	$8.45 \cdot 10^{-2}$
920	$2.55 \cdot 10^{-5}$	$3.97 \cdot 10^{-6}$	$1.38 \cdot 10^{-8}$	$1.93 \cdot 10^{-8}$	$1.17 \cdot 10^{-6}$	$8.24 \cdot 10^{-2}$
930	$2.48 \cdot 10^{-5}$	$3.86 \cdot 10^{-6}$	$1.34 \cdot 10^{-8}$	$1.88 \cdot 10^{-8}$	$1.14 \cdot 10^{-6}$	$8.04 \cdot 10^{-2}$
940	$2.41 \cdot 10^{-5}$	$3.76 \cdot 10^{-6}$	$1.30 \cdot 10^{-8}$	$1.83 \cdot 10^{-8}$	$1.11 \cdot 10^{-6}$	$7.84 \cdot 10^{-2}$
950	$2.34 \cdot 10^{-5}$	$3.66 \cdot 10^{-6}$	$1.27 \cdot 10^{-8}$	$1.77 \cdot 10^{-8}$	$1.08 \cdot 10^{-6}$	$7.65 \cdot 10^{-2}$
960	$2.27 \cdot 10^{-5}$	$3.56 \cdot 10^{-6}$	$1.23 \cdot 10^{-8}$	$1.72 \cdot 10^{-8}$	$1.05 \cdot 10^{-6}$	$7.46 \cdot 10^{-2}$
970	$2.21 \cdot 10^{-5}$	$3.47 \cdot 10^{-6}$	$1.20 \cdot 10^{-8}$	$1.68 \cdot 10^{-8}$	$1.02 \cdot 10^{-6}$	$7.27 \cdot 10^{-2}$
980	$2.15 \cdot 10^{-5}$	$3.38 \cdot 10^{-6}$	$1.17 \cdot 10^{-8}$	$1.63 \cdot 10^{-8}$	$9.88 \cdot 10^{-7}$	$7.09 \cdot 10^{-2}$
990	$2.09 \cdot 10^{-5}$	$3.29 \cdot 10^{-6}$	$1.14 \cdot 10^{-8}$	$1.58 \cdot 10^{-8}$	$9.61 \cdot 10^{-7}$	$6.91 \cdot 10^{-2}$
1000	$2.03 \cdot 10^{-5}$	$3.20 \cdot 10^{-6}$	$1.11 \cdot 10^{-8}$	$1.54 \cdot 10^{-8}$	$9.34 \cdot 10^{-7}$	$6.74 \cdot 10^{-2}$

Table B.3: SM Higgs branching ratios in bosonic final states and Higgs total widths in the low- and intermediate-mass range.

M_H [GeV]	$H \to gg$	$H \to \gamma\gamma$	$H \to Z\gamma$	$H \to WW$	$H \to ZZ$	Total Γ_H [GeV]
90	$6.12 \cdot 10^{-2}$	$1.23 \cdot 10^{-3}$	0.00	$2.09 \cdot 10^{-3}$	$4.21 \cdot 10^{-4}$	$2.20 \cdot 10^{-3}$
95	$6.74 \cdot 10^{-2}$	$1.40 \cdot 10^{-3}$	$4.52 \cdot 10^{-6}$	$4.72 \cdot 10^{-3}$	$6.72 \cdot 10^{-4}$	$2.32 \cdot 10^{-3}$
100	$7.37 \cdot 10^{-2}$	$1.59 \cdot 10^{-3}$	$4.98 \cdot 10^{-5}$	$1.11 \cdot 10^{-2}$	$1.13 \cdot 10^{-3}$	$2.46 \cdot 10^{-3}$
105	$7.95 \cdot 10^{-2}$	$1.78 \cdot 10^{-3}$	$1.73 \cdot 10^{-4}$	$2.43 \cdot 10^{-2}$	$2.15 \cdot 10^{-3}$	$2.62 \cdot 10^{-3}$
110	$8.44 \cdot 10^{-2}$	$1.97 \cdot 10^{-3}$	$3.95 \cdot 10^{-4}$	$4.82 \cdot 10^{-2}$	$4.39 \cdot 10^{-3}$	$2.82 \cdot 10^{-3}$
115	$8.76 \cdot 10^{-2}$	$2.13 \cdot 10^{-3}$	$7.16 \cdot 10^{-4}$	$8.67 \cdot 10^{-2}$	$8.73 \cdot 10^{-3}$	$3.09 \cdot 10^{-3}$
120	$8.82 \cdot 10^{-2}$	$2.25 \cdot 10^{-3}$	$1.12 \cdot 10^{-3}$	$1.43 \cdot 10^{-1}$	$1.60 \cdot 10^{-2}$	$3.47 \cdot 10^{-3}$
125	$8.56 \cdot 10^{-2}$	$2.30 \cdot 10^{-3}$	$1.55 \cdot 10^{-3}$	$2.16 \cdot 10^{-1}$	$2.67 \cdot 10^{-2}$	$4.03 \cdot 10^{-3}$
130	$7.96 \cdot 10^{-2}$	$2.26 \cdot 10^{-3}$	$1.96 \cdot 10^{-3}$	$3.05 \cdot 10^{-1}$	$4.02 \cdot 10^{-2}$	$4.87 \cdot 10^{-3}$
135	$7.06 \cdot 10^{-2}$	$2.14 \cdot 10^{-3}$	$2.28 \cdot 10^{-3}$	$4.03 \cdot 10^{-1}$	$5.51 \cdot 10^{-2}$	$6.14 \cdot 10^{-3}$
140	$5.94 \cdot 10^{-2}$	$1.94 \cdot 10^{-3}$	$2.47 \cdot 10^{-3}$	$5.04 \cdot 10^{-1}$	$6.92 \cdot 10^{-2}$	$8.12 \cdot 10^{-3}$
145	$4.70 \cdot 10^{-2}$	$1.68 \cdot 10^{-3}$	$2.49 \cdot 10^{-3}$	$6.03 \cdot 10^{-1}$	$7.96 \cdot 10^{-2}$	$1.14 \cdot 10^{-2}$
150	$3.43 \cdot 10^{-2}$	$1.37 \cdot 10^{-3}$	$2.32 \cdot 10^{-3}$	$6.99 \cdot 10^{-1}$	$8.28 \cdot 10^{-2}$	$1.73 \cdot 10^{-2}$
155	$2.16 \cdot 10^{-2}$	$1.00 \cdot 10^{-3}$	$1.91 \cdot 10^{-3}$	$7.96 \cdot 10^{-1}$	$7.36 \cdot 10^{-2}$	$3.02 \cdot 10^{-2}$
160	$8.57 \cdot 10^{-3}$	$5.33 \cdot 10^{-4}$	$1.15 \cdot 10^{-3}$	$9.09 \cdot 10^{-1}$	$4.16 \cdot 10^{-2}$	$8.29 \cdot 10^{-2}$
165	$3.11 \cdot 10^{-3}$	$2.30 \cdot 10^{-4}$	$5.45 \cdot 10^{-4}$	$9.60 \cdot 10^{-1}$	$2.22 \cdot 10^{-2}$	$2.46 \cdot 10^{-1}$
170	$2.18 \cdot 10^{-3}$	$1.58 \cdot 10^{-4}$	$4.00 \cdot 10^{-4}$	$9.65 \cdot 10^{-1}$	$2.36 \cdot 10^{-2}$	$3.80 \cdot 10^{-1}$
175	$1.80 \cdot 10^{-3}$	$1.23 \cdot 10^{-4}$	$3.38 \cdot 10^{-4}$	$9.58 \cdot 10^{-1}$	$3.23 \cdot 10^{-2}$	$5.00 \cdot 10^{-1}$
180	$1.54 \cdot 10^{-3}$	$1.02 \cdot 10^{-4}$	$2.96 \cdot 10^{-4}$	$9.32 \cdot 10^{-1}$	$6.02 \cdot 10^{-2}$	$6.31 \cdot 10^{-1}$
185	$1.26 \cdot 10^{-3}$	$8.09 \cdot 10^{-5}$	$2.44 \cdot 10^{-4}$	$8.44 \cdot 10^{-1}$	$1.50 \cdot 10^{-1}$	$8.32 \cdot 10^{-1}$
190	$1.08 \cdot 10^{-3}$	$6.74 \cdot 10^{-5}$	$2.11 \cdot 10^{-4}$	$7.86 \cdot 10^{-1}$	$2.09 \cdot 10^{-1}$	1.04
195	$9.84 \cdot 10^{-4}$	$5.89 \cdot 10^{-5}$	$1.91 \cdot 10^{-4}$	$7.57 \cdot 10^{-1}$	$2.39 \cdot 10^{-1}$	1.24
200	$9.16 \cdot 10^{-4}$	$5.26 \cdot 10^{-5}$	$1.75 \cdot 10^{-4}$	$7.41 \cdot 10^{-1}$	$2.56 \cdot 10^{-1}$	1.43
210	$8.27 \cdot 10^{-4}$	$4.34 \cdot 10^{-5}$	$1.52 \cdot 10^{-4}$	$7.23 \cdot 10^{-1}$	$2.74 \cdot 10^{-1}$	1.85
220	$7.69 \cdot 10^{-4}$	$3.67 \cdot 10^{-5}$	$1.34 \cdot 10^{-4}$	$7.14 \cdot 10^{-1}$	$2.84 \cdot 10^{-1}$	2.31
230	$7.27 \cdot 10^{-4}$	$3.14 \cdot 10^{-5}$	$1.19 \cdot 10^{-4}$	$7.08 \cdot 10^{-1}$	$2.89 \cdot 10^{-1}$	2.82
240	$6.97 \cdot 10^{-4}$	$2.72 \cdot 10^{-5}$	$1.07 \cdot 10^{-4}$	$7.04 \cdot 10^{-1}$	$2.94 \cdot 10^{-1}$	3.40
250	$6.75 \cdot 10^{-4}$	$2.37 \cdot 10^{-5}$	$9.54 \cdot 10^{-5}$	$7.01 \cdot 10^{-1}$	$2.97 \cdot 10^{-1}$	4.04
260	$6.59 \cdot 10^{-4}$	$2.08 \cdot 10^{-5}$	$8.57 \cdot 10^{-5}$	$6.99 \cdot 10^{-1}$	$2.99 \cdot 10^{-1}$	4.76
270	$6.48 \cdot 10^{-4}$	$1.84 \cdot 10^{-5}$	$7.72 \cdot 10^{-5}$	$6.97 \cdot 10^{-1}$	$3.02 \cdot 10^{-1}$	5.55
280	$6.42 \cdot 10^{-4}$	$1.63 \cdot 10^{-5}$	$6.98 \cdot 10^{-5}$	$6.95 \cdot 10^{-1}$	$3.04 \cdot 10^{-1}$	6.43
290	$6.42 \cdot 10^{-4}$	$1.45 \cdot 10^{-5}$	$6.32 \cdot 10^{-5}$	$6.93 \cdot 10^{-1}$	$3.05 \cdot 10^{-1}$	7.39
300	$6.46 \cdot 10^{-4}$	$1.30 \cdot 10^{-5}$	$5.75 \cdot 10^{-5}$	$6.92 \cdot 10^{-1}$	$3.07 \cdot 10^{-1}$	8.43
310	$6.56 \cdot 10^{-4}$	$1.17 \cdot 10^{-5}$	$5.24 \cdot 10^{-5}$	$6.90 \cdot 10^{-1}$	$3.08 \cdot 10^{-1}$	9.57
320	$6.73 \cdot 10^{-4}$	$1.05 \cdot 10^{-5}$	$4.79 \cdot 10^{-5}$	$6.89 \cdot 10^{-1}$	$3.09 \cdot 10^{-1}$	10.8
330	$6.99 \cdot 10^{-4}$	$9.56 \cdot 10^{-6}$	$4.39 \cdot 10^{-5}$	$6.88 \cdot 10^{-1}$	$3.10 \cdot 10^{-1}$	12.1
340	$7.42 \cdot 10^{-4}$	$8.73 \cdot 10^{-6}$	$4.04 \cdot 10^{-5}$	$6.87 \cdot 10^{-1}$	$3.11 \cdot 10^{-1}$	13.5
350	$8.05 \cdot 10^{-4}$	$7.62 \cdot 10^{-6}$	$3.65 \cdot 10^{-5}$	$6.76 \cdot 10^{-1}$	$3.07 \cdot 10^{-1}$	15.2
360	$8.42 \cdot 10^{-4}$	$6.10 \cdot 10^{-6}$	$3.17 \cdot 10^{-5}$	$6.51 \cdot 10^{-1}$	$2.97 \cdot 10^{-1}$	17.6
370	$8.54 \cdot 10^{-4}$	$4.85 \cdot 10^{-6}$	$2.76 \cdot 10^{-5}$	$6.28 \cdot 10^{-1}$	$2.87 \cdot 10^{-1}$	20.2
380	$8.51 \cdot 10^{-4}$	$3.86 \cdot 10^{-6}$	$2.42 \cdot 10^{-5}$	$6.09 \cdot 10^{-1}$	$2.79 \cdot 10^{-1}$	23.1
390	$8.40 \cdot 10^{-4}$	$3.09 \cdot 10^{-6}$	$2.14 \cdot 10^{-5}$	$5.94 \cdot 10^{-1}$	$2.73 \cdot 10^{-1}$	26.1
400	$8.22 \cdot 10^{-4}$	$2.47 \cdot 10^{-6}$	$1.90 \cdot 10^{-5}$	$5.82 \cdot 10^{-1}$	$2.69 \cdot 10^{-1}$	29.2
410	$8.02 \cdot 10^{-4}$	$1.98 \cdot 10^{-6}$	$1.70 \cdot 10^{-5}$	$5.72 \cdot 10^{-1}$	$2.65 \cdot 10^{-1}$	32.5
420	$7.80 \cdot 10^{-4}$	$1.60 \cdot 10^{-6}$	$1.53 \cdot 10^{-5}$	$5.64 \cdot 10^{-1}$	$2.63 \cdot 10^{-1}$	35.9
430	$7.56 \cdot 10^{-4}$	$1.28 \cdot 10^{-6}$	$1.38 \cdot 10^{-5}$	$5.59 \cdot 10^{-1}$	$2.61 \cdot 10^{-1}$	39.4
440	$7.33 \cdot 10^{-4}$	$1.03 \cdot 10^{-6}$	$1.26 \cdot 10^{-5}$	$5.54 \cdot 10^{-1}$	$2.60 \cdot 10^{-1}$	43.1
450	$7.09 \cdot 10^{-4}$	$8.27 \cdot 10^{-7}$	$1.15 \cdot 10^{-5}$	$5.51 \cdot 10^{-1}$	$2.59 \cdot 10^{-1}$	46.9
460	$6.85 \cdot 10^{-4}$	$6.62 \cdot 10^{-7}$	$1.05 \cdot 10^{-5}$	$5.49 \cdot 10^{-1}$	$2.59 \cdot 10^{-1}$	50.8
470	$6.62 \cdot 10^{-4}$	$5.29 \cdot 10^{-7}$	$9.64 \cdot 10^{-6}$	$5.47 \cdot 10^{-1}$	$2.59 \cdot 10^{-1}$	54.9
480	$6.39 \cdot 10^{-4}$	$4.21 \cdot 10^{-7}$	$8.87 \cdot 10^{-6}$	$5.46 \cdot 10^{-1}$	$2.59 \cdot 10^{-1}$	59.1
490	$6.17 \cdot 10^{-4}$	$3.34 \cdot 10^{-7}$	$8.19 \cdot 10^{-6}$	$5.46 \cdot 10^{-1}$	$2.60 \cdot 10^{-1}$	63.5

Table B.4: SM Higgs branching ratios in bosonic final states and Higgs total widths in the high-mass range.

M_H [GeV]	$H \to gg$	$H \to \gamma\gamma$	$H \to Z\gamma$	$H \to WW$	$H \to ZZ$	Total Γ_H [GeV]
500	$5.96 \cdot 10^{-4}$	$2.64 \cdot 10^{-7}$	$7.58 \cdot 10^{-6}$	$5.46 \cdot 10^{-1}$	$2.61 \cdot 10^{-1}$	68.0
510	$5.75 \cdot 10^{-4}$	$2.09 \cdot 10^{-7}$	$7.03 \cdot 10^{-6}$	$5.46 \cdot 10^{-1}$	$2.61 \cdot 10^{-1}$	72.7
520	$5.55 \cdot 10^{-4}$	$1.65 \cdot 10^{-7}$	$6.53 \cdot 10^{-6}$	$5.47 \cdot 10^{-1}$	$2.62 \cdot 10^{-1}$	77.6
530	$5.36 \cdot 10^{-4}$	$1.30 \cdot 10^{-7}$	$6.08 \cdot 10^{-6}$	$5.48 \cdot 10^{-1}$	$2.63 \cdot 10^{-1}$	82.6
540	$5.17 \cdot 10^{-4}$	$1.04 \cdot 10^{-7}$	$5.67 \cdot 10^{-6}$	$5.49 \cdot 10^{-1}$	$2.65 \cdot 10^{-1}$	87.7
550	$4.99 \cdot 10^{-4}$	$8.52 \cdot 10^{-8}$	$5.30 \cdot 10^{-6}$	$5.50 \cdot 10^{-1}$	$2.66 \cdot 10^{-1}$	93.1
560	$4.82 \cdot 10^{-4}$	$7.16 \cdot 10^{-8}$	$4.95 \cdot 10^{-6}$	$5.51 \cdot 10^{-1}$	$2.67 \cdot 10^{-1}$	98.7
570	$4.65 \cdot 10^{-4}$	$6.28 \cdot 10^{-8}$	$4.64 \cdot 10^{-6}$	$5.53 \cdot 10^{-1}$	$2.68 \cdot 10^{-1}$	104
580	$4.49 \cdot 10^{-4}$	$5.80 \cdot 10^{-8}$	$4.35 \cdot 10^{-6}$	$5.55 \cdot 10^{-1}$	$2.70 \cdot 10^{-1}$	110
590	$4.34 \cdot 10^{-4}$	$5.64 \cdot 10^{-8}$	$4.08 \cdot 10^{-6}$	$5.56 \cdot 10^{-1}$	$2.71 \cdot 10^{-1}$	116
600	$4.19 \cdot 10^{-4}$	$5.77 \cdot 10^{-8}$	$3.84 \cdot 10^{-6}$	$5.58 \cdot 10^{-1}$	$2.72 \cdot 10^{-1}$	123
610	$4.04 \cdot 10^{-4}$	$6.12 \cdot 10^{-8}$	$3.61 \cdot 10^{-6}$	$5.60 \cdot 10^{-1}$	$2.73 \cdot 10^{-1}$	129
620	$3.90 \cdot 10^{-4}$	$6.66 \cdot 10^{-8}$	$3.40 \cdot 10^{-6}$	$5.62 \cdot 10^{-1}$	$2.75 \cdot 10^{-1}$	136
630	$3.77 \cdot 10^{-4}$	$7.36 \cdot 10^{-8}$	$3.21 \cdot 10^{-6}$	$5.64 \cdot 10^{-1}$	$2.76 \cdot 10^{-1}$	143
640	$3.65 \cdot 10^{-4}$	$8.19 \cdot 10^{-8}$	$3.03 \cdot 10^{-6}$	$5.66 \cdot 10^{-1}$	$2.77 \cdot 10^{-1}$	150
650	$3.52 \cdot 10^{-4}$	$9.12 \cdot 10^{-8}$	$2.86 \cdot 10^{-6}$	$5.67 \cdot 10^{-1}$	$2.79 \cdot 10^{-1}$	158
660	$3.40 \cdot 10^{-4}$	$1.01 \cdot 10^{-7}$	$2.70 \cdot 10^{-6}$	$5.69 \cdot 10^{-1}$	$2.80 \cdot 10^{-1}$	166
670	$3.29 \cdot 10^{-4}$	$1.12 \cdot 10^{-7}$	$2.56 \cdot 10^{-6}$	$5.71 \cdot 10^{-1}$	$2.81 \cdot 10^{-1}$	174
680	$3.18 \cdot 10^{-4}$	$1.23 \cdot 10^{-7}$	$2.42 \cdot 10^{-6}$	$5.73 \cdot 10^{-1}$	$2.82 \cdot 10^{-1}$	182
690	$3.07 \cdot 10^{-4}$	$1.35 \cdot 10^{-7}$	$2.29 \cdot 10^{-6}$	$5.75 \cdot 10^{-1}$	$2.83 \cdot 10^{-1}$	190
700	$2.97 \cdot 10^{-4}$	$1.47 \cdot 10^{-7}$	$2.18 \cdot 10^{-6}$	$5.77 \cdot 10^{-1}$	$2.85 \cdot 10^{-1}$	199
710	$2.87 \cdot 10^{-4}$	$1.59 \cdot 10^{-7}$	$2.06 \cdot 10^{-6}$	$5.79 \cdot 10^{-1}$	$2.86 \cdot 10^{-1}$	208
720	$2.78 \cdot 10^{-4}$	$1.71 \cdot 10^{-7}$	$1.96 \cdot 10^{-6}$	$5.81 \cdot 10^{-1}$	$2.87 \cdot 10^{-1}$	218
730	$2.69 \cdot 10^{-4}$	$1.83 \cdot 10^{-7}$	$1.86 \cdot 10^{-6}$	$5.82 \cdot 10^{-1}$	$2.88 \cdot 10^{-1}$	227
740	$2.60 \cdot 10^{-4}$	$1.95 \cdot 10^{-7}$	$1.77 \cdot 10^{-6}$	$5.84 \cdot 10^{-1}$	$2.89 \cdot 10^{-1}$	237
750	$2.51 \cdot 10^{-4}$	$2.07 \cdot 10^{-7}$	$1.69 \cdot 10^{-6}$	$5.86 \cdot 10^{-1}$	$2.90 \cdot 10^{-1}$	248
760	$2.43 \cdot 10^{-4}$	$2.19 \cdot 10^{-7}$	$1.61 \cdot 10^{-6}$	$5.88 \cdot 10^{-1}$	$2.91 \cdot 10^{-1}$	258
770	$2.36 \cdot 10^{-4}$	$2.30 \cdot 10^{-7}$	$1.53 \cdot 10^{-6}$	$5.89 \cdot 10^{-1}$	$2.92 \cdot 10^{-1}$	269
780	$2.28 \cdot 10^{-4}$	$2.41 \cdot 10^{-7}$	$1.46 \cdot 10^{-6}$	$5.91 \cdot 10^{-1}$	$2.93 \cdot 10^{-1}$	281
790	$2.21 \cdot 10^{-4}$	$2.53 \cdot 10^{-7}$	$1.40 \cdot 10^{-6}$	$5.93 \cdot 10^{-1}$	$2.94 \cdot 10^{-1}$	292
800	$2.14 \cdot 10^{-4}$	$2.63 \cdot 10^{-7}$	$1.33 \cdot 10^{-6}$	$5.94 \cdot 10^{-1}$	$2.95 \cdot 10^{-1}$	304
810	$2.07 \cdot 10^{-4}$	$2.74 \cdot 10^{-7}$	$1.27 \cdot 10^{-6}$	$5.96 \cdot 10^{-1}$	$2.96 \cdot 10^{-1}$	317
820	$2.00 \cdot 10^{-4}$	$2.84 \cdot 10^{-7}$	$1.22 \cdot 10^{-6}$	$5.97 \cdot 10^{-1}$	$2.97 \cdot 10^{-1}$	330
830	$1.94 \cdot 10^{-4}$	$2.94 \cdot 10^{-7}$	$1.16 \cdot 10^{-6}$	$5.99 \cdot 10^{-1}$	$2.98 \cdot 10^{-1}$	343
840	$1.88 \cdot 10^{-4}$	$3.04 \cdot 10^{-7}$	$1.12 \cdot 10^{-6}$	$6.01 \cdot 10^{-1}$	$2.99 \cdot 10^{-1}$	357
850	$1.82 \cdot 10^{-4}$	$3.13 \cdot 10^{-7}$	$1.07 \cdot 10^{-6}$	$6.02 \cdot 10^{-1}$	$3.00 \cdot 10^{-1}$	371
860	$1.76 \cdot 10^{-4}$	$3.22 \cdot 10^{-7}$	$1.02 \cdot 10^{-6}$	$6.03 \cdot 10^{-1}$	$3.01 \cdot 10^{-1}$	386
870	$1.71 \cdot 10^{-4}$	$3.30 \cdot 10^{-7}$	$9.83 \cdot 10^{-7}$	$6.05 \cdot 10^{-1}$	$3.02 \cdot 10^{-1}$	401
880	$1.65 \cdot 10^{-4}$	$3.39 \cdot 10^{-7}$	$9.44 \cdot 10^{-7}$	$6.06 \cdot 10^{-1}$	$3.03 \cdot 10^{-1}$	416
890	$1.60 \cdot 10^{-4}$	$3.47 \cdot 10^{-7}$	$9.07 \cdot 10^{-7}$	$6.08 \cdot 10^{-1}$	$3.03 \cdot 10^{-1}$	432
900	$1.55 \cdot 10^{-4}$	$3.54 \cdot 10^{-7}$	$8.72 \cdot 10^{-7}$	$6.09 \cdot 10^{-1}$	$3.04 \cdot 10^{-1}$	449
910	$1.50 \cdot 10^{-4}$	$3.61 \cdot 10^{-7}$	$8.38 \cdot 10^{-7}$	$6.10 \cdot 10^{-1}$	$3.05 \cdot 10^{-1}$	466
920	$1.46 \cdot 10^{-4}$	$3.67 \cdot 10^{-7}$	$8.07 \cdot 10^{-7}$	$6.12 \cdot 10^{-1}$	$3.06 \cdot 10^{-1}$	484
930	$1.41 \cdot 10^{-4}$	$3.75 \cdot 10^{-7}$	$7.77 \cdot 10^{-7}$	$6.13 \cdot 10^{-1}$	$3.06 \cdot 10^{-1}$	502
940	$1.37 \cdot 10^{-4}$	$3.81 \cdot 10^{-7}$	$7.49 \cdot 10^{-7}$	$6.14 \cdot 10^{-1}$	$3.07 \cdot 10^{-1}$	521
950	$1.33 \cdot 10^{-4}$	$3.87 \cdot 10^{-7}$	$7.22 \cdot 10^{-7}$	$6.16 \cdot 10^{-1}$	$3.08 \cdot 10^{-1}$	540
960	$1.29 \cdot 10^{-4}$	$3.93 \cdot 10^{-7}$	$6.97 \cdot 10^{-7}$	$6.17 \cdot 10^{-1}$	$3.08 \cdot 10^{-1}$	560
970	$1.25 \cdot 10^{-4}$	$3.98 \cdot 10^{-7}$	$6.73 \cdot 10^{-7}$	$6.18 \cdot 10^{-1}$	$3.09 \cdot 10^{-1}$	581
980	$1.21 \cdot 10^{-4}$	$4.03 \cdot 10^{-7}$	$6.50 \cdot 10^{-7}$	$6.19 \cdot 10^{-1}$	$3.10 \cdot 10^{-1}$	602
990	$1.17 \cdot 10^{-4}$	$4.07 \cdot 10^{-7}$	$6.29 \cdot 10^{-7}$	$6.20 \cdot 10^{-1}$	$3.10 \cdot 10^{-1}$	624
1000	$1.14 \cdot 10^{-4}$	$4.12 \cdot 10^{-7}$	$6.08 \cdot 10^{-7}$	$6.21 \cdot 10^{-1}$	$3.11 \cdot 10^{-1}$	647

Table B.5: SM Higgs branching ratios for 4-fermion final states for the low- and intermediate-mass range.

M_H [GeV]	$H \to 4e$	$H \to 2e2\mu$	$H \to 4\ell$	$H \to 4q$	$H \to 2\ell 2q$	$H \to 4f$
90	$7.08 \cdot 10^{-7}$	$9.39 \cdot 10^{-7}$	$2.39 \cdot 10^{-4}$	$1.06 \cdot 10^{-3}$	$1.09 \cdot 10^{-3}$	$2.40 \cdot 10^{-3}$
95	$1.11 \cdot 10^{-6}$	$1.49 \cdot 10^{-6}$	$5.29 \cdot 10^{-4}$	$2.34 \cdot 10^{-3}$	$2.36 \cdot 10^{-3}$	$5.21 \cdot 10^{-3}$
100	$1.80 \cdot 10^{-6}$	$2.51 \cdot 10^{-6}$	$1.22 \cdot 10^{-3}$	$5.41 \cdot 10^{-3}$	$5.33 \cdot 10^{-3}$	$1.20 \cdot 10^{-2}$
105	$3.21 \cdot 10^{-6}$	$4.78 \cdot 10^{-6}$	$2.69 \cdot 10^{-3}$	$1.18 \cdot 10^{-2}$	$1.16 \cdot 10^{-2}$	$2.60 \cdot 10^{-2}$
110	$6.10 \cdot 10^{-6}$	$9.78 \cdot 10^{-6}$	$5.39 \cdot 10^{-3}$	$2.36 \cdot 10^{-2}$	$2.30 \cdot 10^{-2}$	$5.22 \cdot 10^{-2}$
115	$1.15 \cdot 10^{-5}$	$1.95 \cdot 10^{-5}$	$9.81 \cdot 10^{-3}$	$4.30 \cdot 10^{-2}$	$4.17 \cdot 10^{-2}$	$9.45 \cdot 10^{-2}$
120	$2.03 \cdot 10^{-5}$	$3.60 \cdot 10^{-5}$	$1.63 \cdot 10^{-2}$	$7.20 \cdot 10^{-2}$	$6.94 \cdot 10^{-2}$	$1.57 \cdot 10^{-1}$
125	$3.30 \cdot 10^{-5}$	$5.98 \cdot 10^{-5}$	$2.50 \cdot 10^{-2}$	$1.11 \cdot 10^{-1}$	$1.06 \cdot 10^{-1}$	$2.42 \cdot 10^{-1}$
130	$4.89 \cdot 10^{-5}$	$9.03 \cdot 10^{-5}$	$3.55 \cdot 10^{-2}$	$1.57 \cdot 10^{-1}$	$1.51 \cdot 10^{-1}$	$3.43 \cdot 10^{-1}$
135	$6.63 \cdot 10^{-5}$	$1.24 \cdot 10^{-4}$	$4.73 \cdot 10^{-2}$	$2.09 \cdot 10^{-1}$	$2.00 \cdot 10^{-1}$	$4.56 \cdot 10^{-1}$
140	$8.25 \cdot 10^{-5}$	$1.56 \cdot 10^{-4}$	$5.93 \cdot 10^{-2}$	$2.62 \cdot 10^{-1}$	$2.51 \cdot 10^{-1}$	$5.71 \cdot 10^{-1}$
145	$9.43 \cdot 10^{-5}$	$1.79 \cdot 10^{-4}$	$7.07 \cdot 10^{-2}$	$3.12 \cdot 10^{-1}$	$2.99 \cdot 10^{-1}$	$6.81 \cdot 10^{-1}$
150	$9.76 \cdot 10^{-5}$	$1.87 \cdot 10^{-4}$	$8.12 \cdot 10^{-2}$	$3.57 \cdot 10^{-1}$	$3.42 \cdot 10^{-1}$	$7.83 \cdot 10^{-1}$
155	$8.63 \cdot 10^{-5}$	$1.66 \cdot 10^{-4}$	$9.10 \cdot 10^{-2}$	$3.97 \cdot 10^{-1}$	$3.81 \cdot 10^{-1}$	$8.70 \cdot 10^{-1}$
160	$4.85 \cdot 10^{-5}$	$9.36 \cdot 10^{-5}$	$1.00 \cdot 10^{-1}$	$4.33 \cdot 10^{-1}$	$4.18 \cdot 10^{-1}$	$9.50 \cdot 10^{-1}$
165	$2.58 \cdot 10^{-5}$	$5.00 \cdot 10^{-5}$	$1.04 \cdot 10^{-1}$	$4.47 \cdot 10^{-1}$	$4.31 \cdot 10^{-1}$	$9.83 \cdot 10^{-1}$
170	$2.73 \cdot 10^{-5}$	$5.32 \cdot 10^{-5}$	$1.04 \cdot 10^{-1}$	$4.50 \cdot 10^{-1}$	$4.34 \cdot 10^{-1}$	$9.87 \cdot 10^{-1}$
175	$3.71 \cdot 10^{-5}$	$7.28 \cdot 10^{-5}$	$1.05 \cdot 10^{-1}$	$4.52 \cdot 10^{-1}$	$4.36 \cdot 10^{-1}$	$9.91 \cdot 10^{-1}$
180	$6.85 \cdot 10^{-5}$	$1.36 \cdot 10^{-4}$	$1.04 \cdot 10^{-1}$	$4.53 \cdot 10^{-1}$	$4.34 \cdot 10^{-1}$	$9.93 \cdot 10^{-1}$
185	$1.70 \cdot 10^{-4}$	$3.38 \cdot 10^{-4}$	$1.03 \cdot 10^{-1}$	$4.57 \cdot 10^{-1}$	$4.34 \cdot 10^{-1}$	$9.94 \cdot 10^{-1}$
190	$2.36 \cdot 10^{-4}$	$4.72 \cdot 10^{-4}$	$1.02 \cdot 10^{-1}$	$4.60 \cdot 10^{-1}$	$4.34 \cdot 10^{-1}$	$9.90 \cdot 10^{-1}$
195	$2.69 \cdot 10^{-4}$	$5.37 \cdot 10^{-4}$	$1.02 \cdot 10^{-1}$	$4.60 \cdot 10^{-1}$	$4.33 \cdot 10^{-1}$	$9.95 \cdot 10^{-1}$
200	$2.88 \cdot 10^{-4}$	$5.75 \cdot 10^{-4}$	$1.02 \cdot 10^{-1}$	$4.61 \cdot 10^{-1}$	$4.33 \cdot 10^{-1}$	$9.98 \cdot 10^{-1}$
210	$3.08 \cdot 10^{-4}$	$6.17 \cdot 10^{-4}$	$1.01 \cdot 10^{-1}$	$4.62 \cdot 10^{-1}$	$4.33 \cdot 10^{-1}$	$9.96 \cdot 10^{-1}$
220	$3.19 \cdot 10^{-4}$	$6.38 \cdot 10^{-4}$	$1.01 \cdot 10^{-1}$	$4.64 \cdot 10^{-1}$	$4.33 \cdot 10^{-1}$	$9.98 \cdot 10^{-1}$
230	$3.26 \cdot 10^{-4}$	$6.52 \cdot 10^{-4}$	$1.01 \cdot 10^{-1}$	$4.65 \cdot 10^{-1}$	$4.33 \cdot 10^{-1}$	$9.97 \cdot 10^{-1}$
240	$3.31 \cdot 10^{-4}$	$6.61 \cdot 10^{-4}$	$1.01 \cdot 10^{-1}$	$4.62 \cdot 10^{-1}$	$4.33 \cdot 10^{-1}$	$9.98 \cdot 10^{-1}$
250	$3.34 \cdot 10^{-4}$	$6.68 \cdot 10^{-4}$	$1.01 \cdot 10^{-1}$	$4.63 \cdot 10^{-1}$	$4.33 \cdot 10^{-1}$	$9.97 \cdot 10^{-1}$
260	$3.37 \cdot 10^{-4}$	$6.74 \cdot 10^{-4}$	$1.01 \cdot 10^{-1}$	$4.65 \cdot 10^{-1}$	$4.33 \cdot 10^{-1}$	$9.98 \cdot 10^{-1}$
270	$3.40 \cdot 10^{-4}$	$6.79 \cdot 10^{-4}$	$1.01 \cdot 10^{-1}$	$4.65 \cdot 10^{-1}$	$4.32 \cdot 10^{-1}$	$9.98 \cdot 10^{-1}$
280	$3.42 \cdot 10^{-4}$	$6.83 \cdot 10^{-4}$	$1.01 \cdot 10^{-1}$	$4.64 \cdot 10^{-1}$	$4.33 \cdot 10^{-1}$	$9.99 \cdot 10^{-1}$
290	$3.44 \cdot 10^{-4}$	$6.87 \cdot 10^{-4}$	$1.01 \cdot 10^{-1}$	$4.64 \cdot 10^{-1}$	$4.33 \cdot 10^{-1}$	$9.98 \cdot 10^{-1}$
300	$3.45 \cdot 10^{-4}$	$6.90 \cdot 10^{-4}$	$1.01 \cdot 10^{-1}$	$4.64 \cdot 10^{-1}$	$4.33 \cdot 10^{-1}$	$9.99 \cdot 10^{-1}$
310	$3.47 \cdot 10^{-4}$	$6.93 \cdot 10^{-4}$	$1.01 \cdot 10^{-1}$	$4.64 \cdot 10^{-1}$	$4.33 \cdot 10^{-1}$	$9.98 \cdot 10^{-1}$
320	$3.48 \cdot 10^{-4}$	$6.96 \cdot 10^{-4}$	$1.01 \cdot 10^{-1}$	$4.64 \cdot 10^{-1}$	$4.33 \cdot 10^{-1}$	1.00
330	$3.49 \cdot 10^{-4}$	$6.98 \cdot 10^{-4}$	$1.01 \cdot 10^{-1}$	$4.64 \cdot 10^{-1}$	$4.33 \cdot 10^{-1}$	1.00
340	$3.50 \cdot 10^{-4}$	$6.99 \cdot 10^{-4}$	$1.01 \cdot 10^{-1}$	$4.64 \cdot 10^{-1}$	$4.32 \cdot 10^{-1}$	1.00
350	$3.45 \cdot 10^{-4}$	$6.90 \cdot 10^{-4}$	$9.95 \cdot 10^{-2}$	$4.57 \cdot 10^{-1}$	$4.26 \cdot 10^{-1}$	$9.82 \cdot 10^{-1}$
360	$3.34 \cdot 10^{-4}$	$6.67 \cdot 10^{-4}$	$9.61 \cdot 10^{-2}$	$4.41 \cdot 10^{-1}$	$4.10 \cdot 10^{-1}$	$9.49 \cdot 10^{-1}$
370	$3.23 \cdot 10^{-4}$	$6.46 \cdot 10^{-4}$	$9.24 \cdot 10^{-2}$	$4.26 \cdot 10^{-1}$	$3.97 \cdot 10^{-1}$	$9.14 \cdot 10^{-1}$
380	$3.15 \cdot 10^{-4}$	$6.29 \cdot 10^{-4}$	$9.01 \cdot 10^{-2}$	$4.13 \cdot 10^{-1}$	$3.85 \cdot 10^{-1}$	$8.88 \cdot 10^{-1}$
390	$3.08 \cdot 10^{-4}$	$6.15 \cdot 10^{-4}$	$8.78 \cdot 10^{-2}$	$4.03 \cdot 10^{-1}$	$3.76 \cdot 10^{-1}$	$8.67 \cdot 10^{-1}$
400	$3.03 \cdot 10^{-4}$	$6.05 \cdot 10^{-4}$	$8.59 \cdot 10^{-2}$	$3.97 \cdot 10^{-1}$	$3.70 \cdot 10^{-1}$	$8.49 \cdot 10^{-1}$
410	$2.99 \cdot 10^{-4}$	$5.98 \cdot 10^{-4}$	$8.47 \cdot 10^{-2}$	$3.91 \cdot 10^{-1}$	$3.63 \cdot 10^{-1}$	$8.38 \cdot 10^{-1}$
420	$2.96 \cdot 10^{-4}$	$5.92 \cdot 10^{-4}$	$8.36 \cdot 10^{-2}$	$3.85 \cdot 10^{-1}$	$3.60 \cdot 10^{-1}$	$8.28 \cdot 10^{-1}$
430	$2.94 \cdot 10^{-4}$	$5.88 \cdot 10^{-4}$	$8.30 \cdot 10^{-2}$	$3.81 \cdot 10^{-1}$	$3.55 \cdot 10^{-1}$	$8.19 \cdot 10^{-1}$
440	$2.93 \cdot 10^{-4}$	$5.86 \cdot 10^{-4}$	$8.24 \cdot 10^{-2}$	$3.78 \cdot 10^{-1}$	$3.53 \cdot 10^{-1}$	$8.15 \cdot 10^{-1}$
450	$2.92 \cdot 10^{-4}$	$5.84 \cdot 10^{-4}$	$8.19 \cdot 10^{-2}$	$3.78 \cdot 10^{-1}$	$3.52 \cdot 10^{-1}$	$8.10 \cdot 10^{-1}$
460	$2.92 \cdot 10^{-4}$	$5.84 \cdot 10^{-4}$	$8.17 \cdot 10^{-2}$	$3.76 \cdot 10^{-1}$	$3.50 \cdot 10^{-1}$	$8.07 \cdot 10^{-1}$
470	$2.92 \cdot 10^{-4}$	$5.84 \cdot 10^{-4}$	$8.16 \cdot 10^{-2}$	$3.75 \cdot 10^{-1}$	$3.50 \cdot 10^{-1}$	$8.07 \cdot 10^{-1}$
480	$2.92 \cdot 10^{-4}$	$5.85 \cdot 10^{-4}$	$8.15 \cdot 10^{-2}$	$3.76 \cdot 10^{-1}$	$3.48 \cdot 10^{-1}$	$8.05 \cdot 10^{-1}$
490	$2.93 \cdot 10^{-4}$	$5.86 \cdot 10^{-4}$	$8.16 \cdot 10^{-2}$	$3.75 \cdot 10^{-1}$	$3.50 \cdot 10^{-1}$	$8.06 \cdot 10^{-1}$

Table B.6: SM Higgs branching ratios for 4-fermion final states for the high-mass range.

M_H [GeV]	$H \to 4e$	$H \to 2e2\mu$	$H \to 4\ell$	$H \to 4q$	$H \to 2\ell 2q$	$H \to 4f$
500	$2.94 \cdot 10^{-4}$	$5.88 \cdot 10^{-4}$	$8.16 \cdot 10^{-2}$	$3.75 \cdot 10^{-1}$	$3.50 \cdot 10^{-1}$	$8.06 \cdot 10^{-1}$
510	$2.95 \cdot 10^{-4}$	$5.90 \cdot 10^{-4}$	$8.17 \cdot 10^{-2}$	$3.76 \cdot 10^{-1}$	$3.51 \cdot 10^{-1}$	$8.07 \cdot 10^{-1}$
520	$2.96 \cdot 10^{-4}$	$5.92 \cdot 10^{-4}$	$8.19 \cdot 10^{-2}$	$3.77 \cdot 10^{-1}$	$3.51 \cdot 10^{-1}$	$8.09 \cdot 10^{-1}$
530	$2.97 \cdot 10^{-4}$	$5.94 \cdot 10^{-4}$	$8.21 \cdot 10^{-2}$	$3.78 \cdot 10^{-1}$	$3.51 \cdot 10^{-1}$	$8.12 \cdot 10^{-1}$
540	$2.98 \cdot 10^{-4}$	$5.97 \cdot 10^{-4}$	$8.23 \cdot 10^{-2}$	$3.78 \cdot 10^{-1}$	$3.52 \cdot 10^{-1}$	$8.14 \cdot 10^{-1}$
550	$3.00 \cdot 10^{-4}$	$6.00 \cdot 10^{-4}$	$8.26 \cdot 10^{-2}$	$3.79 \cdot 10^{-1}$	$3.53 \cdot 10^{-1}$	$8.16 \cdot 10^{-1}$
560	$3.01 \cdot 10^{-4}$	$6.03 \cdot 10^{-4}$	$8.28 \cdot 10^{-2}$	$3.81 \cdot 10^{-1}$	$3.55 \cdot 10^{-1}$	$8.18 \cdot 10^{-1}$
570	$3.03 \cdot 10^{-4}$	$6.05 \cdot 10^{-4}$	$8.31 \cdot 10^{-2}$	$3.82 \cdot 10^{-1}$	$3.56 \cdot 10^{-1}$	$8.21 \cdot 10^{-1}$
580	$3.04 \cdot 10^{-4}$	$6.08 \cdot 10^{-4}$	$8.34 \cdot 10^{-2}$	$3.83 \cdot 10^{-1}$	$3.57 \cdot 10^{-1}$	$8.24 \cdot 10^{-1}$
590	$3.06 \cdot 10^{-4}$	$6.11 \cdot 10^{-4}$	$8.37 \cdot 10^{-2}$	$3.85 \cdot 10^{-1}$	$3.59 \cdot 10^{-1}$	$8.27 \cdot 10^{-1}$
600	$3.07 \cdot 10^{-4}$	$6.14 \cdot 10^{-4}$	$8.39 \cdot 10^{-2}$	$3.86 \cdot 10^{-1}$	$3.60 \cdot 10^{-1}$	$8.31 \cdot 10^{-1}$
610	$3.09 \cdot 10^{-4}$	$6.17 \cdot 10^{-4}$	$8.43 \cdot 10^{-2}$	$3.86 \cdot 10^{-1}$	$3.61 \cdot 10^{-1}$	$8.35 \cdot 10^{-1}$
620	$3.10 \cdot 10^{-4}$	$6.20 \cdot 10^{-4}$	$8.45 \cdot 10^{-2}$	$3.89 \cdot 10^{-1}$	$3.63 \cdot 10^{-1}$	$8.37 \cdot 10^{-1}$
630	$3.12 \cdot 10^{-4}$	$6.23 \cdot 10^{-4}$	$8.52 \cdot 10^{-2}$	$3.91 \cdot 10^{-1}$	$3.64 \cdot 10^{-1}$	$8.38 \cdot 10^{-1}$
640	$3.13 \cdot 10^{-4}$	$6.26 \cdot 10^{-4}$	$8.51 \cdot 10^{-2}$	$3.92 \cdot 10^{-1}$	$3.65 \cdot 10^{-1}$	$8.45 \cdot 10^{-1}$
650	$3.15 \cdot 10^{-4}$	$6.29 \cdot 10^{-4}$	$8.55 \cdot 10^{-2}$	$3.93 \cdot 10^{-1}$	$3.67 \cdot 10^{-1}$	$8.49 \cdot 10^{-1}$
660	$3.16 \cdot 10^{-4}$	$6.32 \cdot 10^{-4}$	$8.58 \cdot 10^{-2}$	$3.95 \cdot 10^{-1}$	$3.68 \cdot 10^{-1}$	$8.52 \cdot 10^{-1}$
670	$3.17 \cdot 10^{-4}$	$6.35 \cdot 10^{-4}$	$8.64 \cdot 10^{-2}$	$3.96 \cdot 10^{-1}$	$3.69 \cdot 10^{-1}$	$8.53 \cdot 10^{-1}$
680	$3.19 \cdot 10^{-4}$	$6.38 \cdot 10^{-4}$	$8.64 \cdot 10^{-2}$	$3.98 \cdot 10^{-1}$	$3.71 \cdot 10^{-1}$	$8.57 \cdot 10^{-1}$
690	$3.20 \cdot 10^{-4}$	$6.41 \cdot 10^{-4}$	$8.67 \cdot 10^{-2}$	$3.99 \cdot 10^{-1}$	$3.72 \cdot 10^{-1}$	$8.64 \cdot 10^{-1}$
700	$3.22 \cdot 10^{-4}$	$6.43 \cdot 10^{-4}$	$8.74 \cdot 10^{-2}$	$4.01 \cdot 10^{-1}$	$3.74 \cdot 10^{-1}$	$8.64 \cdot 10^{-1}$
710	$3.23 \cdot 10^{-4}$	$6.46 \cdot 10^{-4}$	$8.74 \cdot 10^{-2}$	$4.02 \cdot 10^{-1}$	$3.75 \cdot 10^{-1}$	$8.65 \cdot 10^{-1}$
720	$3.24 \cdot 10^{-4}$	$6.49 \cdot 10^{-4}$	$8.78 \cdot 10^{-2}$	$4.04 \cdot 10^{-1}$	$3.76 \cdot 10^{-1}$	$8.69 \cdot 10^{-1}$
730	$3.26 \cdot 10^{-4}$	$6.51 \cdot 10^{-4}$	$8.80 \cdot 10^{-2}$	$4.05 \cdot 10^{-1}$	$3.78 \cdot 10^{-1}$	$8.71 \cdot 10^{-1}$
740	$3.27 \cdot 10^{-4}$	$6.54 \cdot 10^{-4}$	$8.85 \cdot 10^{-2}$	$4.06 \cdot 10^{-1}$	$3.79 \cdot 10^{-1}$	$8.73 \cdot 10^{-1}$
750	$3.28 \cdot 10^{-4}$	$6.57 \cdot 10^{-4}$	$8.89 \cdot 10^{-2}$	$4.08 \cdot 10^{-1}$	$3.80 \cdot 10^{-1}$	$8.77 \cdot 10^{-1}$
760	$3.29 \cdot 10^{-4}$	$6.59 \cdot 10^{-4}$	$8.91 \cdot 10^{-2}$	$4.11 \cdot 10^{-1}$	$3.81 \cdot 10^{-1}$	$8.79 \cdot 10^{-1}$
770	$3.31 \cdot 10^{-4}$	$6.62 \cdot 10^{-4}$	$8.95 \cdot 10^{-2}$	$4.09 \cdot 10^{-1}$	$3.83 \cdot 10^{-1}$	$8.80 \cdot 10^{-1}$
780	$3.32 \cdot 10^{-4}$	$6.64 \cdot 10^{-4}$	$8.95 \cdot 10^{-2}$	$4.10 \cdot 10^{-1}$	$3.85 \cdot 10^{-1}$	$8.84 \cdot 10^{-1}$
790	$3.33 \cdot 10^{-4}$	$6.66 \cdot 10^{-4}$	$9.00 \cdot 10^{-2}$	$4.14 \cdot 10^{-1}$	$3.83 \cdot 10^{-1}$	$8.86 \cdot 10^{-1}$
800	$3.34 \cdot 10^{-4}$	$6.69 \cdot 10^{-4}$	$9.03 \cdot 10^{-2}$	$4.14 \cdot 10^{-1}$	$3.84 \cdot 10^{-1}$	$8.90 \cdot 10^{-1}$
810	$3.35 \cdot 10^{-4}$	$6.71 \cdot 10^{-4}$	$9.06 \cdot 10^{-2}$	$4.13 \cdot 10^{-1}$	$3.88 \cdot 10^{-1}$	$8.93 \cdot 10^{-1}$
820	$3.36 \cdot 10^{-4}$	$6.73 \cdot 10^{-4}$	$9.07 \cdot 10^{-2}$	$4.15 \cdot 10^{-1}$	$3.88 \cdot 10^{-1}$	$8.95 \cdot 10^{-1}$
830	$3.38 \cdot 10^{-4}$	$6.75 \cdot 10^{-4}$	$9.09 \cdot 10^{-2}$	$4.17 \cdot 10^{-1}$	$3.91 \cdot 10^{-1}$	$8.98 \cdot 10^{-1}$
840	$3.39 \cdot 10^{-4}$	$6.77 \cdot 10^{-4}$	$9.14 \cdot 10^{-2}$	$4.18 \cdot 10^{-1}$	$3.90 \cdot 10^{-1}$	$9.00 \cdot 10^{-1}$
850	$3.40 \cdot 10^{-4}$	$6.79 \cdot 10^{-4}$	$9.14 \cdot 10^{-2}$	$4.21 \cdot 10^{-1}$	$3.91 \cdot 10^{-1}$	$9.03 \cdot 10^{-1}$
860	$3.41 \cdot 10^{-4}$	$6.81 \cdot 10^{-4}$	$9.18 \cdot 10^{-2}$	$4.20 \cdot 10^{-1}$	$3.92 \cdot 10^{-1}$	$9.04 \cdot 10^{-1}$
870	$3.42 \cdot 10^{-4}$	$6.83 \cdot 10^{-4}$	$9.21 \cdot 10^{-2}$	$4.22 \cdot 10^{-1}$	$3.94 \cdot 10^{-1}$	$9.06 \cdot 10^{-1}$
880	$3.43 \cdot 10^{-4}$	$6.85 \cdot 10^{-4}$	$9.22 \cdot 10^{-2}$	$4.23 \cdot 10^{-1}$	$3.94 \cdot 10^{-1}$	$9.08 \cdot 10^{-1}$
890	$3.44 \cdot 10^{-4}$	$6.87 \cdot 10^{-4}$	$9.25 \cdot 10^{-2}$	$4.23 \cdot 10^{-1}$	$3.95 \cdot 10^{-1}$	$9.11 \cdot 10^{-1}$
900	$3.45 \cdot 10^{-4}$	$6.89 \cdot 10^{-4}$	$9.27 \cdot 10^{-2}$	$4.23 \cdot 10^{-1}$	$3.96 \cdot 10^{-1}$	$9.13 \cdot 10^{-1}$
910	$3.46 \cdot 10^{-4}$	$6.91 \cdot 10^{-4}$	$9.29 \cdot 10^{-2}$	$4.25 \cdot 10^{-1}$	$3.97 \cdot 10^{-1}$	$9.16 \cdot 10^{-1}$
920	$3.47 \cdot 10^{-4}$	$6.93 \cdot 10^{-4}$	$9.32 \cdot 10^{-2}$	$4.26 \cdot 10^{-1}$	$3.99 \cdot 10^{-1}$	$9.18 \cdot 10^{-1}$
930	$3.47 \cdot 10^{-4}$	$6.95 \cdot 10^{-4}$	$9.34 \cdot 10^{-2}$	$4.26 \cdot 10^{-1}$	$3.98 \cdot 10^{-1}$	$9.20 \cdot 10^{-1}$
940	$3.48 \cdot 10^{-4}$	$6.97 \cdot 10^{-4}$	$9.37 \cdot 10^{-2}$	$4.28 \cdot 10^{-1}$	$3.99 \cdot 10^{-1}$	$9.22 \cdot 10^{-1}$
950	$3.49 \cdot 10^{-4}$	$6.98 \cdot 10^{-4}$	$9.39 \cdot 10^{-2}$	$4.30 \cdot 10^{-1}$	$4.00 \cdot 10^{-1}$	$9.24 \cdot 10^{-1}$
960	$3.50 \cdot 10^{-4}$	$7.00 \cdot 10^{-4}$	$9.41 \cdot 10^{-2}$	$4.30 \cdot 10^{-1}$	$4.02 \cdot 10^{-1}$	$9.25 \cdot 10^{-1}$
970	$3.51 \cdot 10^{-4}$	$7.02 \cdot 10^{-4}$	$9.43 \cdot 10^{-2}$	$4.30 \cdot 10^{-1}$	$4.03 \cdot 10^{-1}$	$9.28 \cdot 10^{-1}$
980	$3.52 \cdot 10^{-4}$	$7.03 \cdot 10^{-4}$	$9.45 \cdot 10^{-2}$	$4.32 \cdot 10^{-1}$	$4.04 \cdot 10^{-1}$	$9.28 \cdot 10^{-1}$
990	$3.53 \cdot 10^{-4}$	$7.05 \cdot 10^{-4}$	$9.47 \cdot 10^{-2}$	$4.33 \cdot 10^{-1}$	$4.04 \cdot 10^{-1}$	$9.31 \cdot 10^{-1}$
1000	$3.53 \cdot 10^{-4}$	$7.07 \cdot 10^{-4}$	$9.49 \cdot 10^{-2}$	$4.33 \cdot 10^{-1}$	$4.05 \cdot 10^{-1}$	$9.32 \cdot 10^{-1}$